



UNIVERSITÀ
DEGLI STUDI
FIRENZE

PHD IN
CHEMICAL SCIENCE

**Transport of brownian particles and
bacteria in hydrogels with tunable
porosity**

Academic Discipline CHIM/02

Doctoral Candidate

Gavino Bassu

Supervisor

Prof. Emiliano Fratini

Coordinator

Prof.ssa Anna Maria Papini

The consultation of the thesis is free. Unless a specific authorization is obtained from the author, the thesis can be, however, downloaded and printed only for strictly personal purposes related to study, research and teaching, with the explicit exclusion of any use that has a even indirectly a commercial nature.

To live like this it's better to never die
G. Maddau

Abstract

In the present work, an insight into the impact of confinement imposed by application-relevant poly(ethylene glycol) (PEG) hydrogel matrices on the dynamics of passive and active colloids was presented. By thoroughly characterizing the internal structure of the hydrogels at the nano and microscale, and by the precise tailoring of the porosities of the developed hydrogels, we established a connection between the microgel dynamics (measured through particle tracking) and the 3D geometrical confinement imposed by the porous matrices. To do this, PEG hydrogels with a high degree of transparency, tunable pore sizes, and volume fractions achieved through freeze-drying, were employed. Our findings revealed that the hydrogel networks' porosity is defined by elongated channels with asymmetric sections, where the average size decreases from approximately 7 to about 2 particle diameters. The size distribution becomes narrower with an increase in PEG content in the pre-reaction mixture. As the confinement intensifies, the microgel dynamics undergo a slowdown and transition from diffusive to sub-diffusive behavior. The observed reduction in diffusivity aligns with models of diffusion in cylindrical pores and can be ascribed to hydrodynamic and steric effects, along with geometric constriction.

Furthermore, the motility of *B. subtilis* under different degrees of confinement induced by transparent porous hydrogels was investigated linking the bacteria's dynamic behavior at short times to specific the hydrogel's porosity and characteristic structural features. Mean squared displacements (MSDs) reveal a transition from the run-and-tumble dynamics of unconfined *B. subtilis* to progressively sub-diffusive motion with increasing confinement. The bacteria's dynamic behavior at short times is linked to specific parameters characterizing the hydrogel porosity. Consequently, the median instantaneous velocity of bacteria decreases and exhibits a narrower distribution, while the reorientation rate increases and reaches a plateau. By analyzing single trajectories, we demonstrate that the average dynamic behavior results from complex displacements, encompassing active, diffusive, and sub-diffusive segments. In instances of small to moderate confinements, the number of active segments decreases, while the diffusive and sub-diffusive segments increase. The interplay of sub-diffusion, diffusion, and active motion along the same trajectory is characterized as a hopping and trapping motion. In this scenario, hopping events correspond to displacements with an instantaneous velocity surpassing the corresponding mean value along a trajectory. In contrast to previous observations, the escape from local trapping in *B. subtilis* occurs not only through active runs but also via diffusion. Notably, the contribution of diffusion to escape is maximized at intermediate levels of confinement. Over sufficiently extended durations, transport coefficients, as estimated from experimental MSDs under various degrees of confinement, can be predicted using a recently proposed hopping and trapping model. Lastly, a quantitative relationship that correlates the median velocity of bacteria under confinement with that of unconfined bacteria, using the characteristic confine-

ment length of the hydrogel matrix, was proposed.

The present work offers an intriguing aspect is the unusual dependence of the effective diffusion coefficient on the pore volume fraction, indicating the presence of interactions between microgels and the hydrogel matrix. New insights into bacterial motility within complex media that simulate natural environments were reported, holding relevance for critical issues such as biological retention, water purification, biofilm formation, membrane permeation, and bacteria separation. These results underscore the significance of a thorough characterization of the 3D geometry of porous networks in comprehending transport properties within intricate, random porous media.

List of abbreviations

Acronyms

<i>PEG</i>	Poly(ethylene glycol)
<i>PEGDA</i>	Poly(ethylene glycol) diacrylate
<i>DMP</i>	2',5'-Dimethylacetophenone
<i>pNIPAM</i>	Poly(N-isopropylacrylamide)
<i>MBA</i>	N,N'-Methylenebis(acrylamide)
<i>APS</i>	Ammonium persulfate
<i>RhB</i>	Rhodamine B
<i>EWC</i>	Equilibrium water content
<i>HD</i>	Hydration degree
<i>FWI</i>	Free water index
<i>BWI</i>	Bound water index
C_{fw}	Free water mass per mass of polymer
C_{bw}	Bound water mass per mass of polymer
<i>DSC</i>	Differential scanning calorimetry
<i>SAXS</i>	Small angle x-ray scattering
<i>SEM</i>	Scanning electron microscopy
<i>LSCM</i>	Laser scanning confocal microscopy
<i>MSD</i>	Mean Square Displacement
<i>TSA</i>	Tryptic Soy Agar

TSB Tryptic Soy Broth

Greek letters

ξ Normalized confinement length
 ϕ Pore volume fraction
 α Pore area fraction
 ζ Average mesh size
 γ Average reorientation rate

Contents

Contents	11
1 Introduction	1
1.1 Motivations and aims	2
1.2 Gels	6
1.2.1 Gelation theories	7
1.2.2 Classification and types of gels	10
1.3 Colloids	17
1.3.1 Passive colloids: Brownian Motion	19
1.3.2 Active Colloids	22
1.3.3 Self-propelled bacteria	24
1.4 Transport of active and passive colloids in porous media	32
1.4.1 Confined passive diffusion	33
1.4.2 Confined active diffusion	37
2 Experimental section	41
2.1 Materials	42
2.1.1 Chemicals	42
2.1.2 Hydrogel preparation	43
2.1.3 Microgel preparation	47
2.1.4 Bacterial culture	50

2.2	Experimental techniques	52
2.2.1	Swelling behavior and water state	52
2.2.2	Structural characterization	55
2.2.3	Morphological characterization	59
2.2.4	Rheological behavior	63
2.3	Particle Tracking	65
2.3.1	Single particle tracking method	65
2.3.2	Instrumental setup	67
3	Results and discussions	69
3.1	PEG-based hydrogels	70
3.1.1	Synthesis and swelling behavior	70
3.1.2	Nanoscale topology	74
3.1.3	Morphological characterization	78
3.1.4	Viscoelastic regime and flow behavior	85
3.2	pNIPAM microgels	88
3.2.1	Microgels preparation	88
3.3	Dynamics of colloids	90
3.3.1	Diffusion properties of microgels	90
3.4	Dynamics of bacteria	99
3.4.1	Bacteria characterization and hydrogel loading	99
3.4.2	Motility behavior	104
3.4.3	Single-trajectory analysis	112
3.4.4	Trajectories classifying	117
3.4.5	Transport models	120
4	Conclusion	131
	Bibliography	137

A Publications	157
A.0.1 Attached Publications	161
Acknowledgments	171

Chapter 1

Introduction

1.1 Motivations and aims

Some of the most interesting phenomena, from physics to biology, and technological applications from medicine to environmental science, are associated with the diffusion properties of micro-metric objects in heterogeneous three-dimensional matrices. For example, porous matrices are involved in the microfiltration of undesired particulates to preserve instruments or vehicles; additionally, the recovery of valuable colloidal material from waste byproducts is of primary importance in industrial manufacturing. Moreover, the prediction of diffusion behavior of bio-colloids, such as viruses or bacteria, through soil or tissues has reached a huge interest in environmental, geological, and medical science. All of these cases raise the key role of the porous matrix. In particular, in all these systems the diffusion or active transport typically observed in bulk is inevitably affected by the confinement imposed by the porous structure and the particle-matrix interactions. A detailed knowledge of these effects is a key feature in giving complete insights into a wide range of biological, chemical, and physical processes that involve hindered transport. Recent approaches to elucidate the effect of confinement on the transport properties of passive colloids involved quasi-2D confining networks [1–3]. Two different regimes of motion were observed under 2D confinement: the usual bulk diffusion and a state in which particles expose sub-diffusive motion as a result of the confinement within the *holes* present in the matrix. Further studies of colloidal transport within ordered 3D structures highlighted the linear decrease of diffusivity with the increase of confinement length and with the decrease of the available free volume fraction [4–6]. Besides passive colloids, another subject of great interest whose dynamics have been extensively studied

in unconfined conditions is micro-swimmers. This class of active microscopic objects with the ability to move in a fluid environment represents the majority of motile bacteria. As is well known, bacteria are ubiquitous in micro-environments like animal or plant tissue, soil, and water. Due to this they play a crucial role in various environments and have a significant impact on fields like health, agriculture, environmental science, and industrial activities. Bacterial motility is an essential aspect of their behavior, enabling them to move, interact, and spread in extremely complex micro-environments. This mobility is often achieved through specific propelling mechanisms, with the most common being flagellum-based motion. The number of flagella and their distribution on the bacterial cell, along with the bacterial morphology (e.g., coccus, bacillus, vibrio), determine various motility modes and behaviors. One of the most common modes for micro-swimmers is the so-called run-and-tumble motility that is characterized by straight-line running, resulting from the synergistic rotation of bundled flagella, and rapid reorientations in which bacteria unbundle the flagella allowing a change of direction. Recent studies have shown the impact that the surrounding environment has on bacterial motility with surfaces in the vicinity of swimming bacteria leading to transient accumulation or confinement imposed by microfluidic chips inducing a strong variation of the run-time duration [7, 8].

Despite the numerous interesting findings, microfluidic experiments are not well representative of the porous natural media and are still far from natural conditions where the majority of the transport phenomena of colloids occur. With the exception of model systems with extremely regular porosity, the simultaneous investigation of the dynamics of colloids or micro-swimmers and the detailed study of the morphology of the confining net-

work is difficult to achieve. This is principally because, while the application-relevant porous matrices are opaque, the study of the dynamics is usually performed through optical methods, such as microscopy coupled with particle tracking, or correlation techniques like fluorescence correlation spectroscopy. The opacity, principally due to the difference in the refraction index between the porous network and the filler fluid, often limits the clear tracking of colloidal probes. Different strategies are adopted to reduce the reflection or refraction of the light allowing the particle tracking of the probes but with the consequent loss of structural and morphological information of the 3D matrix environment.

The present thesis work is focused on the development of new poly (ethylene glycol)-based hydrogels with tunable micrometric porous structure and high transparency degree and the simultaneous investigation of the local morphology and the transport properties of soft colloidal particles and biological micro-swimmers such as bacteria. Thanks to its biocompatibility, poly(ethylene glycol) (PEG) is the most diffuse polyether in terms of commercial volumes and biomedical applications [9–12]; it can be easily implemented in the preparation of hydrogels with a broad spectrum of physical and chemical properties. In this thesis work, transparent PEG hydrogels were synthesized by photopolymerization of the di-acrylate macromonomer, and the desired porosity on the micron scale was induced by freeze-drying treatment. In order to link the 3D geometrical confinement of the porous structure to the resulting dynamics of colloids and micro-swimmers, a detailed characterization of the internal structure of the hydrogels was coupled to the simultaneous single-particle tracking of the objects. The effect of the confinement imposed by this new class of hydrogels was first explored for thermo-responsive microgels of pNIPAM. Then, thanks to the high bio-

compatibility of the developed gels, the motility behavior of *Bacillus subtilis* bacteria was investigated in different confining conditions.

Transparent hydrogel matrices with tunable micron-scale porosities allowed the synergic detailed morphological characterization and the particle tracking technique, giving a better understanding of the confinement effects associated with disordered porous matrices, both on passive colloids and bacteria.

1.2 Gels

Gels are defined by the Union of Pure and Applied Chemistry (IUPAC), as a "nonfluid colloidal network or polymer network that is expanded throughout its whole volume by a fluid" [13]; in general, gels are systems made of at least two constituents where one of these is the macro-molecule (or colloid) that constitutes the three-dimensional (3D) network by covalent or noncovalent bondings arranged in the medium of other constituents (fluids). Thanks to their capacity to absorb a significant amount of solvent (up to a thousand times the polymer mass itself), gels are described as semisolid systems characterized by physical properties in between those of solid and liquid as a result of the polymeric chains (or colloidal) network filled by fluid. Polymeric gels have reached a huge interest over the past decades due to their applications in biomedicine and pharmacy, as composites for sensors and electronic devices, in food product development, and in agriculture. Polymeric gels reached a high degree of customization, depending on the constituent polymers, the nature and quantity of cross-linking, etc., which resulted in the strong diversification and the precise tuning of their physico-chemical properties, allowing their introduction in the most varied fields of application. Numerous are their application as porous soft-material for gel-electrophoresis, size exclusion chromatography, and as polymeric scaffolds for cell culture; Nevertheless, their application as natural-like matrices for three-dimensional (3D) confinement has not yet been studied in detail. Colloidal particle diffusion in 3D matrices is relevant to many fields of science, however, observing both diffusing systems and the detailed 3D structure of porous environments is nowadays still challenging due to media opacity.

1.2.1 Gelation theories

Gelation theories describe the process of formation of the network that provides solid-like properties to the gels. The development of gelation theories through statistical approaches led to the introduction of three models: the Flory-Stockmayer model [14], the percolation model [15], and the Cluster-Cluster Aggregation (CCA) model [16]. According to the Flory-Stockmayer model, gelation occurs when multifunctional molecules form covalent bonds with each other, resulting in a network structure. The model considers the possible formation of covalent bonds between monomers as a random event with an associated probability p . If this probability is small, the system exists in a *sol* phase, consisting of polymer chains with finite size (monomers, dimers, trimers, etc.). However, if the probability p exceeds a critical threshold value (p_c), a single chain with an infinite spatial extension, denoted as an "infinite network", is formed. This situation corresponds to the gel phase. The accuracy of this model in describing polymer network gels is limited by the complete absence of solvent, equal reactivity of all the functional groups involved in the reactions, the fact that only intermolecular reactions are allowed, absence of steric hindrance, and the omission of excluded volume effects by assuming that monomers are point-like objects. This theory predicts the gelation point and the degree of percentage conversion of the monomer into the polymeric network taking into account the reagents limiting the polymerization reaction. Due to the steric hindrance, which prevents functional groups involved from being equally reactive, the effective conversion degree required to reach the critical gelation point is higher than that expected by the Flory-Stockmayer Theory.

The percolation model described by Zallen and Stauffer consid-

ers the presence of the solvent and the self and cross interaction between the solvent molecules (A) and monomers (B). Through this, four interactions between particles can be defined:

- W_{AA} = Solvent-solvent interactions
- W_{AB} = Solvent-polymer interactions
- W_{BB} = Monomer-monomer van der Waals interactions, with a weight represented by p
- E = Bonding energy between monomers, with a weight represented by $1-p$

In this model, the gel phase is defined as the phase where a non-zero finite fraction of monomers is bonded together via chemical bonds to form a macroscopic molecule. This indicates the presence of a connected network structure within the system. In order to determine the gelation threshold, the pair monomers involved in the chemical bond must be nearest neighbours and their relative interaction energy must be equal to $-E$. Consistent with this approach, this model can be applied to reactive polymers made of M monomers.

The Cluster-Cluster Aggregation Model describes how gels form in colloidal systems. It suggests that, after the primary nucleation of small clusters or particles, they come together and stick, gradually forming larger clusters. These clusters continue to grow by incorporating more particles. Eventually, the clusters interconnect, creating a network that spans the system. This percolation transition marks the gelation point, where the system transforms into a gel. The interconnected clusters form a three-dimensional scaffold that traps the solvent or dispersing medium, resulting in the formation of a gel. This gel network exhibits both solid-like behaviour (elasticity) and liquid-like behaviour (flow under

stress), giving gels their characteristic properties.

The polymeric network structure obtained by the model can be topologically described through three characteristic parameters: the polymer volume fraction, the molecular weight of the polymer chain between two neighbouring crosslinking points, and the mesh size (ζ). The polymer volume fraction in the swollen state represents the fraction of the total volume of the gel occupied by the polymer in its swollen state. This parameter quantifies the amount of fluid absorbed and can be determined by equilibrium swelling experiments. The molecular weight of the polymer chain between two neighboring cross-linking points reflects the length or size of the polymer segment that is tethered between two cross-linking sites. The corresponding mesh size or correlation length defines the spatial arrangement of the polymer network, reflecting the average distance between adjacent cross-linking points in the gel network. It determines the size of the "pores" or "meshes" within the gel, affecting its permeability, swelling behavior, and responsiveness to external stimuli.

1.2.2 Classification and types of gels

Gels can be classified in various ways based on different criteria. Based on the nature of the cross-linking as physical and chemical gels; based on the polymeric network composition as a homopolymer, copolymer, and interpenetrated; based on the media in which the polymeric network is dispersed as xerogel, organogel, and hydrogel; based on the single polymeric network size as macrogels, microgels, and nanogels.

Physical and Chemical gels

Physical gels are unique materials constituted of polymeric three-dimensional networks resulting from the non-covalent interactions between the macromolecular chains. These non-covalent interactions include hydrophobic interactions, electrostatic interactions, Van der Waals forces, and hydrogen bonds. The relatively weak nature of these non-covalent interactions, with energies typically ranging from 1 to 120 kJ/mol, plays a key role in the dynamic behavior of these gels with cross-links that can be reversibly broken and reformed, changing their state between solid and liquid under influence of environmental factors. Almost all physical gels are thermoreversible; when the temperature is increased beyond a specific threshold, the supramolecular structure of the gel begins to melt due to the weakening or breaking of the non-covalent interaction, and the individual polymer molecules disperse back into the surrounding solvent, returning to a more fluid state. This transition is reversible, decreasing the temperature below the threshold value the gel structure can reform as the non-covalent interactions are reconstituted.

On the other hand, chemical gels are formed by cross-linked polymer networks through covalent bonds. These covalent bonds

are strong and permanent, with binding energies typically ranging from 200 to 650 kJ/mol. Unlike physical gels, chemical gels do not exhibit thermoreversibility; once the covalent bonds are formed, they are not easily broken and reformed. The densely interconnected network resulting from the cross-linking reaction gives chemical gels interesting physicochemical properties. In the last decades, chemical gels have gained increasing interest within biomedical sciences and across various scientific disciplines; driven by the growing need for application-relevant soft materials, several methods for the preparation of chemical gels have been developed. Here are some common methods used to obtain chemical gels:

- Chemical cross-linking involves the establishment of covalent linkages between polymer chains through chemical reactions of functional groups.
- Radical polymerization is a technique where low-molecular-weight monomers, in the presence of a cross-linking agent, undergo rapid polymerization through the formation of radical species.
- Condensation typically involves reactions between hydroxyl or amine groups and carboxylic acids or their derivatives, leading to the formation of amide bonds in the cross-links.
- Grafting involves the polymerization of a monomer onto the backbone of a preformed polymer.

Each of these methods offers unique advantages and may be chosen based on the specific requirements of the desired gel and the compatibility of the method with the intended application.

Chemical gels are essential in various industries, including materials science, pharmaceuticals, and biotechnology, where their covalent and highly structured nature is advantageous.

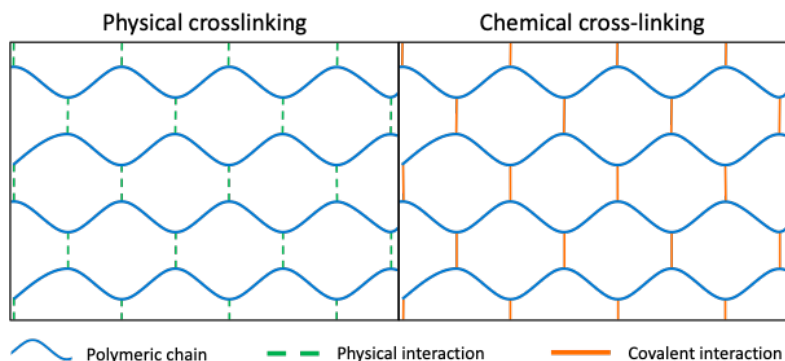


Figure 1.1: Schematic illustration of physical and chemical cross-linking in gels.

Homopolymer, Copolymer, Interpenetrating Polymer Network

Gels can be classified according to the nature of the structural units involved in the building of the supramolecular network. Homopolymer gels are formed by a polymeric network derived from a single species of monomers or macromonomers, which is the only structural unit that constitutes the 3D structure. Copolymer networks are formed by two or more different species arranged in various configurations along the polymeric chain. The monomers in the polymeric networks can be arranged in a random, block, or alternating configuration. The different arrangement leads to different properties in the resulting gel, depending on the sequence of monomers and the distribution of their species. Interpenetrating Polymer Networks (IPN) are a class of gels constituted by two

independent cross-linked polymeric networks three-dimensionally combined to form a unique gel matrix. This dual-network structure results in unique properties and enhanced performance. The choice of gel type depends on the desired properties and the specific requirements of the intended application.

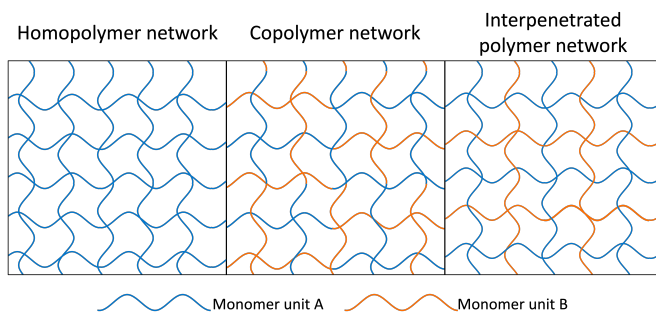


Figure 1.2: Schematic illustration of homopolymeric, copolymeric, and interpenetrated gel networks.

Xerogels/Cryogels/Aerogels, Organogels, Hydrogels

Gels can be classified on the nature of the fluid or the liquid phase that constitutes the media where the polymeric network is swollen. The primary categories of gels are xerogels, cryogels, aerogels, organogels, and hydrogels [17]. Xerogels, cryogels, and aerogels present a self-standing polymeric structure completely expanded in a gas phase and can be differentiated by the drying method. Xerogels are prepared by the direct evaporation of the solvent in air-drying, with the increase of the temperature or decrease of the pressure. As a result of this process, xerogels have tiny pore sizes (1-10 nm), and usually less porosity (5-50%) than cryogels and aerogels [18]. Cryogels are indeed characterized by their preparation through a process involving freezing and subse-

quent sublimation of solvent within the gel network [19]. Changes in the amount of solvent, structural component, cross-linking amount, and cooling rate play a key role in the distribution of pore sizes and the morphological and structural properties of the resulting gel. One critical step in the aerogel production process is the supercritical drying necessary for the controlled removal of the solvent; unlike conventional drying methods, a supercritical fluid is used in this process, typically carbon dioxide, to remove the solvent from the gel. Supercritical fluids, with their gas-like properties, allow complete penetration of the polymeric network and replacement of the solvent without causing it to collapse. Then, the supercritical fluid is gradually evaporated, leaving a solid material with a highly porous structure. In the preparation of aerogels, the polymeric structure is kept unaltered during the solvent removal leading to a highly porous and low-density material with high specific surface area, superior thermal insulation, and ultra-low sound transmission [20]. Different from xerogels, cryogels, and aerogels, hydrogels and organogels are characterized by a supramolecular polymeric structure dispersed in a liquid media. Based on the nature of the media gels are categorized into hydrogels, where the continuous phase is water, or organogels where the media may contain any type of organic solvent or oil.

Macrogels, microgels, and nanogels

Based on the size of the polymer network, gels can be classified into three classes: macrogels, microgels, and nanogels. Gels with a single supramolecular polymeric network greater than 1 μm are defined as macrogels, whereas polymer networks of submicron sizes (from 100 nm to 1 μm) are known as microgels. On the other hand, gels with network sizes smaller than 100 nm are defined as

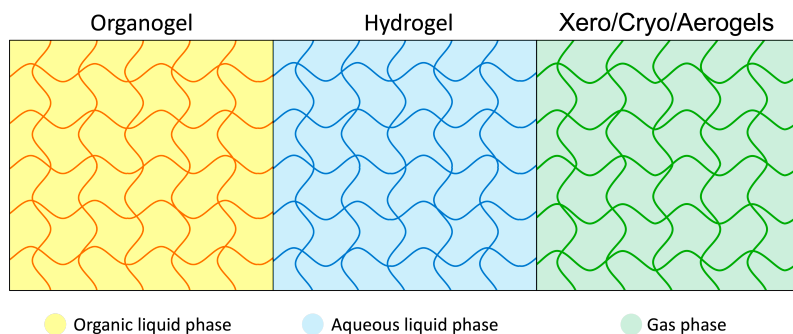


Figure 1.3: Schematic illustration of homopolymeric, copolymeric, and interpenetrated gel networks.

nanogels [21]. The concentration, and consequently the distance between the polymer molecules, play a fundamental role in the formation of the polymer network at different length scales. In dilute solutions, the greater distance between polymer molecules promotes intramolecular cross-linking instead of intermolecular cross-linking. Intramolecular cross-linking occurs within a single polymer chain when reactive functional groups or chemical bonds within the chain link together, thus creating the three-dimensional structures of a single microgel, or nano gel if the particle size is above or below 100 nm respectively. Under high polymer concentration conditions, the polymer molecules are closer together and therefore intermolecular cross-linking is promoted, leading to the formation of a larger three-dimensional network of a typical bulk macrogel. Macro gels were already described in the previous sections. Microgels are micron-sized colloidal particles formed by a polymer network with unique properties and interesting applications in many fields of science, including pharmacy and biotechnology. Microgels are often referred to as hydrophilic cross-linked latex which absorbs significant amounts of

water and possesses a responsive behavior under specific stimuli and changes in environmental conditions, such as temperature, ionic strength, light, and pH. Microgels offer several advantages over other carrier systems such as the precise control of particle size and shapes, greater colloidal stability, improved responsive behavior, and a high degree of functional customization. These abilities make microgels an excellent and versatile system for improved drug delivery with minimized potential side effects. Due to this several approaches have been developed for the preparation of microgels and the customization of their properties. They include photolithographic and micro-molding methods [22, 23], microfluidics [24], free radical heterogeneous polymerization in dispersion, precipitation, inverse (mini)emulsion, and inverse microemulsion [25].

1.3 Colloids

Colloids are objects typically ranging from nanometer to micrometer sizes (traditionally defined as between 1 nm and 10 μm), including a variety of particles such as engineered nanomaterials, viruses, bacteria, fine powders, proteins, and finely textured soil particles like clay. Nowadays we know that colloidal suspensions are extremely widespread in human life, among which milk is the most popular. Some colloidal systems, such as "extremely finely divided gold in a fluid" [26], had been known for over a century, however, the systematic investigation of these species began in 1861 through the publications of Thomas Graham; he identified as colloids those species that were unable to diffuse across a membrane. The size of these dissolved species was simply larger than the pore size of the membrane under investigation. The term "colloidal material" refers to suspensions or dispersions rather than solutions because the material is "suspended" or "dispersed" in the liquid phase. A first distinction of colloidal systems can be made based on the intrinsic properties of colloidal species: rigid particles, extremely flexible particles (also called macromolecules), and supra-molecular systems like viruses. Clearly, this classification does not have precise parameters; a polymeric dispersion can fall into the first or the second category depending on whether the solvent has poor affinity with the polymer, leading to its collapse and consequent formation of a stiff globule, or vice versa has good affinity, resulting in swelling and softening of the polymeric network. The conventional definition of colloids has historically relied on their size, but discrepancies in size classifications are evident in the literature, varying based on the properties of the systems under consideration. Establishing a precise boundary between colloids and molecules, or

larger particles, has been a source of contention, particularly in the biological sciences [27]. Consequently, a more pragmatic approach involves defining colloids by their properties that impact transport behavior; Despite larger particles, colloids demonstrate increased rates of diffusive flux, such as Brownian motion, and heightened reactivity owing to larger surface areas. They are also more strongly influenced by short-range surface forces. On the other hand, colloids follow more deterministic trajectories than smaller molecules, and their interaction forces, based on the same fundamental principles governing atom-atom and molecule-molecule pairings, can be larger and decay more gradually over distances than those of smaller molecules [28].

1.3.1 Passive colloids: Brownian Motion

The colloids identified by Graham are solutions of "large molecules" that exhibit Brownian motions, irregular motions generated by random collisions between solvent molecules with colloidal particles, consequently, colloidal particles are similar to *Brownian particles*. The experimental work of Jean Perrin [29] confirmed the seminal work of Albert Einstein and Paul Langevin [30] resulting in the formulation of the relationship between the mean square displacement of *Brownian particles* and their diffusion coefficient:

$$\langle \Delta r^2 \rangle = 2dD\tau \quad (1.1)$$

where the mean squared displacement describes the average square difference between two position vectors of the particle at a time difference τ ; d represents the spatial dimensions in which the particle moves and D is the diffusion coefficient. In 1908, Langevin introduced his equally renowned equation [31], which characterizes Brownian motion using a stochastic forcing term. Crucial in establishing the discrete, molecular nature of matter, Einstein described the effect of suspended spheres on viscosity [32], predicting the solvent increase of viscosity from η_s to $\eta_s(1 + 2.5\phi_s)$, where ϕ_s is the volume fraction of spheres dispersed in the investigated liquid. Thanks to this description, Brownian motions can be understood as arising from the collisions between solvent molecules and significantly larger dissolved particles and *Brownian particles* or colloids as those species, extremely larger than the molecule of the solvent in which they are dispersed, but still small enough to exhibit the characteristic Brownian motion at room temperature. Although it is relatively simple to define an upper limit for the size of a colloid, beyond

which these motions are negligible, the lower limit for these systems cannot be precisely delineated. Colloidal diffusion is characterized by the migration of colloids from areas with a high concentration of particles to those with a low concentration, resembling the molecular diffusion of individual molecules. In contrast to individual molecules, colloids undergo diffusion through a random walk behavior which stems from the numerous collisions between colloids and molecules in the surrounding fluid (see Fig. 1.4). The intensity of Brownian motion becomes more pronounced as the particle size decreases [33]. The impact of Brownian motion on colloid transport is significant, even in situations where the overall diffusive flux is relatively low compared to overall transport rates. Brownian motion impacts the trajectories of colloids during transport, determining the distance they can travel through porous media. Describing the trajectory of a solitary colloid in a flowing fluid involves a combination of deterministic forces (external, hydrodynamic/aerodynamic forces) and stochastic forces (Brownian force) [34, 35]. While moving through a porous medium, a colloid's trajectory follows the flow streamlines within the medium. The Brownian motion component of the colloid's path enables it to cross flow streamlines and come into contact with surfaces or other colloids that were not initially part of its trajectory [33].

Several phenomena observed in disordered systems, including energy transfer and hole burning in condensed molecular media, electron and hole transport in amorphous semiconductors, particle diffusion in porous materials, and chromatographic separation processes, involve the diffusion processes through complex media. In particular, the diffusion of particles is a fundamental process with broad implications across diverse scientific and practical domains, impacting fields as varied as biology, chemistry, physics,

materials science, and environmental science. Its study is essential for advancing our understanding of numerous natural and engineered systems.

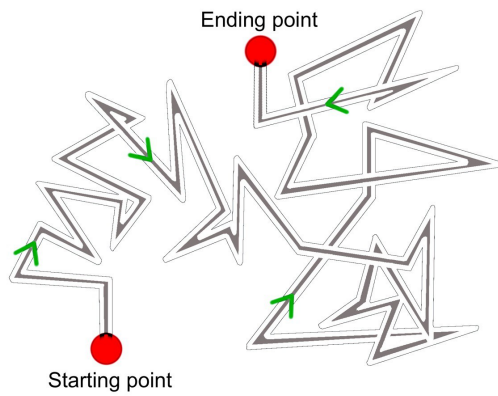


Figure 1.4: Representative random walk trajectory of a Brownian particle.

1.3.2 Active Colloids

Despite the great interest and in-depth studies carried out on passive colloids, numerous natural colloidal systems exhibit active transport, i.e. present self-propulsion capabilities, and are therefore known as active colloids or active matter [36, 37]. This new class of matter involves a wide number of non-equilibrium systems; cells, microswimmers, and nanomotors are just a few examples. Due to the complexity of such systems, the study, prediction, and complete understanding of their behavior require considerable interdisciplinary efforts from chemistry to biology, physics, and mathematics. In nature, evolution has developed and selected a wide variety of active systems with sophisticated propulsion mechanisms and navigation strategies tailored to the native environment. Pioneering studies on microswimmers revealed the presence of locomotive apparatuses consisting of cilia or flagella, and the study of their dynamic behavior has allowed the understanding of sophisticated strategies fundamental to their survival (i.e. chemotaxis and phototaxis) [38, 39]. Migration involves a range of fundamental biological processes, such as morphogenesis and tissue repair, cytoskeleton-generated forces, and intercellular and substrate adhesion, resulting in specific phenomena like fingering-like instabilities and glass-like arrest. Tissues, viewed as nature's active materials, serve as intriguing models for synthetic active materials due to their combination of diverse aspects such as epithelial monolayers exhibiting both elastic responses to stretching and 'super-elasticity' supported by active cytoskeletal polymerization dynamics.

Many strategies have been introduced for the preparation of artificial active systems to study and mimic the motion of motile bacteria, molecular motors, and other natural active systems [40].

Examples include inhomogeneous catalytic jets [41], magnetic nano-propellers [42], and Janus particles [43]; these nano- and micromachines set the basis for highly responsive multifunctional materials. As mentioned for biological micro-swimmers, the phenomena that can promote motion in preferential directions are gradients of concentration of nutrients or harmful species, respectively along or against the concentration gradient; similar to these, systems such as Janus particles [44], consisting of two hemispheres differently functionalized, one of which covered by catalyst elements, can exploit concentration gradients of hydrogen peroxide for active diffusion along the gradient. Examples of active systems range on many dimensional scales but all are united by the persistent condition out of equilibrium generated by the continuous consumption of energy to promote self-propulsion; all propulsion mechanisms involve the constant input of energy to perform the active motion, such energy is constantly dissipated into the environment.

Based on the motion strategy, self-propelled particles can be categorized into two main classes: active Brownian particles (ABPs), and run-and-tumble particles (RTPs). ABPs, such as spherical Janus particles and non-tumbling bacteria, move at a constant speed with direction changes imposed by their rotational diffusivity resulting from random thermal fluctuations from their surrounding environment [40]. On the other hand, RTPs are characterized by a dynamic based on straight-line runs, *runs*, performed at a constant speed, interrupted by reorientation events, *tumbles*. Despite their different motion modes, ABPs and RTPs behave similarly on long time scales; they exhibit the same translational diffusion constant of $(d - 1)D_r = \gamma$, with d the dimension of possible spatial moving, D_r the rotational diffusion, and γ the orientation rate [45].

1.3.3 Self-propelled bacteria

A fascinating class of active matter that still today presents numerous mysteries is motile bacteria. Motile bacteria spread and populate many different micro-environments from soil, and waste, to animal or plant tissue, playing a fundamental role in health [46,47], industry [48,49], and environmental science [50,51]. Bacteria play a crucial role in maintaining the health and functioning of ecosystems. They are involved in several interesting phenomena such as the nutrient cycling, decomposition, and conversion of organic matter. Many bacteria are beneficial and inhabit the human body, aiding in digestion, producing essential vitamins (like vitamin K), and protecting against harmful pathogens. Bacteria are involved as host organisms for the production of various products, including pharmaceuticals, enzymes, and biofuels. Bacteria can be engineered to produce specific compounds, making them valuable tools in industry. Their technological application is crucial in agriculture for processes like nitrogen fixation, in food production processes such as fermentation. Bacteria represent excellent model organisms in scientific research. They have simple and well-understood genetic systems, making them ideal for studying fundamental biological processes.

Among the many characteristics that have allowed their proliferation and the colonization of all microenvironments on our planet, there is their extraordinary ability to move, reorient, swim, and run in a multitude of even extremely complex media. Bacterial motility refers to the ability of bacteria to move actively toward favorable environments and to spread and populate new habitats. Bacteria have evolved diverse mechanisms to navigate and adapt to different environments, allowing them to thrive in a wide range of ecological niches. A first broad classification of the bacterial

motility mechanisms was performed by J. Henrichsen [52], who observed 40 bacterial species and identified five different categories: gliding, sliding, twitching, swimming, and swarming (see Fig. 1.5). Gliding motility is observed in bacteria that lack motile organelles such as flagella and pili. The exact mechanism behind gliding varies among different bacterial species; it involves the smooth and continuous movement over surfaces as a result of various possible strategies, including slime secretion, surface adhesion, and rotation of surface structures [53]. Similar to gliding, sliding is a motility strategy that involves the secretion of surfactants to facilitate the passive surface cell motion powered by the growth and division of the colony that pushes new cells across the surface [54]. In contrast to the smooth and organized cell movement exposed by gliding or sliding, twitching is the intermittent and uneven bacterial motility strategy that involves the extension and retraction of thin, hair-like appendages called pili or type IV pili. These pili allow bacteria to move across solid surfaces, such as agar plates or host tissues [55].

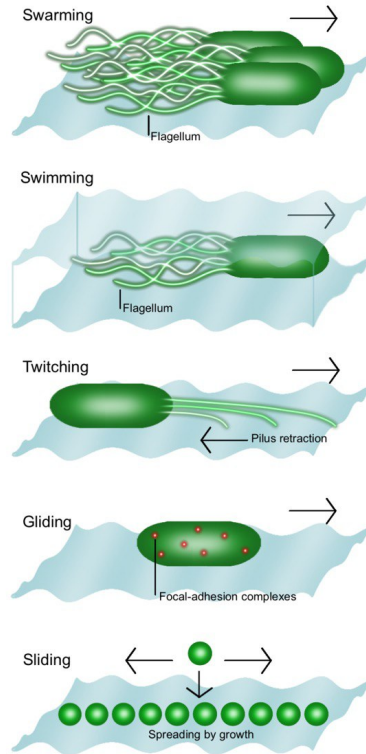


Figure 1.5: Graphical of the main bacterial motility mechanisms [55]. Swarming is bacterial movement on surfaces with rotating flagella. Swimming is individual bacteria movement in bulk liquid using flagella. Twitching involves pili extension, attachment, and retraction for surface movement. Gliding is flagella/pili-independent surface movement with focal-adhesion complexes. Sliding is passive surface translocation powered by growth and aided by a surfactant.

Flagella are long, whip-like appendages or structures that protrude from the surface of certain cells, enabling them to move. These structures are primarily involved in cell motility. Flagella are found in various organisms, including bacteria, archaea, and eukaryotic cells. In bacteria, flagella are composed of pro-

tein filaments that rotate like propellers, allowing the bacteria to swim through liquid environments. The rotation of these flagella is powered by a molecular motor located at the base of the structure. The movement of flagella in bacteria is essential for processes such as chemotaxis, where the bacteria can move toward or away from chemical signals in their environment. The locomotory structure of Gram-negative swimming bacteria, such as *Escherichia coli* and *Salmonella*, involves the rapid and reversible rotation of flagella at speeds up to 300 Hz driven by macromolecular motors integrated into the cell membrane and connected to the flagellar filament base; to drive this propulsion process the motor utilizes an electrochemical potential gradient generated by differential proton accumulation across the cytoplasmic membrane. The flagellum is an extensive molecular assembly comprised of approximately 20-30 thousand protein subunits, involving around 30 different proteins. Its structural elements can be categorized into two groups: the basal body rings and the tubular axial structure. The basal body rings, which include the L-ring, P-ring, MS-ring, and C-ring, constitute the rotary motor along with the stator complex formed by MotA and MotB cytoplasmic membrane proteins. The MS- and C-ring collaborate to create a rotor [56–58](see Fig. 1.6), and the generation of torque results from the interaction between the rotor and stator, coupled with the flow of protons through the proton pathway within the stator complex [59, 60]. Flagella play a crucial role in the survival and function of many microorganisms, contributing to their ability to navigate and interact with their environment.

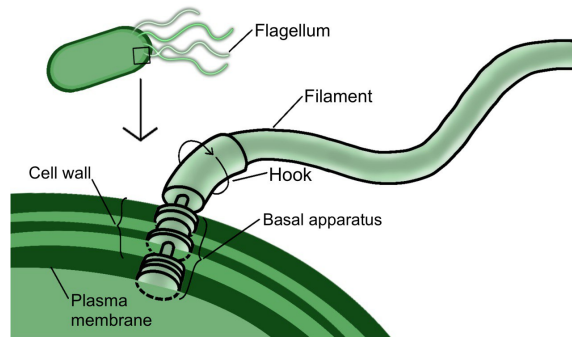


Figure 1.6: Schematic illustration of the bacterial flagellum describing the various functional units. The names of the components are presented in the illustration.

Copyright © 2008 Pearson Education, Inc., publishing as Pearson Benjamin Cummings.

The sophisticated flagellar apparatus allows the self-propelled bacteria to perform active motion of swimming and swarming mode. Swarming motility is characterized by the coordinated, rapid movement of bacteria across solid surfaces as a multicellular group. This behavior typically involves a dense, spreading population of bacteria moving in unison across a surface, and it is often observed under specific environmental conditions [61]. Swimming motility is the individual cell movement powered by rotating flagella but, unlike swarming, takes place in liquid environments. Swimming motility is one of the most expressed motility strategies, giving bacteria an advantage in surviving unfavorable environmental conditions [62]. In the early stages of the host-microbe interactions swimming motility plays a key role allowing the planktonic bacteria to explore and come close to host

surfaces or matrices. The straight movement (run) is generated by the counterclockwise rotation of one or multiple flagella, to generate thrust. Several events could induce tumbling to change direction, such environmental factors such as nutrient gradients, or the presence of harmful species. During the reorientation event (tumble), one or more clockwise rotations can bundle, drag, and cause a change in the direction of the cell [63]. This alternating pattern of running and tumbling, called run-and-tumble, allows bacteria to explore many micro-environments in response to external stimuli; run-and-tumble represents an efficient strategy for finding favourable conditions or avoiding harmful ones, making it crucial for the survival and adaptation of bacteria in diverse environments. This motility mode is constituted of three movement strategies: conventional run-tumbling with ballistic runs interrupted by directional changes, the run-reverse-flick movement in which the run is alternated by a "reverse" phase in which the flagellar rotation is reversed to allow the bacterium to retrace short paths followed by quick "flicks" in which the propulsion of the rotating flagella is stopped to allow a rapid reorientation of the cell, and the run-reverse mode where the flagella reverse their rotation allowing the backward movement (the three movement strategies are graphically represented in Fig.1.7). At short times swimmers with run-and-tumble motility perform persistent motions mainly characterized by straight-line runs that give rise to ballistic motion. At a long time, on the other hand, the increasing reorientation events become significant leading to a randomization of the bacterial movement describing a diffusive regime. Run-and-tumble motility can be mathematically modeled as a stochastic process in which "runs" are straight-line motions performed at constant speed v_0 interrupted by tumbling events whose frequency follows the Poisson distribution, in which events are in-

dependent of each other and the frequency with which they occur is assumed constant. Models of this type assume that the duration of tumbling events is negligible and after reorientation, the bacterium resumes its run with the speed v_0 reached instantly. Moreover, in this model, interactions with other agents, such as other microorganisms and the surrounding environment are assumed to be negligible with completely elastic collisions. Through models of this type, it is possible to define the relation between the mean square displacements and time; the mean square displacements scales as $\langle \Delta r^2 \rangle \approx \tau^2$ at short times, and $\langle \Delta r^2 \rangle \approx \tau$ at long times, demonstrating the presence of the ballistic and diffusive regime respectively. The transition between the ballistic and diffusive regimes can depend on various factors such as the availability of nutrients, environmental conditions, and the specific motility mechanisms of the bacteria. In general, with equal nutrient and environmental conditions, the transition between the two motion regimes is determined by the characteristic running speed and frequency and duration of the reorientation events, peculiar to each bacterium [64].

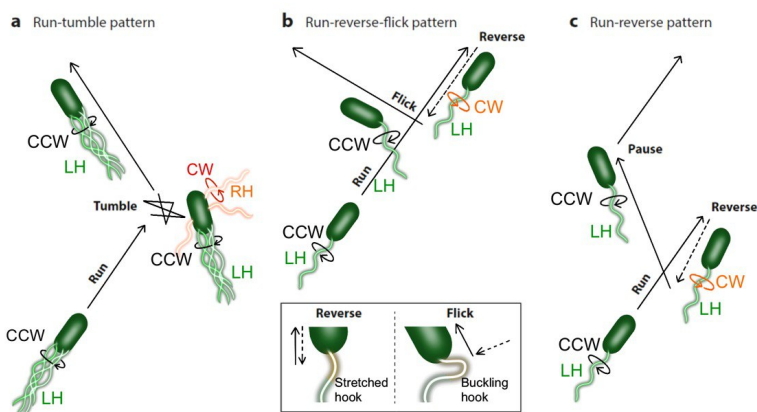


Figure 1.7: Schematic representation of the characteristic phases of flagellated swimming bacteria: run-tumble pattern (a), run-reverse-flick pattern (b), and run-reverse pattern (c).

1.4 Transport of active and passive colloids in porous media

The ubiquitous presence of colloids determines their importance in numerous fields, among which stand out the systems in which the movement and diffusion of colloids in porous matrices play a key role; The movement of colloids through porous materials has implications across diverse fields, including medical sciences, industrial manufacturing, geosciences, and environmental engineering. Numerous industrial processes involve porous media filters to recover harmful colloidal materials; in the medical field, colloids like albumin move through the body via porous blood vessels, playing a crucial role in maintaining human health. Innovative cancer treatment technologies leverage colloid transport behavior to specifically target cancerous cells [65]. In geosciences and environmental engineering, there is considerable interest in predicting the movement of colloids like pathogenic bacteria and viruses through soils or other porous media [66,67].

1.4.1 Confined passive diffusion

A complete understanding of the dynamics in heterogeneous disordered porous media represents a goal of great interest in many fields of science and industrial processes. A first description of the behavior of Brownian particles diffusing in a medium was introduced with the Lorentz gas model [68], named after the Dutch physicist Hendrik Lorentz to describe the diffusion of hard spheres (representing the particles) moving in a medium that undergoing elastic collision with each other. The Lorentz model predicts a delocalization-to-localization transition associated with a decrease in the accessible empty volume beyond a critical value. This hypothesis describes the delocalized dynamics of diffusing particles in low-density matrices, resulting in a large accessible volume. while, as the density of obstacles in the matrix increases beyond the critical percolation density, particles become trapped in "pockets" of accessible space where they become localized. This condition leads to anomalous long-time diffusion characterized by a sublinear dependence of the mean squared displacement (MSD) on time, which can be defined as $\delta r^2 \approx t^n$, with $n < 1$ [69]. Although models based on Lorentz's theory are brilliant, the experimental relationship of diffusive properties in cluttered and crowded matrices is still very rare today. The bi-dimensional diffusive behavior of colloids has been experimentally studied using model systems and molecular dynamics simulations [70]. To do this, small spherical colloidal particles were observed in a 2D model system consisting of large fixed particles (obstacles) randomly distributed. These experiments highlighted the crucial effect of confinement on the dynamics of the fluid-dispersed colloidal system; a key role in this phenomenon is represented by the structural characteristics of the confining matrix, such as the

accessible area fraction, density, and distribution of obstacles. By decreasing the accessible area fraction, defined as the area explored by the particle and thus not occupied by the confining matrix relative to the total investigated area, an increase in the localization of the colloidal system dynamics can be observed.

Diffusion at the molecular level within densely populated environments has been simulated in the presence of geometric constraints, revealing two primary scenarios related to the mean free path of the molecule and the characteristic length of the confining system [3]. Knudsen diffusion describes the movement of particles within spaces whose dimensions are comparable to or smaller than the mean free path of the diffusing particle. This type of diffusion is particularly significant in various natural and engineered (nano)porous media, such as the diffusion of pharmaceuticals through tissues. Fick-Jacobs diffusion occurs when diffusion takes place within a confining matrix with at least one dimension comparable to or smaller than the mean free path of the diffusing particle and another dimension smaller than this characteristic dimension. The Fick-Jacobs equation is a crucial tool for examining diffusion in biological channels or zeolites. Concerning the diffusion processes in porous media, the Knudsen and Fick-Jacobs models represent two brilliant insights into molecular diffusion under confinement that, despite taking into account the geometries of the neighboring structure, are affected by the matrix's porosity and tortuosity, which lead to inaccuracies in the description of the effective diffusivity of the system [71].

Recent works investigated the Brownian motion behavior in quasi-2D confining networks [1–3]; the colloidal templated technique [72] involved in these works allowed the preparation of a 2D arrangements of spherical cavities connected by circular holes. The experimental setup enabled *in situ* observation of DNA molecules

with different size ranges revealing the existence of two different motion regimes: a free-diffusion state, typically associated with the diffusion in the bulk liquids, and a trapped state in which the molecules inside confining holes present sub-diffusive motion. Remarkably, the two regimes mutually switch between prolonged localizations in the cavities, characterized by longer permanence times, and rapid "jumps" through the junction holes. The bi-dimensional MSD was found to be linearly dependent on time, allowing the extrapolation of the diffusion coefficient; compared to the unconfined free-diffusing molecules, the diffusion coefficient was found over two orders of magnitude greater than diffusing in the confining array. Consistent with the Einstein derivation, the diffusion coefficient decreases with the increase of the particle size, reflected in this case by the molecular weight. Moreover, the average jumping frequency is strongly related to the particles' size diffusing in the confining matrix [1] with the resulting localization periods increasing with the particle size. The diffusion properties of confined colloids in quasi-2D model systems consisting of frozen colloids have been investigated by microscopic experiments, accompanied by simulation studies in which matrix-particle interactions are described by the repulsive potential of Lennard-Jones; these studies provided a relationship between the dimensionless diffusion parameter and the structural entropy of the confining system [4]. By varying the packed fraction of the matrix there is a discrepancy between the diffusivity coefficients extrapolated experimentally and calculated in the simulations with values provided by the computational model slightly higher than the experimentally determined values. This evidence confirms that precise knowledge of the morphology of the neighboring system is of fundamental importance to have a better knowledge of the matrix-particle interaction at play in dense and extremely crowded sys-

tems.

The constant search for matrices more and more similar to real systems has led to the investigation of 3D-ordered systems, which provide an excellent starting point for the study of the three-dimensional diffusion properties [6]. The study of differential dynamic microscopy of dilute dispersions of nanoparticles confined in arrays has demonstrated the significant slowdown in the dynamics of nanoparticles; the analysis of single particle tracking showed the linear decrease in the diffusion coefficient in conjunction with the decrease in the accessible space in the investigated volume and, equivalently, the increase in confinement. Other 3D-ordered structures are represented by inverse opals with variable cavities, which have been used as confining matrices for fluorescence correlation study [5]; these experiments show anomalous diffusions for extremely confined systems that diverge from standard Brownian dynamic models. The divergences would be related to possible imperfections and inhomogeneities determined by the degree of polydispersity of the starting opals, which have a significant magnitude at high degrees of confinement.

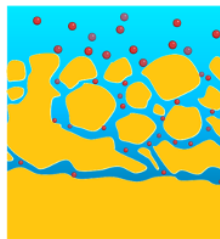


Figure 1.8: Sketch of colloids' percolation

1.4.2 Confined active diffusion

The active motion of the self-propelled system allows them to move and populate a large range of complex and crowded micro-environments. The development of new active matter systems, such as microrobots, smart drug delivery systems, and bacteria-sequestering technologies [73], rely not only on understanding the dynamic behavior of these systems in bulk liquid but moreover in confined spaces and crowded environments well-representative of the application matrices such as porous heterogeneous media. Many efforts have been made to predict and understand the behavior of active matter in such matrices, and numerous computational and experimental studies, predominantly on ordered model matrices, have allowed for an initial understanding of this still-open topic. The active motion in such matrices leads to several interesting and application-relevant phenomena (i.e. surface adhesion, and accumulation at boundaries) [44]. The persistent motion of ABPs from bulk liquid to porous matrices results in an inhomogeneous distribution of the active particles near the boundary solid surface [74, 75]. The mean-free path of ABPs is dramatically affected by solid boundaries or obstacles; the resulting decrease in the available free space leads to a cut-off of their run length and consequently reduces the effective diffusivity with the accumulation at boundaries [75]. Simplified models of ABPs and micro-swimmers have been applied to the study of collective dynamics, primarily to investigate diffusive properties under the influence of external fields and varying degrees of confinement by radially symmetric potentials [76]. The simulations performed in the Unified Colored Noise approximation (UCNA) [77] found interesting results of the stationary state that qualitatively agree with the analytical results for high values of rotational dif-

fusion coefficients resulting from a low degree of confinement. On the other hand, the results diverge in highly confined conditions, where diffusion coefficients are dramatically decreased and the spectrum of possible velocities that can be imposed is restricted to only low velocities. The reduction of these characteristic parameters promoted numerous experiments and theoretical studies that have highlighted the presence of transient events near the confining walls; micro-swimmers reaching the confining wall or obstacle remain in its vicinity for a certain time before "escaping" to continue their journey [41,78,79]. Despite similarities between absent confinement and mild confinement conditions, ABPs and RTPs interact differently with the confining walls when the distance between the confining walls is comparable to or smaller than the characteristic run length of the investigated particle [80]. Based on these differences, various strategies have been introduced to separate and "trap" ABPs and RTPs [40]. The theoretically predicted results with Matryoshka-like mazes in different geometries suggest interesting potential applications for the efficient separation of these systems; ABPs accumulate in the outermost region of Matryoshka-like mazes, while RTPs occupy all positions inside the maze with almost equal probability.

In the specific case of biological micro-swimmers, bacterial motility is essential in the exploration and interaction with surfaces as well as spreading highly confining microenvironments (e.g., animal or plant tissue, soil, waste, granulated, and porous materials). Consequently, a deep knowledge of the motile behavior, from bulk liquids to highly confining matrices, would lead to great improvements in many fields of science and technological application. In order to achieve a more general understanding of the motility in confining microenvironments, microfluidic experiments were performed involving several microfluidic geometries

at different geometrical complexity and various levels of confinement [81]. Research on *Chlamydomonas reinhardtii* has demonstrated that the movement of algae is dramatically affected by obstacles such as arrays of pillars; the increase of the pillars' density results in the decrease of both the mean correlation time of direction as well as the effective diffusion coefficient compared to free space [82]. Moreover, in densely populated environments, *E. coli* exhibits a distinctive hopping-trapping behavior, in which it becomes trapped in pockets between closely packed obstacles and subsequently navigates confined channels to reach other pore spaces [83]. Additionally, periodic porous media significantly affects the chemotactic migration of bacteria, where confinement strongly influences directed motion, causing active particles to move cohesively over considerable distances [84]. The promising prospects in both medical and engineering applications led to the employment of mathematical modeling as a sophisticated instrument, coupling experimental findings into a conceptual structure to understand the intricacies of motility. Many of these include fluid shear effects, body shape asymmetry, flagellar chirality, and so forth [85–87]. Such models offer qualitative predictions of the motion similar to those experimentally observed. Despite the complexity of flagellum-based bacterial motility, constituted of multiple phases as shown in Fig.1.7, an effective simplification is represented by the switch between straight runs and changes in direction, resulting from bundling and unbundling of flagella, respectively, in the so-called run-and-tumble motility mode [88]. These systems have been modeled using random walk approaches, with reorientation events interspersed with straight runs [89]. In these models, diffusion in homogeneous porous systems is substantially determined by the pore size. Two regimes are distinguished: wide pores where the pore size is greater than the

characteristic run length and narrow pores where the pore size is smaller than the run length. In the limit of infinitely large pores, the first regime reflects the motion of bacteria in bulk liquids with excellent agreement between predictions and experimental evidence [90–92]. Transition to the narrow-pore regime assumes an unchanged running speed equal to the free-diffusing micro-swimmer; that speed is applied for shorter run lengths as a result of the imposed confinement with values corresponding to the pore diameter [93, 94]. Observations in three-dimensional systems reflecting this regime are only partially addressed by two-dimensional or three-dimensional ordered confined systems since most microscale porous matrices have a high degree of opacity, avoiding the direct observation of micro-swimmers. Recent studies involving hydrogel matrices highlight how the assumption of unchanged speed under high degrees of confinement leads to predictions that diverge from observed experimental data [83, 95]. These results suggest possible interactions with the matrix and the determination of increasingly prolonged "trapping" events as the dimensions of the pores in the confining matrix decrease.

Although these studies have greatly contributed to the comprehension of bacterial behavior in confined conditions, the microfluidic chips are not well-representative of the natural environment where bacteria usually proliferate and thrive. An additional effort is needed to fully understand bacterial motility in heterogeneous three-dimensional systems with a high degree of confinement and complexity.

Chapter 2

Experimental section

The following chapter reports the materials, the synthetic procedures, and the processing methods involved in the preparation of the systems investigated in this thesis work. Followed by the main techniques of investigation, instrumental conditions used for the physicochemical characterization of the prepared gel systems (macro and microgels), and the particle tracking technique.

2.1 Materials

2.1.1 Chemicals

Poly (ethylene glycol) (PEG) with a molar weight of 35000 g/mol (purity 99%), acryloyl chloride (purity 97%), and 2,2-Dimethoxy-2-phenylacetophenone (DMP) (purity 97%) were purchased from Merck. The hydroxyl termini of PEG polymeric units were acylated by a 4-fold molar excess of acryloyl chloride and triethylamine (TEA) in 100 mL of dichloromethane under a nitrogen atmosphere. The obtained poly (ethylene glycol) diacrylate (PEGDA) was precipitated out of the solution in cold diethyl ether. The filtered white powder was stored at - 20 °C until use. N-isopropyl acrylamide (NIPAM, purity 99%), N, N'-Methylenebis(acrylamide) (MBA, purity 99%), Ammonium persulfate (APS, purity $\geq 98\%$), water solution of glutaraldehyde (5 wt%), *tert*-butanol solution of Osmium tetroxide (2.5 wt%), and Phosphate buffer saline pills were purchased from Sigma Aldrich. The fluorescent probes Rhodamine B (RhB)(purity $\geq 95\%$), Oregon Green 488 (purity $\geq 95\%$), and SYTO9 (from Live/Dead *BacLight*TM), respectively from Sigma Aldrich and Thermo Fisher Scientific, were used to prepare the dye solutions following instructions provided by suppliers. Water was purified by a Millipore Milli-Q gradient system (resistivity $< 18 \text{ M}\Omega\cdot\text{cm}$).

2.1.2 Hydrogel preparation

Poly(ethylene glycol) acrylation process

In order to synthesize micropatterned poly(ethylene glycol) diacrylate-based hydrogels that can be used as substrates for diffusion studies in complex matrices, the polymer has been first functionalized with the acrylic functionalities graft at the two ends of the polymer chain [96]. In order to remove the possible presence of water, 10 g of PEG of the desired molar weight was lyophilized overnight. The polymer pellet was completely solved in a three-neck round-bottom flask with anhydrous dichloromethane and evacuated three times under an inert atmosphere. To the obtained solution the triethylamine was added in a ratio of 2 mol TEA:1 mol PEG with a glass syringe and kept under mixing for 5 minutes. Then, a four-times excess of acryloyl chloride was very slowly added to the PEG solution. The reaction environment was then evacuated again and kept in an inert atmosphere in the dark for at least 12 hours. The solution was then transferred in a separatory funnel with 1/4 to 1/2 of the total volume of a 1.5 M K_2CO_3 water solution and shaken vigorously for a few seconds, venting the funnel to release CO_2 between shakings. The two phases were separated by gravity overnight. The lowest organic phase was drained in a beaker and the water residues were removed with anhydrous $MgSO_4$. The organic phase was filtered and the PEGDA precipitated out of the solution in cold diethyl ether as white crystals. The PEGDA was dried under vacuum overnight and stored at $-20\text{ }^\circ\text{C}$.

PEG hydrogel synthesis

PEG hydrogels were prepared by photo-induced free radical polymerization of water solutions of the acrylate macromonomers

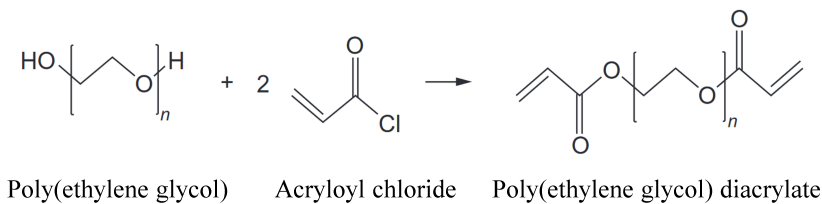


Figure 2.1: Acrylation reaction of poly(ethylene glycol) of the desired molecular weight with acryloyl chloride.

(PEGDA) and DMP. The acrylic functionalities of the macromonomers easily undergo interconnection processes in the presence of free radicals allowing the three-dimensional crosslinking of the polymeric system [97,98]. The terminal acrylic functions of the macromonomer chain ensure the cross-linking of the system through a complex polymerization process that can be explained through the combination of two most simple mechanisms: chain-growth and step-growth polymerization [99]. The fast propagation of the active centers through monomers with unsaturated vinyl bonds resulting from the chain-growth process leads to a more heterogeneous network (Fig. 2.2). On the other hand, step-growth-polymerized hydrogels are formed by the reaction of at least two multifunctional monomers with mutually reactive groups, where each monomer serves as a cross-linking point. In contrast to the chain-growth mechanism, step-growth gelation occurs when at least two multifunctional monomers react together producing fewer structural defects during reticulation. Generally, covalently crosslinked PEG hydrogels result from the combination of these two reaction mechanisms, leading to a more ordered structure, in the prevalence of step-growth, or with greater inhomogeneity, in the prevalence of chain-growth.

Different amounts of PEGDA were vigorously mixed until the

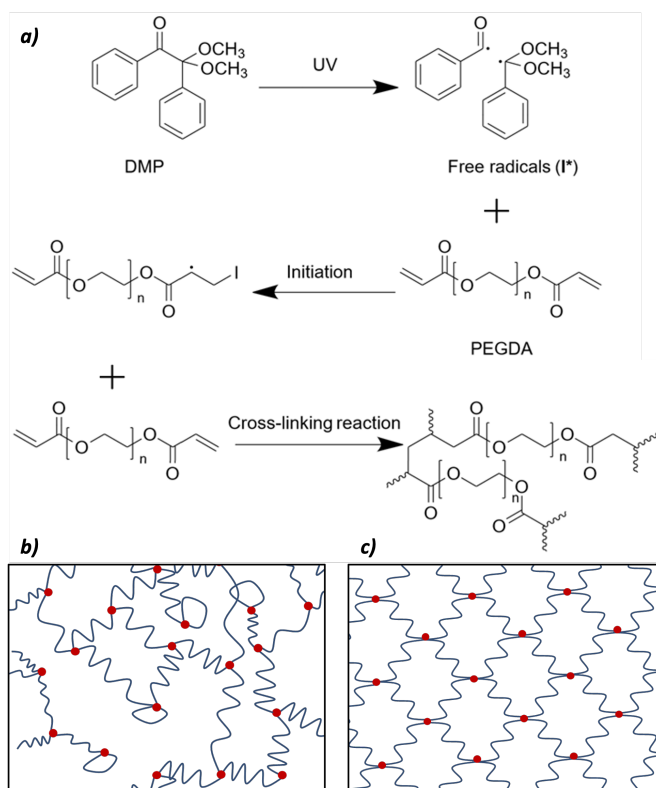


Figure 2.2: Free radical polymerization reaction of the PEGDA photoinitiated by DMP [99] (a); sketch of the polymeric network resulting from pure chain-growth (b) and pure step-growth mechanism.

complete dissolution in water to obtain pre-reaction mixtures at specific macromonomer concentrations (10, 12, 16, 20, 25, and 30 wt%). Then 10 μL of an ethanol solution of DMP (0.2 g/L) was added to the pre-reaction mixture and bubbled with nitrogen for 1 minute. In order to remove the remaining bubbles, the solution was centrifuged at 3000 rpm for 10 minutes. The obtained transparent pre-reaction mixture was cast in rectangular demountable glass molds of 2 mm thickness and photo-cross-linked overnight

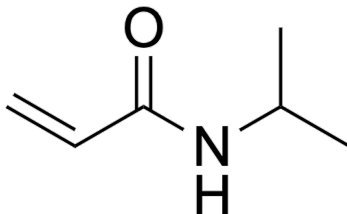
by a UV lamp (Camag[®]; power = 55 W; 365 nm wavelength) at a 7.5 cm distance. After the reaction, a 2 mm thick flat transparent hydrogel was obtained; the gel was then cut into squares of 1 cm and placed in water to remove residues of unreacted monomers, water was changed once a day until complete equilibration. In order to induce the desired micron-scale porosities, the swollen hydrogels were then freeze-dried by direct immersion in liquid nitrogen for 5 min and then completely dried at -55 °C and 40 mtorr overnight. The freeze-drying procedure involves the formation of ice crystals that act as porogen; the ice crystalsâ nucleation and growth involve the compression of the polymeric homogeneous network into compact polymeric walls leading to a macroscopic porous network. The resulting white xerogels were rehydrated in MilliQ water for 48 h. Hereinafter, all the hydrogels are named using the initial letter "P" followed by the macro-monomer concentration in the pre-reaction mixture. Under this notation, the investigated hydrogels fall in the range from P10 to P30. The prepared gels were labeled with Rhodamine B to directly observe the porous structure during each experiment. Each gel was equilibrated in Rhodamine B solution for 72 hours.

2.1.3 Microgel preparation

pNIPAM microgels

Among the many strategies developed to synthesize microgels, the most commonly used is probably the precipitation polymerization in which all the components needed for polymerization, including monomers, crosslinkers, and initiators, are dissolved in a suitable solvent, typically water. Then an initiator (peroxide- or azo-based compound) is added to the solution and the subsequent thermal decomposition into highly reactive species initiates the polymerization of the monomers leading to radical propagation. As the polymer chains grow, they become insoluble in the reaction medium. Once the polymer chains reach a certain size or critical length, they aggregate and precipitate out of the solution. This leads to the formation of polymer particles or microgels. In the specific case of NIPAAm or VCL monomers, this occurs because the polymerization temperature is far above the LCST of the formed polymers. When the polymerization is completed and the reaction mixture cools down to room temperature, microgel particles swell (temperature below VPTT of polymer chains) and develop a "hairy" morphology. The choice of monomers, initiators, and reaction conditions can be tailored to control the size, morphology, and properties of the resulting polymer particles. The monomer concentration, temperature, amount of cross-linker, the rate of stirring, and the presence of surfactants influence the size, shape, and polydispersity of the resulting microgels.

Microgels of N-isopropyl acrylamide (molecular structure is reported in Fig.2.3) were obtained by surfactant-free emulsion polymerization [100, 101]. As shown graphically in Fig.2.4, the main phases of this synthetic strategy include the polymerization of oligoradicals at a temperature above the VPTT, such polymer-



N-Isopropylacrylamide

Figure 2.3: NIPAM molecular structure.

ization leads to the formation of precursor particles whose growth beyond the critical size determines their precipitation. The microgels thus obtained are then swollen by lowering the temperature below the VPTT. The microgels involved in this work were prepared following the formulation reported in Tab.2.1. In order to prepare fluorescent micron-sized microgels, 1.00 g of NIPAM, 0.03 g of MBA, and 2 mg of Oregon Green 488 were dissolved in 110 mL of MilliQ water in a three-neck flask and stirred at 200 rpm until complete dissolution. The flask was equipped with a water-cooled reflux condenser and the temperature was raised to 43 °C and the solution was purged with nitrogen for 15 min under mixing. The polymerization was initiated by the slow addition of 5 mL of the initiator solution (APS 0.2 g/mL). After 10 minutes of reaction, the solution became turbid due to the phase separation of the pNIPAM chain growing beyond the critical length and its consequent insolubility in water at the reaction temperature. The temperature was raised to 60 °C and after 3 hours the polymer dispersion was rapidly cooled down in an ice bath. The product was then centrifuged and washed twice with MilliQ water.

Table 2.1: Formulation of the micron-sized fluorescent pNIPAM microgels.

Reagent	Quantity (mol)
Water	6.4
NIPAM	$8.8 \cdot 10^{-3}$
MBA	$1.9 \cdot 10^{-4}$
APS	$4.4 \cdot 10^{-4}$

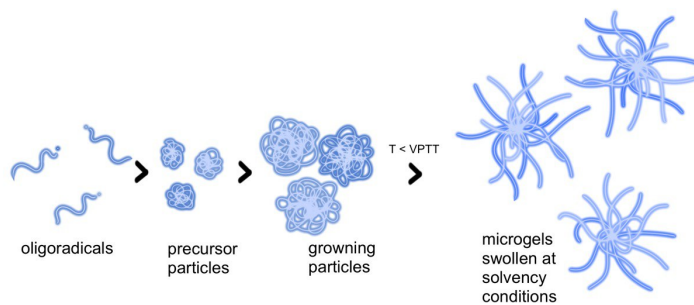


Figure 2.4: Schematic representation of microgels formation and growth [102].

2.1.4 Bacterial culture

Bacillus Subtilis (*B. subtilis*) was chosen as model bacteria in this work because it is a particularly strong pusher microswimmer from the rheological point of view [103]. Analysis of the dynamics of active fluids showed that the presence of self-propelled species such as *B. subtilis*, results in a significant change in apparent viscosity. Simulation studies and experimental demonstrations [104, 105] show how the presence of pushers in Newtonian matrices results in the significant lowering of shear viscosity compared to suspensions of species of similar size and cell shape, but lacking the characteristic propulsive motion. A detailed study of this effect was proposed by Saintillan et al. through his predictive kinetic model [106]. The model explains the effects of the apparent viscosity of torque-free particle suspensions at low Reynolds numbers. Under infinite dilution conditions, the swimming particles undergo ballistic motions, with rare reorientation events due to particle-particle collisions. Saintillan highlighted the stresslet of the matrix resulting from the active stress of the suspended microswimmer in the infinite diluted regime. For dense systems with high cell's volume fraction, the strong deviations from the Saintillan model demonstrated the critical role of collective motion effects, particle transport, and hydrodynamic interaction of the notational particles. These effects are attributable to the dual nature of peritrichous microswimmers such as *B. subtilis* [103], which, through run-and-tumble motion, can act as a pusher or puller under certain conditions.

B. subtilis type strain DMS-10 was purchased from DMSZ (Germany). Following the supplier's instructions the bacterial pellet was reactivated and then the active culture was diluted in fresh tryptic soy broth (TSB) to reach the optical density of approx-

imately 1 measured at the wavelength of 600 nm (OD_{600}) with a Thermo Scientific NanoDrop OneC UV-Vis Spectrophotometer. An overnight culture of *B. subtilis* was prepared for each experiment by inoculation of one colony in 5 mL TSB at 32 °C under agitation at 260 rpm. The stationary phase was confirmed thanks to the measure of OD_{600} of the bacterial dispersion at intervals of 30 minutes. To maximize the number of motile cells, the bacterial dispersion was diluted to $OD_{600} = 0.15$ in fresh TSB and kept at the growing conditions for 30 minutes. Direct visualization of the motile cells was performed by staining *B. subtilis*'s cells with SYTO9 directly on the activated dispersion. The dye solution was added to the bacterial dispersion to a final concentration of 10 vol% and kept under soft agitation for 15 minutes in the dark. The final bacterial dispersion was sufficiently diluted to minimize local gradients of oxygen or nutrient concentration and intercellular interactions throughout the entire media.

2.2 Experimental techniques

2.2.1 Swelling behavior and water state

Polymeric systems derived from the cross-linking of monomers or macro-monomers through covalent bonds do not dissolve in solvents, instead, such networks evolve towards an equilibrium solvent concentration with a concomitant increase or decrease in volume. This process, known as swelling behavior, reaches equilibrium according to the balance between the free energy of polymer-solvent mixing and the free energy cost of expanding the network, which is expressed by the Flory-Rehner equation for isotropic swelling of an affine polymer network [14, 107]. The Flory-Rehner equation has however several limitations. The equation is primarily applicable to polymer networks prepared under solvent-free conditions, while gels are usually prepared in solvent media. Moreover, the mixing free energy estimated from Flory and Rehner's approach underestimates correlations between monomers along the same polymer chain [108] and assumes a Gaussian distribution of chain conformations, an assumption that may not accurately represent the actual distribution of polymer chain conformations in all cases. The swelling behavior of polymeric systems under various environmental conditions and their equilibrium state provide important information on their microscopic and macroscopic characteristics. It should be noted that the swelling of gels provides evidence for their porosity. Water content plays a key role in defining the physico-chemical properties of polymer systems and their application in many areas of science and technology, from biology to food science. Especially in hydrogels, it plays an important role in supporting their integrity and mechanical properties, solubil-

ity, and diffusion of substances, which are crucial features for biomedical, biotechnological, and environmental applications. In particular, the equilibrium water content (EWC) and the hydration degree (HD) reflect the network hydrophilicity and they can be easily obtained as follows:

$$EWC = \frac{W_w - W_d}{W_w} \quad (2.1)$$

$$HD = \frac{W_w - W_d}{W_d} \times 100 \quad (2.2)$$

where W_w and W_d are the weights of the swollen and completely dried gels, respectively. Crucial for the complete understanding of the physico-chemical properties of hydrogels is not only the determination of the total content of water but also the distinction and determination of the fractions of 'primary bound water', 'secondary bound water', and 'free water' [109–111]. In an equilibrated hydrogel, the first water molecule layer directly bound to the hydrophilic groups of the polymer network ('primary bound water') represents the non-freezable water fraction. Behind this first layer gathers the 'secondary bound water' molecules that 'feel' the polar groups of the polymeric network attenuated by the primary bound water. The extra water loaded in the hydrogel that is not affected by these polar groups can be considered as 'free water' since it behaves as if it were in the bulk. In order to quantify the amount of the different types of water in the synthesized hydrogels, differential scanning calorimetry (DSC) was carried out with the DSC 2500 Discovery (TA) instrument under a constant nitrogen flow rate of 50 mL/min. Small pieces of equilibrated gels (10 to 20 mg) were analyzed in an aluminum pan applying a heating rate of 0.5 °C/min, from –60 to 20 °C and the related heat flow was automatically normalized by the initial

weight of the sample. The low heating rate allows the observation of two endothermic peaks, a first broader peak that ranges from $-10\text{ }^{\circ}\text{C}$ to $-40\text{ }^{\circ}\text{C}$, associated with freezable bound water, and a second one at $0\text{ }^{\circ}\text{C}$, proper of the freezable free water. Since the 'primary bound water' does not undergo freezing even below $70\text{ }^{\circ}\text{C}$ it can only be calculated from the total water content of the 'secondary bound water' and the 'free water'. Consistent with the following equations, from thermograms, it is possible to quantify free and bound water index (FWI, BWI), and the free and secondary bound water mass for the unit mass of polymer, C_{fw} and C_{bw} respectively:

$$FWI = \frac{\Delta H_{\text{exp}(T \approx 0\text{ }^{\circ}\text{C})}}{EWC \times \Delta H_{\text{theo}}} \quad (2.3)$$

$$BWI = \frac{\Delta H_{\text{exp}(T < 0\text{ }^{\circ}\text{C})}}{EWC \times \Delta H_{\text{theo}}} \quad (2.4)$$

$$C_{\text{fw}} = \frac{x_w \times FWI}{x_p} \quad (2.5)$$

$$C_{\text{bw}} = \frac{x_w \times BWI}{x_p} \quad (2.6)$$

where $\Delta H_{\text{exp}(T \approx 0)}$ and $\Delta H_{\text{exp}(T < 0)}$ (J/g) correspond to the melting heat of the 'free water' and 'secondary bound water' respectively; those values are obtained from the integration of the endothermic peak around $0\text{ }^{\circ}\text{C}$ and from $-10\text{ }^{\circ}\text{C}$ to $-40\text{ }^{\circ}\text{C}$ of the DSC curves, while ΔH_{theo} is the theoretical value of the specific enthalpy of fusion of water at $0\text{ }^{\circ}\text{C}$ (333.6 J/g) [112].

2.2.2 Structural characterization

The topological structure of a gel, together with its chemical composition, determines the properties of the resulting polymer network. The topology of a polymer network refers to the spatial arrangement and connectivity of polymer chains within the network. It describes how the polymer chains are linked or cross-linked, forming a three-dimensional structure. The specific topology of a polymer network significantly influences its physical and mechanical properties (e.g., elasticity, porosity, and swellability). Understanding and controlling the topology of a polymer network is crucial for tailoring its properties for specific applications. Amorphous or semi-crystalline polymeric systems expose plenty of topological features ranging on various length scales, from molecular to the sub-micro-metric level. At the nanoscale, between 10 and 100 nm, the topology is characterized by inhomogeneity in junction/strand density, dangling chains, entanglements, and loops of various orders comprise the macromolecular features that dominate network structure. A wide range of scattering techniques are constantly used to characterize structural and topological features of polymeric networks. Based on the type of network (i.e., amorphous, or crystalline), different approaches are more informative than others. Nevertheless, all scattering techniques involve radiation exposure of the sample and measurement of the intensity of scattered radiation as a function of the modulus of the scattering vector q :

$$q = \frac{4\pi \sin(\theta)}{\lambda} \quad (2.7)$$

where 2θ is the angle between the incident radiation and the detector measuring the scattered intensity and λ is the wavelength of incident radiation. Small-angle scattering (SAS), which

collects and analyzes scattering at small angles ($q < 0.5 \text{ \AA}^{-1}$), is particularly appropriate for studying materials with structural features on the order of 1 to 100 nm [113]. Techniques including static light scattering (SLS), small-angle neutron scattering (SANS), and small-angle X-ray scattering (SAXS) are powerful tools for studying the topology of polymer networks on this length scale.

Small-angle X-ray scattering

The nanoscale topology and structure of the polymeric networks were investigated using a Xeuss 3.0 HR apparatus (Xenocs, France), equipped with an EIGER2R (1 M model) hybrid pixel photon counting detector (Dectris Ltd., Switzerland) consisting of 1028×1062 pixels with a size of $75 \times 75 \mu\text{m}^2$. A sealed Cu tube powered by a Genix 3D generator (i.e. 30 W) provides the X-ray beam corresponding to the $K\alpha$ ($\lambda = 1.5406 \text{ \AA}$) while the calibration of the sample-to-detector distances, 500 to 1800 mm, was performed with silver behenate standard ($d = 58.376 \text{ \AA}$) [114]. In order to minimize the air scattering the experiments were performed under vacuum and the hydrogels were analyzed in a sealed sample holder of 1 mm of thickness using windows of Kapton[®]. The experimental conditions allow the acquisition of profiles in the scattering vector, q , ranging from 0.004 to 0.55 \AA . The obtained scattering profiles were converted in absolute intensity (mm^{-1}) by the secondary standard (i.e., glassy carbon) [115] and reduced by subtracting the scattering intensity from the empty holder + water. All the data processing was performed through XS-ACT (X-ray Scattering Analysis and Calculation Tool) software (Xenocs, France).

The SAXS profile of polymer gels can be interpreted according

to a generalized Debye-Bueche model [116], which describes the polymeric network as the superposition of two q -dependent contributions and the instrumental background:

$$I(q) = I_{\text{sol}}(q) + I_{\text{ex}}(q) + bkg \quad (2.8)$$

The first term $I_{\text{sol}}(q)$ corresponds to the scattering from the homogeneous polymer solution, represented by the generic Ornstein-Zernike equation [117]:

$$I_{\text{sol}}(q) = \frac{I_{\text{sol}}(0)}{[1 + (\zeta q)^m]} \quad (2.9)$$

where the scattering intensity at $q = 0$, $I_{\text{sol}}(q)$, reflects the polymer-solvent contrast and the volume fraction of the polymer in the gel, ζ represent the characteristic average mesh size of the polymeric network, and m is the Porod exponent related to the polymer-solvent interactions [118].

On the other hand, the second term ($I_{\text{ex}}(q)$) represents the excess of scattering rising from the solid-like inhomogeneities in the gels. These inhomogeneities arise from the non-homogeneous spatial distribution of polymer chains as a result of fluctuation in crosslinking density, separation of microphases due to polymer fraction or degree of ionization, and can be classified into three categories: spatial, topological and connectivity [119]. This excess of scattering is represented by the squared Lorentz or Gauss functions [120].

$$I_{\text{ex}}(q) = \frac{I_{\text{ex}}(0)}{(1 + a^2 q^2)^2} \quad (2.10)$$

where the excess of scattering intensity at $q = 0$ is represented by $I_{\text{ex}}(q)$ and a describes the length scale of the inhomogeneities domains in the gel.

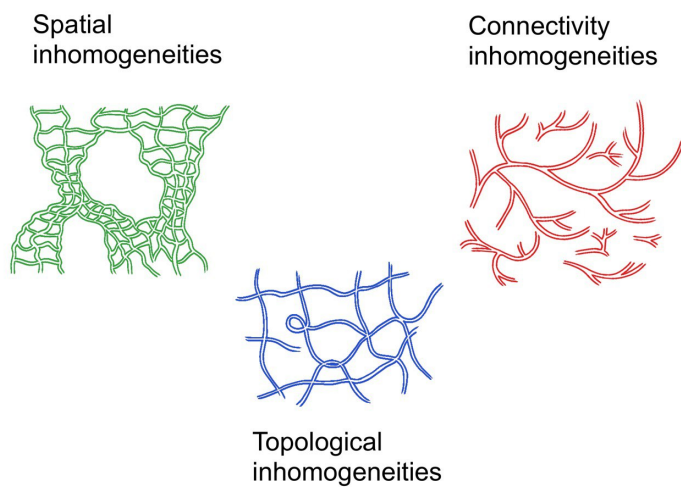


Figure 2.5: The multi-length scale complexity of polymer network topology: The topological features of amorphous polymer networks can be categorized into at least three different length scales: 10-100 nm (shown in green), 1-10 nm (shown in red), and <1 nm (shown in blue).

2.2.3 Morphological characterization

Morphology, referring to the qualitative and quantitative evaluation of a bi-dimensional or three-dimensional network, is the description of the shape, structure, and physical characteristics of materials or biological entities at various levels of detail, ranging from the macroscopic to the microscopic and even nanoscopic scale. Structural characterization of materials is crucial in many fields of science, for industrialists to have complete control over their manufacturing products: in biology, it includes physical attributes and is fundamental to understanding how an organism or an apparatus functions and interacts with the environment; In the context of the hydrogels, composition, cross-linking degree, presence of different co-monomers or co-polymers, and preparation method impact the morphology and so the potential application of these systems. For these reasons, the profound and detailed morphological characterization and how the structure can be modified and precisely tailored represent an aspect of primary importance allowing the understanding of the physical structure at a detailed level of the micron scale. Milestones in the structural investigation of the morphological features are represented by microscopy techniques such as microscopic analysis under optical, scanning, or transmission electron microscopy, and fluorescence microscopy.

In the present work, the structure of the synthesized hydrogels was investigated by scanning electron microscopy (SEM), and confocal laser scanning microscopy (CLSM).

Scanning electron microscopy

SEM investigation on the freeze-dried (xerogels) was performed by means of a FEG-SEM SIGMA microscope (Carl Zeiss, Ger-

many) using an acceleration potential of 2 kV and a working distance of about 3 mm. Under these conditions, the metallization of the samples was not necessary. All the investigated hydrogels were previously lyophilized by the freeze-drying process ensuring the complete water removal and preserving their structural characteristics. The swollen hydrogels were frozen by immersion in liquid nitrogen for 5 minutes and then dried at -55 and 40 mtorr of pressure overnight. The ice crystals generated during the freezing process act as a porogen within the polymeric network.

Laser scanning confocal microscopy

Imaging of hydrogel volumes was carried out using a Leica TCS SP8 confocal microscope. Lab-Tek Chambered Coverglass with 1.0 borosilicate glass bottom was used as sample holders. A 63 \times oil immersion objective with N.A. = 1.43 was used for all experiments. All the synthesized hydrogels were investigated in their hydrated state after complete equilibration before and after the freeze-drying process. In order to perform the imaging of the polymeric network, all the samples were labeled with RhB by immersion in dye solution for 72 hours to allow physical adsorption of the dye within the polymeric network. The affinity between RhB and the PEG results in the physical adsorption of the dye to the polymeric network, allowing the spontaneous and efficient labeling of the hydrogel structure. Due to that, no washing cycles were required to remove the dye solution excess. The fluorescent probe was excited with a laser having a wavelength of 561 nm, and the fluorescence emission was acquired using a highly efficient hybrid detector in the 600 - 700 nm range. 3D image stacks of 1024 \times 1024 \times 40 pixels³ were acquired, which correspond to hydrogel volumes of 90 \times 90 \times 40 μm^3 .

Analysis of the porosity

Morphological and structural characterization were extrapolated from the volumetric image stacks acquired by confocal microscopy. The so obtained three-dimensional stacks were analyzed through MorphoLibJ, a specific collection of mathematical morphology methods for ImageJ [121, 122], to extrapolate geometrical, structural, and morphological features of the observed porosity. In order to distinguish individual pores within the void space and correctly extract the morphology parameters, the 3D scans were first binarized in 8-bit images and then optimized and processed by the "distance transform watershed" [122] method. This method allows the determination and three-dimensional reconstruction of the pores by disentangling the touching pores. From the pores reconstructed in this way as individual solid objects, the porosity of the hydrogels was calculated and used to obtain the pore volume fraction (Φ) according to Eq. 2.11.

$$\Phi = \frac{\sum_i V_{\text{pore}}^i}{V_{\text{tot}}} \quad (2.11)$$

where V_{pore}^i indicates the volume of pore i . Moreover, from the 2D sections of the stacks, the mean diameter of the equivalent circle for each detected object, $\langle d \rangle$, was extracted. These values were used to calculate the pore area fraction (α), defined as the total area of the pores in the investigated 2D plane normalized by the total area of the 2D plane:

$$\alpha = \frac{\sum_i A_{\text{pore}}^i}{A_{\text{tot}}} \quad (2.12)$$

where A_{pore}^i is the area of pore i . The MorphoLibJ tool "Analyze regions 3D" not only allows the determination of the volume

and surface of each detected pore but moreover it allows the extrapolation of characteristic geometrical parameters. For each sample, the ratio of the squared volume over the cubic surface area was calculated to obtain the normalized sphericity index (Eq. 2.13). In order to do this from the volumetric stacks the pores on the edges were previously removed to avoid bias on the geometrical data processing.

$$\text{Sphericity} = 36\pi \frac{V^2}{S^3} \quad (2.13)$$

Finally, this tool allows to assess the pore geometry and symmetry of the pores by the extrapolation of three characteristic lengths of the ellipsoid that best fits within a pore, called R_1 , R_2 and R_3 (referred to the three axes of the ellipsoid) in decreasing order of magnitude, as well as the elongations defined as the lengths' ratios: R_1/R_2 , R_1/R_3 , R_2/R_3 . In order to support the morphology characterization, the so obtained parameters were compared to the average pore diameter obtained from the same images and processed through the ImageJ software "count particles" method. This method, applied at different heights of the collected volumes returned the area and the diameter of the equivalent circle for each detected pore.

2.2.4 Rheological behavior

Rheological characterization is a common and convenient method for studying the mechanical properties and shear response of materials, particularly hydrogels. It focuses on understanding the relationship between stress application and resulting deformation to define the material's mechanical properties. Two types of responses are obtained depending on the type of stress applied. The linear responses are due to stresses that cause deformations that disturb the structure of the material without, however, significantly changing it (the amplitude of the deformation is small, and can be compared to a perturbation). The non-linear responses, on the other hand, are due to stresses that cause deformation to the internal structure (for example, an irreversible deformation). According to the Winter-Chambon Criterion [123], a gel can be defined as a material that has reached its gel point, where the elastic modulus (G') is equal to the viscous modulus (G''). In other words, a gel is a system in which the solid-like behaviour (elasticity) and the liquid-like behaviour (viscosity) are balanced, resulting in a material that exhibits properties of both a solid and a liquid. Gels, defined as polymeric networks dispersed in a fluid, have intermediate characteristics between solids and liquids and a rheological response typical of a viscoelastic solid: the elastic modulus $G'(\omega)$ has an almost frequency-independent value in the experimental measurement window, significantly greater than the viscous modulus $G''(\omega)$ [124].

Rheology measurements were carried out using a DHR-3 hybrid rheometer from TA instruments equipped with parallel plate geometry of 20 mm diameter in stainless steel, at 23 °C temperature controlled by a Peltier plate. The software TRIOS allows the data acquisition and processing of the rheological analyses. In order

to assess the linear response range of the synthesized hydrogels, which represents the range over which the viscoelastic modules are independent of the amplitude of the oscillation, measurements were carried out by increasing the amplitude of the oscillation at a constant frequency ($\omega = 1$ rad/s). In the so-determined linear response regime, measurements were then carried out at constant amplitude, $\gamma_0 = 0.3\%$, in the frequency range from 100 to 0.1 rad/s, in order to measure the linear viscoelastic modules $G'(\omega)$ and $G''(\omega)$.

2.3 Particle Tracking

2.3.1 Single particle tracking method

Mobility is a key factor that determines the behavior of colloidal systems with a huge impact on various applications such as drug delivery, industrial processes, environmental science, and medicine. Among the several parameters that affect colloids' transport properties, confinement represents one of the most labor-intensive processes requiring a set of different techniques. Confinement by rigid obstacles or soft matrices alters the transport properties of particles in complex media with significant consequences in many application-relevant processes. For example, nano or micron-scale cargos diffuse through the crowded cytoplasm and through a network of rigid microtubules and/or semi-flexible actin filaments. Separations in size-exclusion chromatography, micro-filtration, anti-viral strategies, and selective absorption represent a few examples of the multitude of scenarios where diffusion is hindered by confinement.

Here, the single particle tracking method (SPT) is used to monitor and analyze the movements of individual particles over time in the different confining systems allowing us to test the dynamics and interactions of particles in such complex matrices. This technique is particularly valuable in various fields, including physics, biology, chemistry, and materials science; developed in the 1980s to investigate the movements of individual particles or molecules, SPT is usually applied to fluorescence microscopy (but can be applied also to other contrast conditions) by tracking a fluorescent entity over time in order to extrapolate quantitative analysis of dynamic processes from time-lapse image data. The particles of interest in this technique can range from 10 nm up

to micron-sized objects with the only prerogative that these have a strong contrast with the background in order to be easily distinguished and tracked. Due to this, the objects of interest are usually labeled with one or more fluorescent probes. The conventional SPT setup basically involves a fluorescent microscope with a high-power light source and a sensitive camera with high spatial and temporal resolution [125]. In order to extrapolate the dynamic and reconstruct the trajectories performed, it is essential to localize and follow the investigated objects over time with confidence. Automated computational methods have been developed for these tasks by many groups. Typically, a standard SPT algorithm locates all the identified objects at each frame and calculates the probability of connecting each object at a specific frame t to the subsequent frame $t+1$. This probability can be calculated based on several different parameters: proximity, motion speed, brightness, etc. Afterward, the algorithm chooses the solution that maximizes the overall probability.

2.3.2 Instrumental setup

The instrumental setup described for the three-dimensional imaging of the hydrogels was also used for the particle tracking measurements. In addition, two high-efficiency hybrid detectors were used in parallel to simultaneously detect the fluorescence emitted by the confining matrices and the colloids/bacteria. For the visualization of the hydrogel, as explained previously, the detector is set to acquire the fluorescent emission of rhb between 560 - 600 nm; for the visualization of the dynamic system, pNIPAM microgel or *B.subtilis* that are marked respectively with Oregon Green and SYTO9, the second detector was set for fluorescence acquisition between 498 - 550 nm. As it can be seen from the emission spectra of the two markers in Fig. 2.6, the simultaneous acquisition is not subject to bias resulting from band overlap. Time-lapse images of 512×512 pixels were acquired with a spatial resolution of $0.0903 \mu\text{m}$ per pixels, corresponding to a total investigated area of approximately $50 \times 50 \mu\text{m}^2$. Videos of 2000 frames with a time interval of 0.0362 s were acquired for a total experimental time per analysis of about 80 s. All measurements were conducted at room temperature. The tracking algorithm used to reconstruct the trajectories and extrapolate the characteristics of transport parameters was Trackpy v0.50 [126]. Trackpy is a package for tracking dot-like objects in video images, following them through time, and analyzing their trajectories. It is a Python compact and flexible implementation of the widely-used Crocker-Grier algorithm [121]. The software allowed the correction of any background drift, which might be due to large-scale flow or any microscope stage movement. The ensemble mean squared displacement (MSD) of all particles was computed using the "emsd" function in Trackpy. Parallel to this tracking

method, we also used TrackMate and TrackClassifier, two Fiji plugins, to analyze the single trajectories and their characteristic features [127–129]. These two methods coupled allow for extrapolation of the speeds performed in each trajectory and even split and classify into segments of normal diffusion, sub-diffusion, confined diffusion, and directed/active motion. In Track-Mate the Difference of Gaussian (“DoG”) detection algorithm was applied to automatically detect the bacteria in the acquired image time-series. trajectories were reconstructed through the Linear Assignment Problem (LAP) particle-tracking algorithm [130]. The obtained trajectories were classified through TrajClassifier.

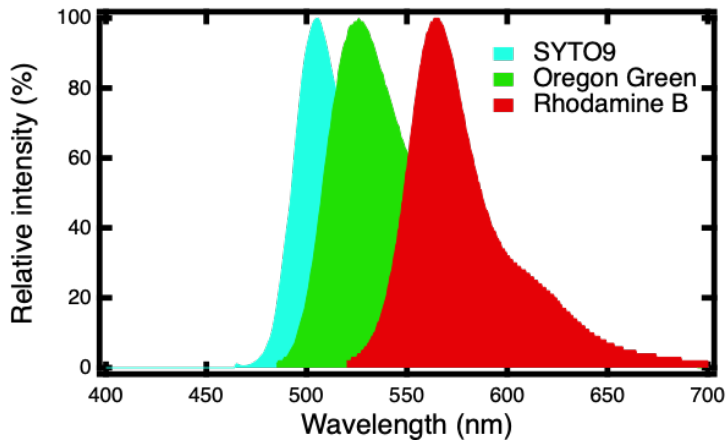


Figure 2.6: Emission spectra of the fluorescent dyes used in this work: SYTO9 in cyan, Oregon Green in green, and Rhodamine B in red.

Chapter 3

Results and discussions

This chapter presents the main results with the corresponding discussion. For each section, the results with relative interpretations are reported.

3.1 PEG-based hydrogels

3.1.1 Synthesis and swelling behavior

Polyethylene glycol hydrogels, prepared according to the procedure given in section 2.1.2, have considerably high transparency and, once immersed in water, have significantly increased their mass. All synthesized hydrogels increased their mass more than 300 times during the bulging process, eventually reaching the water content at equilibrium within the first 24 hours. As shown in Fig. 3.1 in which an exemplary hydrogel with PEG content of 20 wt% was photographed through the various stages of post-synthesis treatment, after freeze-drying Fig. 3.1(c) and rehydration (Fig. 3.1(d)), all samples kept a good degree of transparency, showing slight opacity after the treatment compared to the initial state before freeze-drying (Figs. 3.1(a-b)). The small loss of transparency shown in Fig. 3.1(d) is related to the structural changes at the microscale induced by the freeze-drying process, which induce the consequent change of the refractive index of the substrate once rehydrated.

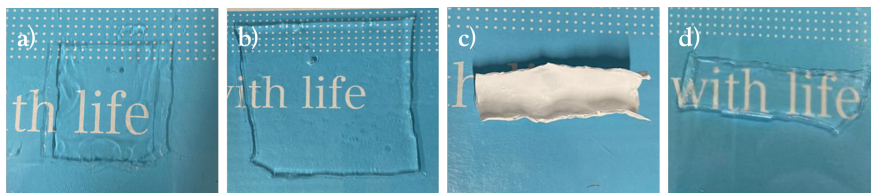


Figure 3.1: Exemplary pictures of a PEG hydrogel (P20) in the different hydration phases; as prepared (a) and at the equilibrium water content (b), after complete lyophilization (c), and rehydration (d).

The hydration kinetics of the PEG hydrogels were reconstructed by monitoring the weight change during the complete

rehydration in water of initially lyophilized samples. The samples' weight was measured after gently removing the surface moisture with paper. As clearly observable from the swelling profiles reported in Fig. 3.2(a), all the samples reached the equilibrium water content (EWC) after the first 10 hours of immersion. The EWC values of the swollen hydrogels showed no significant differences between the samples, reporting a slight decrease with the increase in the concentration of macro-monomer in the pre-reaction mixture (see Fig. 3.2(b)).

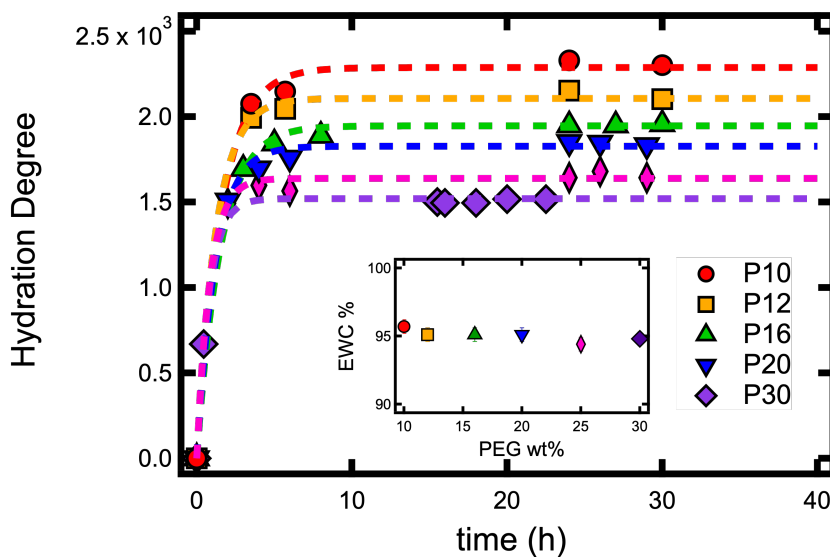


Figure 3.2: Hydration kinetics of the PEG freeze-dried gels (as indicated in the legend) in MilliQ water after the lyophilization process in the main graph and the reached EWC of each synthesized hydrogel in the inset. Dashed lines the fitting curves of the experimental data

Information on the absorption and permeation properties of the investigated gels was extracted from the DSC thermograms. In particular, from the obtained data it was possible to distinguish the different states of water and calculate the relative

amount of imbibed water in each state. As is clearly observable from Fig. 3.3(a), there are two distinct melting peaks in the normalized heat flow measured by DSC associated to the different water types discussed in Sec.2.2.1: one main sharp peak corresponding to the melting of bulk water (≈ 0 °C) and a less pronounced one corresponding to the melting of 'secondary bound water' (≈ -12 °C). The water masses per gram of gel reported in Fig. 3.3(b) indicate a significant change in the state of the water absorbed in the polymeric network as a function of the macro-monomer concentration in the synthesis mixture; although the amount of free (bulk) water per mass of polymer (C_{fw}) remains almost constant, the amount of secondary bound water (C_{bw}) shows a consistent increase as a function of the concentration of macro-monomer in the pre-reaction mixture. The non-monotonous trend exposes a sudden decrease for the PEG concentration greater than 20 wt%, which can be attributed to a drastic reduction of the porosity and consequently to the smaller polymer surface exposed to water.

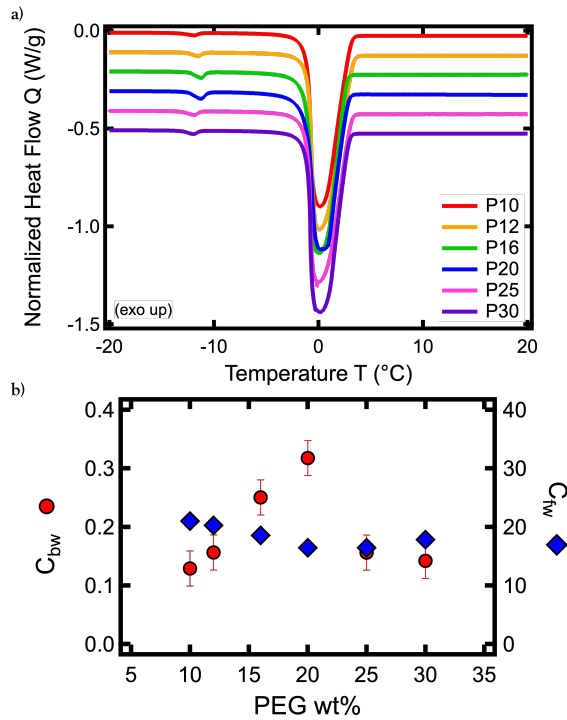


Figure 3.3: Differential scanning calorimetry thermograms of investigated hydrogels(a). The thermal profiles are reported shifted along the y-axis for clarity. The fractions of bound and free water for gram of polymer calculated using Eq. 3.6 and 2.6 are reported as a function of the structural component (Error bars for blue diamonds in (b) are smaller than the marker size).

3.1.2 Nanoscale topology

In order to investigate the nanostructure of the PEG hydrogels and the topological changes associated with the macro-monomer content in the pre-reaction mixture, SAXS experiments were carried out. The intensity profiles obtained for all the samples show a pronounced forward scattering, reflecting the presence of large-scale structures with an inflection approaching q values of 0.1 \AA^{-1} . In order to relate the topological features with the macro-monomer content, the generalized Debye-Bueche model introduced in Sec. 2.2.2 Eq.2.8 was applied to interpret the scattering profiles of the PEG hydrogels after the subtraction of the scattering contributions of water and the Kapton window. The first term of the equation is a generic version of the Ornstein-Zernicke model [117] which gives information on the cross-linked polymer chains that constitute the hydrogel's network and characterizes the high- q region of the scattering profiles. On the other hand, the region at low- q reflects features typically attributed to the network inhomogeneities. The Ornstein-Zernicke [117] term describes the scattering from the mesh forming the network structure in terms of the average mesh size (or correlation length, ζ), and the Porod exponent m associated with the solvent-polymer interactions. The low- q forward scattering term is dependent on the length scale of the solid-like inhomogeneities a of the gel. The topological parameters extrapolated from the fitting of the scattering profiles using Eq.2.8 are listed in Tab. 3.1 and summarized in Fig. 3.4. The exponential decrease of the average mesh size as a function of the PEG concentration in the pre-reaction mixture (Fig. 3.4b), going from $\approx 8 \text{ nm}$ at 10 wt% to $\approx 2 \text{ nm}$ at 30 wt% of PEG, suggests a consistent decrease of the pore volume fraction related to a more interconnected polymeric

network. The fitted Porod exponents m are found to increase with the increase of the PEG concentration (Fig. 3.4c), The Porod exponent reflects the local morphology of the investigated network and is a powerful tool for assessing the polymer-solvent interactions; it is known that this parameter is equal to 1.67 for linear polymer in good solvent conditions and reaches 2 under *theta* solvent conditions [131], in which there are no preferential polymer-polymer nor polymer-solvent interactions. In a simplified interpretation of the Porod approach, m decreases with the polymeric network's expansion while increases when the network collapses. During freeze-drying, the ice-crystal nucleation and growth act as a porogen agent, collapsing the polymeric chains while enhancing the polymer-polymer interactions and reducing the polymer-solvent interactions similar to what was observed for PVA cryogels [132]. As a result of this phenomenon, the higher the concentration of macro-monomer concentration, the higher its resistance to structural deformation and its compactness, which is reflected by a larger Porod exponent. For samples with PEG concentration between 10 and 16 wt% the Porod values suggest *theta* solvent-like conditions, $m \approx 2$. Increasing the PEG content, the Porod exponent increases reaching the value of 3 for 25 wt% of PEG in the pre-reaction solution. This situation reflects a completely collapsed system where the interaction with the solvent is minimized. The higher value found for P30 indicates a transition from a mass fractal to a surface fractal system [133]. As clearly observable from Fig. 3.4(b), the macro-monomer content also affects the solid-like inhomogeneous domains, decreasing their average size (see a value) with increasing PEG content, in agreement with the collapsing phenomenon described by the m exponent. On the other hand, the intensities ratio ($I_{\text{sol}}(0)/I_{\text{ex}}(0)$, see Fig. 3.4(c)) gives information about the relative weight of

the scattering from the mesh structure of the polymer network compared to the one of solid-like inhomogeneities; the increasing trend with the macro-monomer content in the pre-reaction mixture is consistent with the increasing compactness of the hydrogel and therefore the more dominant contribution of the mesh structure.

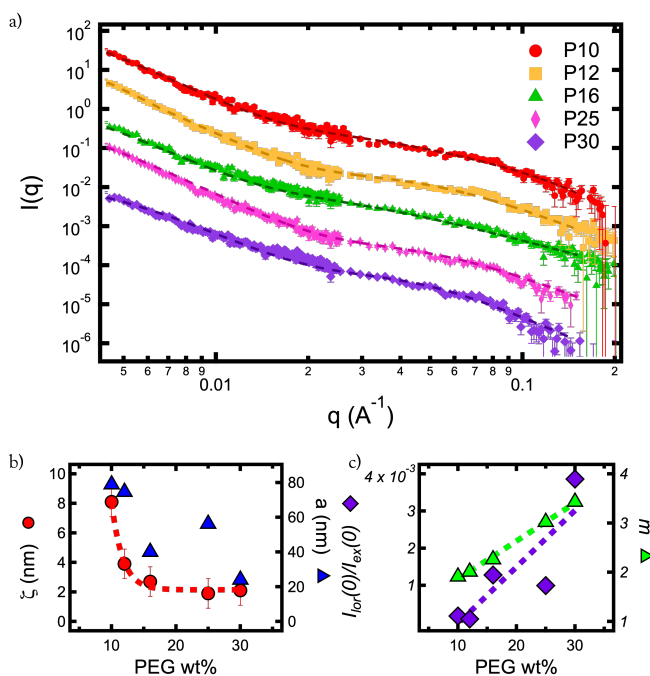


Figure 3.4: SAXS profiles of porous PEG hydrogels after equilibration, freeze-drying, and re-hydration (a). Experimental data are reported as full markers together with fitting curves (reported as dotted lines). The curves are shifted along y-axes for clarity. Average mesh size and solid-like inhomogeneities domains of the PEG hydrogels as a function of the structural component in the pre-reaction mixture (b). The scattering intensities ratio and the Porod exponent as a function of the structural component (c).

Table 3.1: Fitting parameters obtained from the modeling of the SAXS curves for the different PEG hydrogels according to Eq. 2.8

Sample	$I_{\text{lor}}(0)$ (10^{-2})	ζ (nm)	m	$I_{\text{ex}}(0)$ (10^{-2})	a (nm)
P10	4.08 ± 0.01	8.1 ± 0.5	1.91 ± 0.05	233.4 ± 0.2	78.9 ± 0.8
P12	1.42 ± 0.01	3.9 ± 0.5	2.01 ± 0.02	353.3 ± 0.2	74.6 ± 0.8
P16	1.08 ± 0.01	2.7 ± 0.5	2.26 ± 0.02	8.5 ± 0.1	29.9 ± 0.7
P25	0.50 ± 0.10	1.9 ± 0.5	3.02 ± 0.02	12.9 ± 0.5	59.2 ± 0.7
P30	0.80 ± 0.10	2.1 ± 0.5	3.43 ± 0.01	2.1 ± 0.4	24.9 ± 0.7

3.1.3 Morphological characterization

The morphology and porosity of the prepared hydrogels were investigated through LSCM and SEM. Confocal microscopy analysis carried out on hydrogel samples before and after the freeze-drying treatment highlighted the importance of this process for the formation of porosity at the micron scale. Confocal imaging of the hydrogels as-synthesized and equilibrated in water shows that no clear micron-scale inhomogeneities are present (see Fig. 3.5(a)). As observed for the lyophilized hydrogels in the swollen state, reported in Fig. 3.5(b), the freeze-drying process induces the desired porosity in the polymeric network (Figs. 3.5(c) and (d)). Consistent with the expectations, the induced porosity is affected by the PEG content in the pre-reaction mixture; this effect is already apparent in the volumetric image stacks reported in Figs. 3.5(c) and (d) for samples P10 and P20. It is even more clearly observable in the 2D images reported in Fig. 3.6: there is a progressive reduction of the pore size related to the increase of the macro-monomer concentration up to 20 wt%. A critical change in the morphological structure was observed for concentrations greater than this value; the channel-like morphology exposed in the low-concentration regime suddenly changed to a closed-cell-like structure with a few smaller pores that appeared as localized inhomogeneities in the more compact polymeric network. In order to support the LSCM evidence, the hydrogels' morphology was also investigated through SEM imaging of the lyophilized samples. Dehydrated gels were fractured and their internal structure was observed at the electron microscope to collect qualitative information on the structure at the microscale. Consistent with the confocal imaging, the polymeric structures showed a highly interconnected porous network with

significantly different patterns for the sample with a high concentration of PEG. However, it was not possible to extrapolate quantitative information on the morphology of the investigated samples due to the strong biases induced by the treatment of the samples for SEM analysis; as shown in Fig. 3.7 the polymeric structures, although distinctly porous, were collapsed in the freeze-drying treatment. On the other hand, the 2D imaging performed through confocal microscopy allowed a first quantitative analysis of the pore size through the determination of the average pore diameter $\langle d \rangle$. In perfect agreement with the qualitative observations discussed earlier, the pore diameter decreases from 12 to 6.5 μm when the macro-monomer concentration increases from 10 to 20 wt%, with a roughly linear decrease (see Fig. 3.8); over the threshold value of 20 wt% the increase of the PEG amount in the pre-reaction mixture results in a poorly interconnected close-cell-like network with few pores with a mean diameter of $\approx 4 \mu\text{m}$. The three-dimensional structural analysis gave important morphological information on the polymer porous network; the 3D reconstruction of the porosity through MorphoLibJ [122] allowed the correct distinction of each pore in the hydrogel's portion contained in the volume stack, as evidenced by the results of the software analysis reported in Fig. 3.5(c) for two exemplary hydrogels (P10 and P20). Each pore in the investigated volume was labeled with a different color and analyzed to determine the pore volume fraction (according to Eq. 2.11) and the geometrical features, after preliminary removal of the objects on the edges, as defined in Eq. 2.13. The morphological analysis highlights the relationship between polyethylene glycol (PEG) content and pore volume fraction; two different regimes can be identified: as the PEG content increases from 10 wt% to 20 wt%, there is a linear reduction in the pore volume

fraction, with the initial average pore volume fraction of 63% for 10 wt% PEG which decreases linearly to 48% for 20 wt% PEG; The reduction in pore volume fraction agrees with the saturation of pore size, as revealed by 2D analysis. This implies that up to 20 wt% PEG content, the polymeric network is responding in a way that is reflected in both pore volume fraction and pore size. Beyond 20 wt% of PEG content, the linear relationship between PEG content and pore volume fraction disappears. There is a significant change, and the pore volume fraction is dramatically reduced. Pore volume fraction drops to 7% and 4% for PEG content of 25 wt% and 30 wt%, respectively. This indicates a critical point where the influence of PEG on the polymeric network induces a critical morphological change in the hydrogel structure. As already mentioned, the structure of these two hydrogels with a high content of macro-monomer appeared more compact (Fig. 3.6), presenting few pores without clear interconnection. The 3D analysis of the pore volume fraction confirms thus the presence of a small fraction of pores, supporting the interpretation that the high content of PEG does not allow the generation of a completely interconnected porous network.

An even more detailed analysis of the porosity involved the determination of the sphericity index and the elongation of pores based on 3D images and the reconstructed porosity carried out with MorphoLibJ. To ensure accurate and reliable data, pores located at the edges of the image were excluded from the geometrical analyses. This exclusion helps to focus the analysis on internal pores and prevents potential distortions at the edges. Pores' elongation revealed the presence of channel-like pores with preferential directional elongation in the 1 direction, as illustrated in Fig. 3.5 with a reference system. The results reported in Table 2 indicate the presence of channel-like pores. As reported in Tab.

3.2, there is also a relatively pronounced asymmetry in the 2â3 plane, with elongation occurring along the 2 direction. Although the elongation ratios may not show significant changes with increasing PEG content, except possibly for the 20 wt% sample, the evidence suggests that this lack of significant change does not necessarily mean that the pore structure is unaffected. The fewer pores in the high PEG content samples show a more self-similar shape; these features can be related to the porogen agent used to induce the desired porosity (i.e., ice crystal) [134,135] the effect of which is drastically reduced as the concentration of PEG in the pre-mixture becomes larger than 25 wt%.

Table 3.2: Characteristic geometrical parameters of the pores in the PXX hydrogels' network (XX is the wt% of PEG in the pre-reaction mixture)

Sample	ϕ (%)	Sphericity	R1/R2	R1/R3	R2/R3
P10	62.6	0.15 ± 0.05	1.7 ± 0.2	2.8 ± 0.3	1.6 ± 0.2
P12	59.9	0.40 ± 0.08	1.5 ± 0.2	2.7 ± 0.4	1.6 ± 0.1
P16	59.4	0.28 ± 0.03	1.6 ± 0.2	2.5 ± 0.1	1.6 ± 0.1
P20	48.0	0.30 ± 0.04	2.2 ± 0.2	4.1 ± 0.3	1.9 ± 0.2
P25	6.6	0.19 ± 0.04	1.5 ± 0.1	2.1 ± 0.2	1.4 ± 0.2
P30	4.5	0.26 ± 0.10	2.3 ± 0.6	3.4 ± 0.8	1.5 ± 0.1

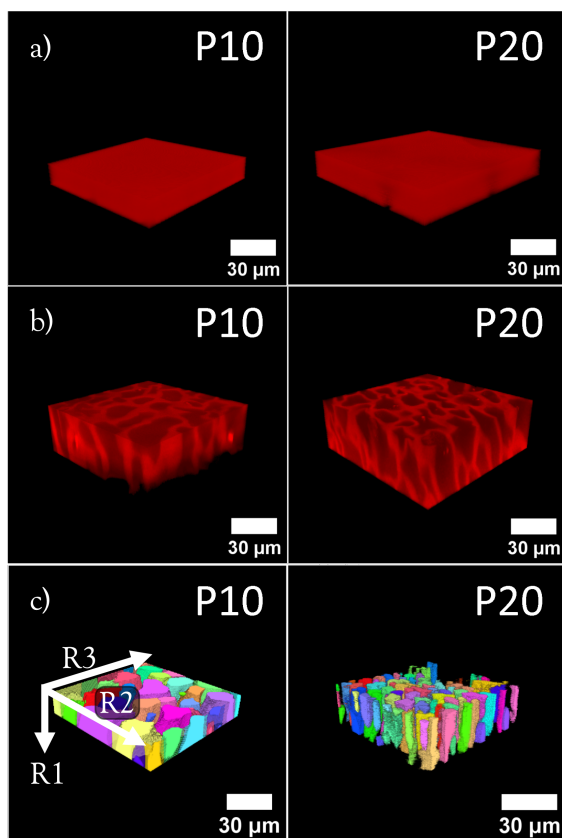


Figure 3.5: 3D images stacks of the swollen hydrogels acquired by laser scanning confocal microscopy for samples P10 and P20 before (a), and after the freeze-drying process (b). Reconstructed pores obtained through the analysis with MorphoLibJ (c).

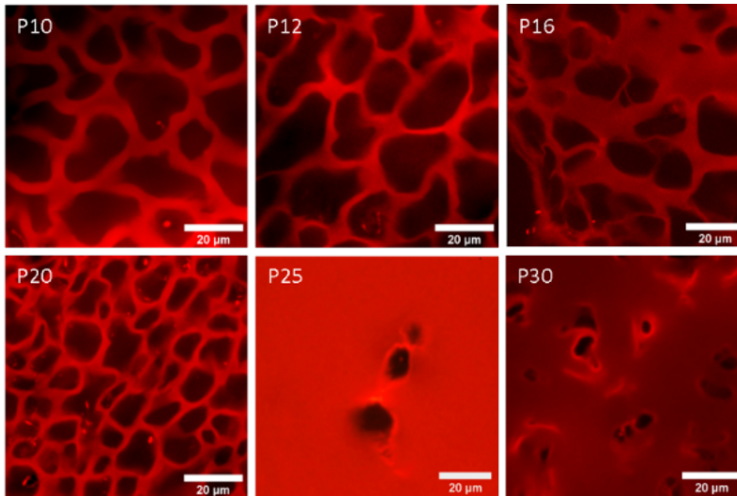


Figure 3.6: 2D confocal micrographs of the swollen porous hydrogels (where XX is the wt% of the structural component in the pre-reaction mixture).

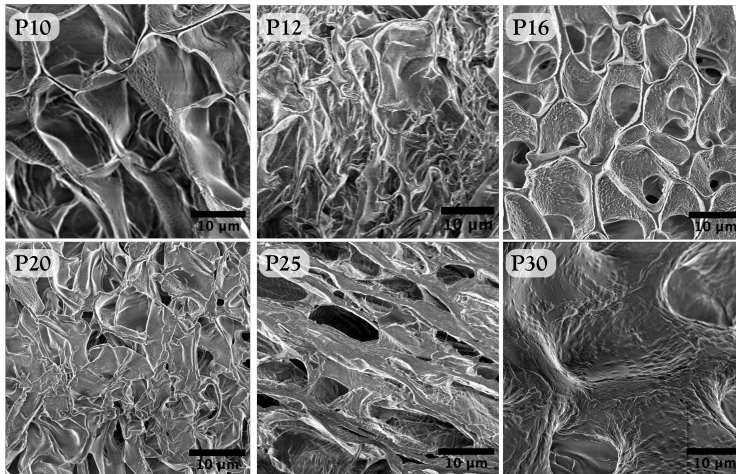


Figure 3.7: Scanning electron microscopy imaging of the freeze-dried porous hydrogels after equilibration in water.

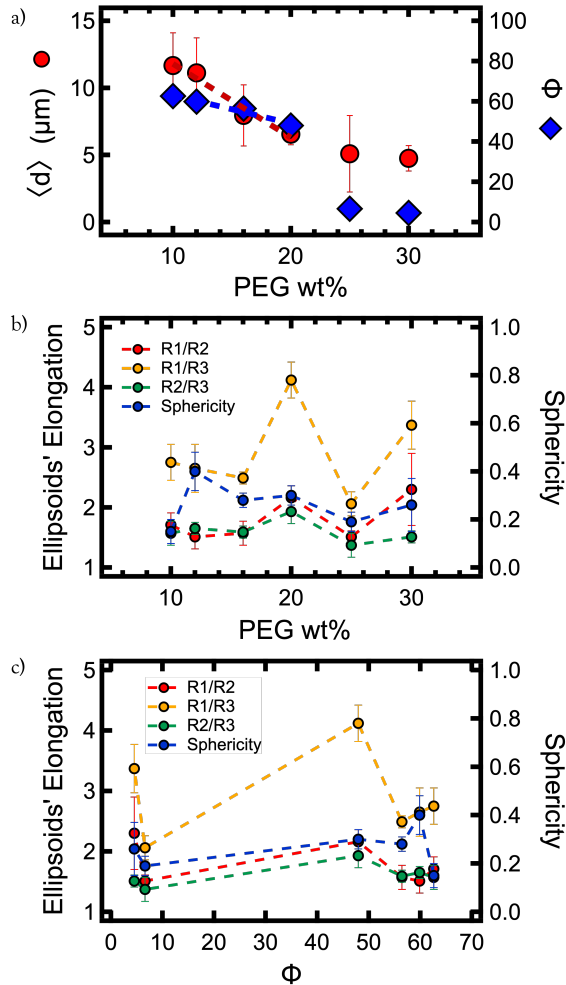


Figure 3.8: Mean pore diameter ($\langle d \rangle$) and pore volume fraction (ϕ) extrapolated from the 2D imaging (a) as a function of the macro-monomer content. The characteristic geometrical parameter extrapolated from the 3D imaging was reported to the PEG content in the pre-reaction mixture, and pore volume fraction.

3.1.4 Viscoelastic regime and flow behavior

The rheological characterization provided a quantitative description of the mechanical properties of the synthesized hydrogels. From the comparison of the storage and loss moduli as a function of the angular frequency, it is possible to understand the type of response, predominantly solid or liquid-like, of the investigated systems to the application of an oscillatory deformation. As shown in Fig. 3.9(a), all samples expose solid-like behavior throughout the entire frequency range explored: the elastic modulus is always greater than the viscous modulus with a consistent variation of the absolute values of G' and G'' as well as their relative ratio as a function of the hydrogels' composition (see Fig. 3.9); This is more clearly shown in Fig.3.10, that reports the storage and loss moduli at the angular frequency of 1 rad/sec as a function of PEG content. The G' value undergoes a significant increase with the increase of the macro-monomer content while G'' shows no significant variation with the increase of the structural component in the pre-reaction mixture. The rheological behavior was then related to the nanoscale topology by confronting the elastic modulus and the nanostructural characteristics extrapolated from SAXS profiles in Sec. 3.1.2. By comparing the Porod exponent with the viscoelastic moduli (Fig. 3.10b), a similar trend as a function of PEG content is observed. This is reasonable since elasticity, and consequently, the solid-type response tends to increase with the increase in m , corresponding to an increase in the compactness of the polymer mesh. This result is also consistent with confocal laser scanning microscopy (CLSM) measurements, where the formation of a less porous, more compact, and isotropic structure was observed with increasing PEG content. When comparing in addition the average mesh size with

the viscoelastic moduli (Fig. 3.10c), a pronounced decrease in the moduli is observed with an increase in the parameter ζ . This is also consistent since in the presence of tighter meshes, the response tends to be more elastic. The parameter a was found to be correlated with the PEG content: its value decreases with an increase in the percentage of PEG. It can be inferred that inhomogeneities tend to decrease in size with an increase in polymer content, resulting in a more compact and isotropic structure. From a rheological perspective (Fig. 3.10d), it can be seen that the dependence of moduli on a is quite moderate, especially when compared to the dependence on ζ or m . This result suggests that rheological properties are more influenced by the mesh structure rather than the presence of heterogeneities.

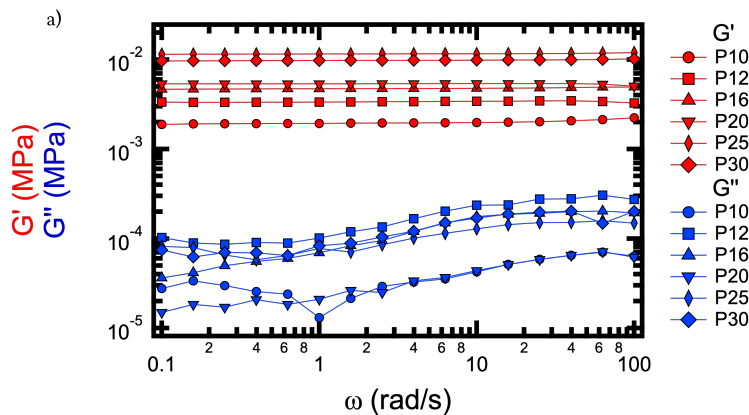


Figure 3.9: Storage (G' , red) and loss (G'' , blue) moduli profiles of the prepared PEG hydrogels as a function of the angular frequency (ω).

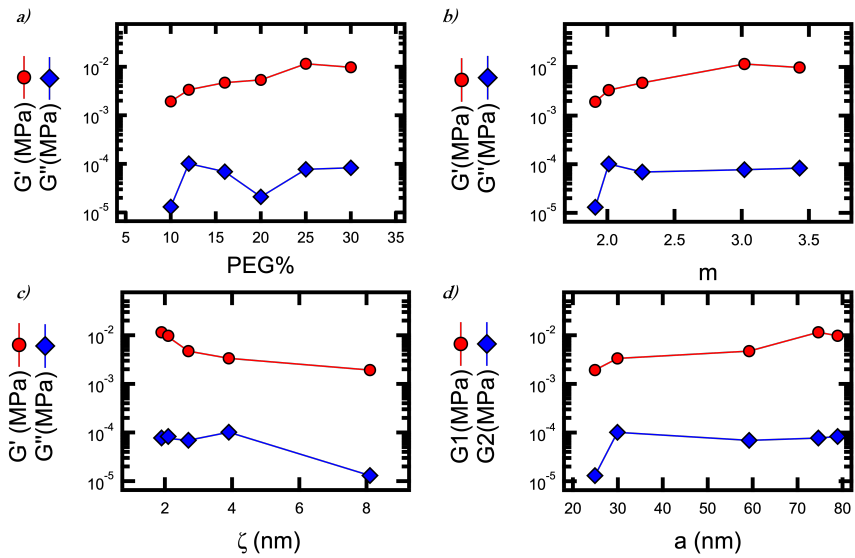


Figure 3.10: Absolute values of Storage (G' , red) and loss (G'' , blue) moduli at 1 rad/s related to the hydrogels' composition(a).

3.2 pNIPAM microgels

3.2.1 Microgels preparation

The mean particle diameter, the polydispersity, and the thermal shrinking across the volumetric phase transition (VPT) of the obtained microgels were determined by Dynamic Light Scattering (DLS) and Optical microscopy. As shown in Fig.3.11c, the thermal shrinking of the pNIPAM microgel diameter obtained from DLS can be modeled using a sigmoidal function, with a maximum diameter equal to $1.79 \pm 0.02 \mu\text{m}$ at room temperature, which decreases to $0.99 \pm 0.02 \mu\text{m}$ at high temperature. For the same temperatures, the polydispersity index obtained from the DLS analysis was equal to 0.20 and 0.06, respectively. The volumetric phase transition temperature was estimated as 32.3 ± 0.2 °C. Consistent with the DLS analysis, the data processing of the optical micrography (Fig.3.11a) at room temperature indicated a mean diameter of $1.8 \pm 0.2 \mu\text{m}$ (Fig. 3.11b) with a polydispersity index of 0.22. The thermal behavior of the synthesized microgel is in very good agreement with results in the literature [136], for similar pNIPAM microgels.

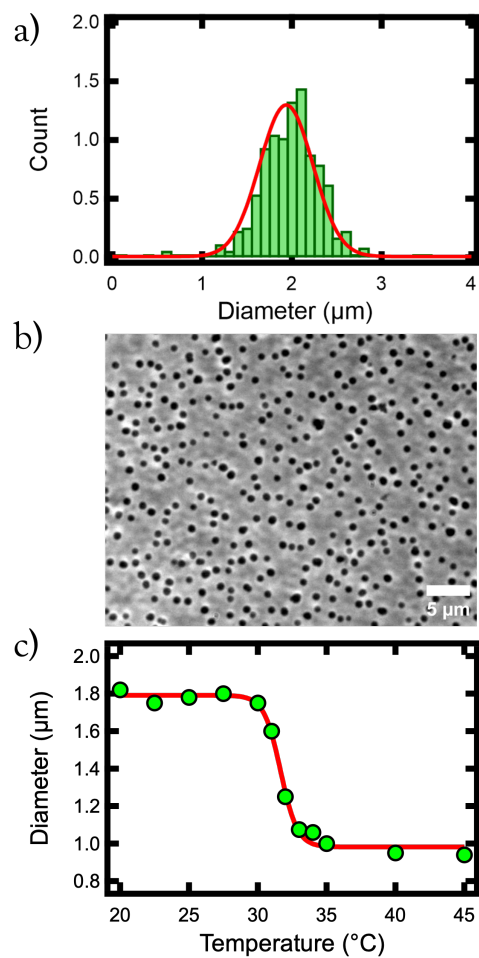


Figure 3.11: Optical micrograph of the pNIPAM microgel's water dispersion at room temperature (25 $^{\circ}\text{C}$) (a) and the extrapolated diameters distribution (b); microgels' diameter as a function of temperature as obtained by dynamic light scattering (c).

3.3 Dynamics of colloids

3.3.1 Diffusion properties of microgels

The diffusion properties of pNIPAM microgels were studied in unconfined water dispersion and in confined conditions when absorbed in the PEG hydrogels' matrices. In order to do this, a water dispersion of pNIPAM microgels of 2 wt% concentration was equilibrated with the porous hydrogels for three days under mixing at 35 °C. Representative 2D images and 3D stacks of the pNIPAM particles loaded into the polymeric networks are reported in Fig. 3.12 a-b and c-d, respectively. Despite the high temporal resolution and acquisition rate of the confocal microscope, it was not possible to study the 3D dynamics of microgels; indeed as evidenced in the 3D stacks in Fig. 3.12 c-d, the rapid movement of particles during the volume scan results in the deformation of particle images, impeding a correct tracking. The dynamics of the microgels were instead studied in the 2-3 plane (referred to Fig. 3.5 c). Based on the morphological studies done on the hydrogel's matrix, which exposed pores with a pronounced elongation perpendicularly to the 2-3 plane (axis 1), we expect that the effect of confinement should be revealed by the in-plane dynamics and not particularly influenced by the motion along the axis 1. In all the investigated systems the particle tracking method allowed the determination of the diffusion properties of the microgel. From the time and ensemble-averaged mean square displacements (MSD) the characteristic diffusive parameters were successfully extrapolated by the log-log plot as a function of the lag-time (τ), shown in Fig. 3.13. These data were obtained by averaging the 2D trajectories of all the diffusing particles over all the initial times. The time and ensemble-averaged MSD, de-

defined in 3.1 as a function of the lag-time τ , reports the x and y time-dependent coordinates of the centroid of the diffusing particle and $\langle \rangle_{i,t}$ indicates an average overall starting times and all the reconstructed trajectories in the field of view.

$$\langle \Delta r^2(\tau) \rangle = \langle [x(t + \tau) - x(t)]^2 + [y(t + \tau) - y(t)]^2 \rangle_{i,t} \quad (3.1)$$

Since micron-sized spheres are sufficiently diluted in a Newtonian fluid of viscosity η , they are expected to undergo simple Brownian motion [137–139] and their diffusion coefficient should follow the Stokes-Einstein relationship. This relationship provides a theoretical framework for understanding the relationship between particle radius R , fluid viscosity η , and diffusion coefficient of the diffusing particle:

$$D_0 = \frac{kT}{6\pi\eta R} \quad (3.2)$$

where k is the Boltzmann's constant, and T is the temperature in K . The lag-time dependence of the 2D MSDs at sufficiently long times, compared to the Brownian diffusion time, can be written as:

$$\langle \Delta r^2(\tau) \rangle = 4\langle K \rangle \tau^n \quad (3.3)$$

where $\langle K \rangle$ is an average transport coefficient and the exponent n is related to the nature of particle displacements; motion defined as normal diffusive expresses $n = 1$, while for n values smaller than 1 the motion can be defined as sub-diffusive.

The dynamics of pNIPAM microgels were investigated in unconfined conditions, by analyzing the bulk water dispersion of the polymeric particles, to the confining conditions represented by the microgels loaded in the porous matrices. As is clearly

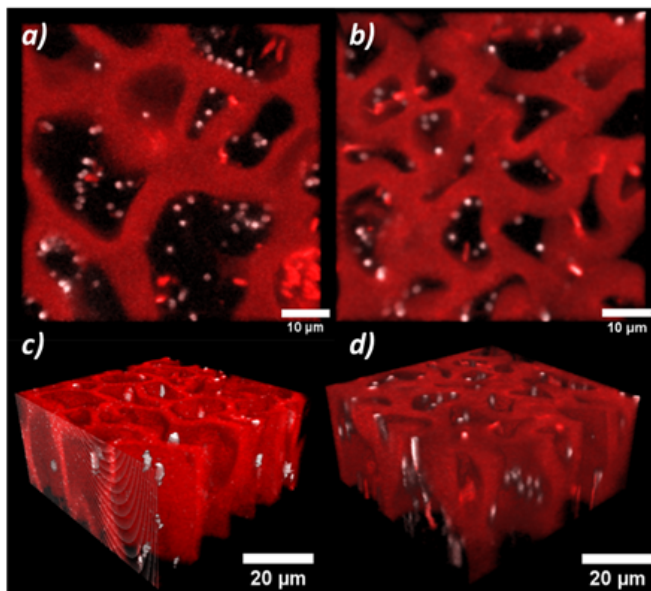


Figure 3.12: LSCM micrographies of the porous gels P10 (a) and P20 (b) loaded with pNIPAM microgels and the corresponding 3D stacks, respectively (c) and (d).

observable from Fig. 3.13, the MSDs of the microgels undergo a progressive decrease moving from the unconfined to the confined conditions imposed by the PEG hydrogels. In all investigated samples in which the microgels are confined the diffusion exponent was less than 1, thus indicating sub-diffusive dynamics for microgels confined in pores almost an order of magnitude larger than their characteristic size. Consistent with the imposed confinement, the exponent n and the effective transport coefficient are strongly affected by the hydrogel's porosity. As shown in Tab. 3.3, the highest values of n and $\langle K \rangle$, 0.60 and $0.17 \mu\text{m}^{0.60}/\text{s}$ respectively, are expressed by microgels confined in the matrix with the highest porosity and consequently the highest pore volume fraction (corresponding to gel P10). These values

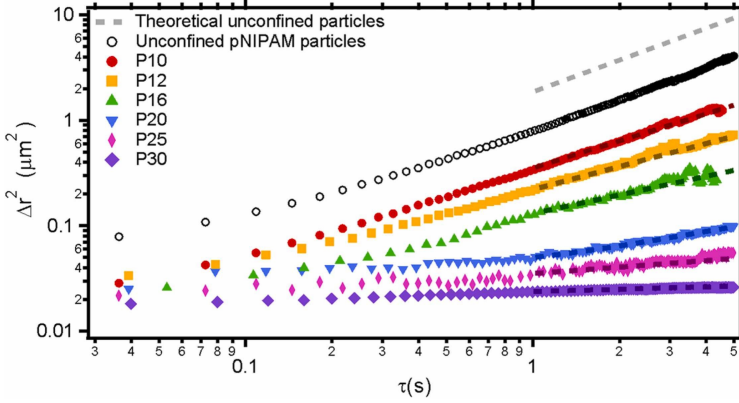


Figure 3.13: Mean Square Displacement of the diffusing pNIPAM microgels in unconfined conditions and loaded in the different porous hydrogels. Fitting curves are reported as dotted lines together with the experimental data (full and empty markers for the confined and the unconfined conditions).

gradually decrease as the mean diameter and the pore volume fraction of the confining matrix decrease, reaching values of 0.24 and 0.11 $\mu m^{0.24}/s$ for P20 samples. As a result of the greater content of PEG, pores with a smaller diameter and low degree of interconnection impose stronger confinement on the dynamics of the loaded microgels, with the result that their displacements are dramatically reduced; the pNIPAM particles are almost stuck in the small pores of the polymeric network resulting in a strong sub-diffusive behavior. The obtained effective diffusion coefficients are not entirely reliable and most likely overestimate the particle mobility. The effective diffusion coefficient, $\langle K \rangle$, and the exponent, n , normalized by the corresponding values obtained for the unconfined dispersion ($\langle K^0 \rangle$ and n^0) were related to the geometrical features describing the polymeric porous structure (see Fig. 3.14), including the normalized confinement length (ξ) and the particle area fraction (α) of the particles loaded in the

hydrogel matrices, which are defined as follows:

$$\xi = \frac{d_{particle}}{\langle d_{pore} \rangle} \quad (3.4)$$

$$\alpha = \frac{A_{particles}}{A_{pore}} = \frac{n_{particle} * A_{single\ particle}}{A_{pore}} \quad (3.5)$$

where $d_{particle}$ and d_{pore} represent the particle and pore diameter while $A_{particles}$ and A_{pore} are the total particles and pores' areas in the investigated image. The total particles' area was determined from the number of particles in the investigated area ($n_{particle}$) multiplied by the area of a single pNIPAM particle ($A_{single\ particle} = \pi R^2$).

Table 3.3: Diffusion exponent n and the effective diffusivity for the pNIPAM particles in PXX hydrogels compared to confinement hydrogels' parameters ϕ , ξ , and α (XX is the wt% of PEG in the pre-reaction mixture).

Sample	n	$\langle K \rangle$ ($\mu m^2/s$)	ϕ	ξ	α
Theoretical value	1.00	0.42	-	-	-
Non-confined system	0.96 ± 0.02	0.38 ± 0.05	-	-	-
P10	0.60 ± 0.05	0.17 ± 0.01	63	0.15	0.04
P12	0.46 ± 0.11	0.15 ± 0.03	60	0.17	0.01
P16	0.38 ± 0.08	0.13 ± 0.03	59	0.23	0.08
P20	0.24 ± 0.06	0.11 ± 0.03	48	0.29	0.11
P25	0.20 ± 0.01	0.09 ± 0.03	7	0.35	0.28
P30	0.19 ± 0.03	0.04 ± 0.02	4	0.38	0.29

Consistent with previous works on nanoparticles confined within structured and unstructured porous media [6, 141–144], the characteristic normalized parameters of the effective transport coefficient and exponent undergoes a continuous decrease as ξ and

α increase (see Fig. 3.14 a-b). Compared to similar works with nanoparticles confined in porous media of packed beds [138] or polymer films [145], with $\langle K \rangle / \langle K^0 \rangle$ values of ≈ 0.53 and 0.50 respectively, the slightly smaller value of normalized diffusivity ($\langle K \rangle / \langle K^0 \rangle \approx 0.44$ at $\xi \approx 0.15$) indicates a more pronounced confinement effect imposed by the hydrogel matrix. Based on the study of Breedveld et al. [138] who interpreted their results according to a matrix mediated steric and hydrodynamic effects in cylindrical [140, 146–149], and slit-like pores [150, 151], we compared the dependence of $\langle K \rangle / \langle K^0 \rangle$ on ξ with a cylindrical pore model that accurately predicts steric and hydrodynamic effects in this system. The results of the morphological analysis of the PEG hydrogels indicate channel-like porosity that supports the semi-quantitative agreement between the model and data reported in Fig. 3.14a [140]. In particular, in the investigated systems good agreement with the model indicates the prevalence of hydrodynamic and steric effects in the reduction of diffusion properties. Moreover, the effective diffusion coefficient and power-law exponent also exposed a consistent decrease with the particle area fraction α ; the critical value of 0.1 at which the transport coefficient starts to become constant is relatively small, indicating that hydrodynamic-like interactions or a non-uniform absorption of particles to the porous matrix play a role in addition to the geometric confinement effects. This trend of the normalized diffusivity can be described with a power-law function with an exponent of -0.38 ± 0.05 .

Consistent with the profiles reported as a function of ξ and α , the values $\langle K \rangle / \langle K^0 \rangle$ and n_{eff} / n_{eff}^0 are almost constant for pore volume fraction ϕ up to 0.4 and increase with a power-law trend with an exponent of 2.7 ± 0.2 for larger values. It is important to highlight how the relationship between the effective diffusion of

confined particles and the porosity has never been experimentally reported in heterogeneous three-dimensional systems due to the precise morphological characterization required to link the structural confinement to the diffusion properties. The pronounced confinement effect shown in our experiments, indicated by the large exponent of $\langle K \rangle / \langle K^0 \rangle$ on ϕ , exceeds the values reported in studies of gas diffusion in porous media with different geometries [152]. This result confirms again the importance of steric and hydrodynamic effects for finite-size particles and suggests the presence of particle-matrix interactions. Further information on the process controlling the confined microgel dynamics was extracted from the one-dimensional particle displacement distributions $\Delta G_s(\Delta r, \Delta t)$ calculated at different lag times for the different confining structures. As expected, the distributions became narrower for gels with a higher content of PEG in the pre-reaction mixture, i.e. with narrower porosities. As shown in Fig. 3.15, the distributions of the particle displacements are approximately Gaussian for confining gels P10, while for samples P16 and P20 deviations from Gaussian behavior are already present.

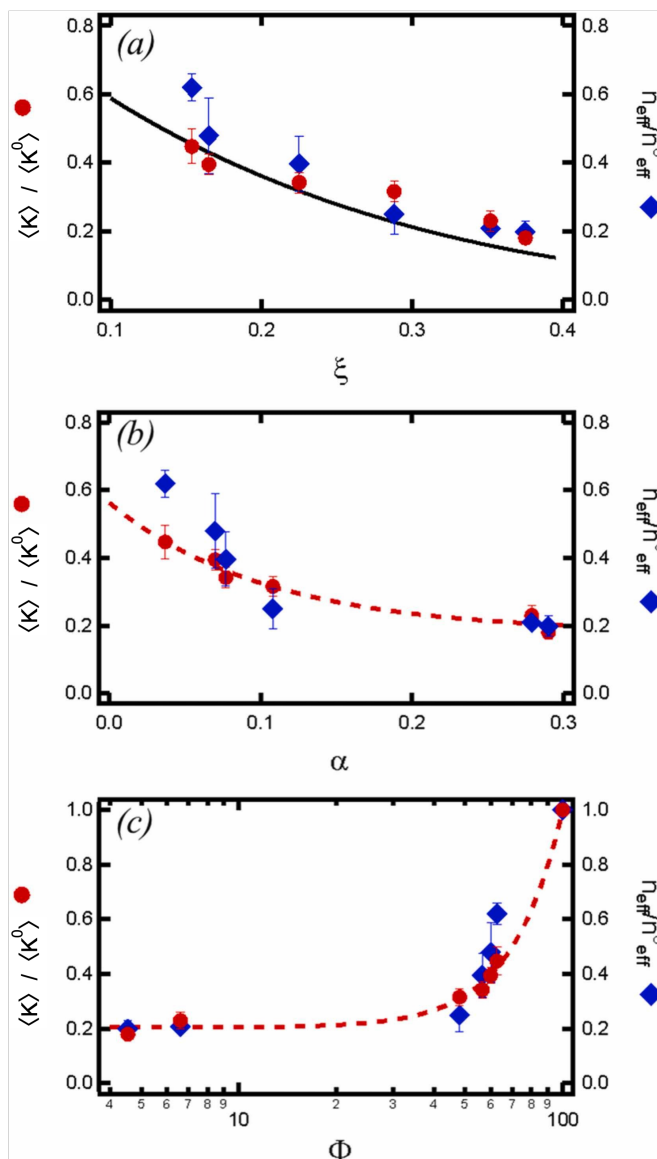


Figure 3.14: Normalized effective transport coefficient and Power-law exponent of the pNIPAM microgels as a function of the normalized confinement length (a), the particle area fraction (b), and the pore volume fraction. The continuous line in (a) represents a model calculation for diffusion in cylindrical pores that includes steric and hydrodynamic effects [140].

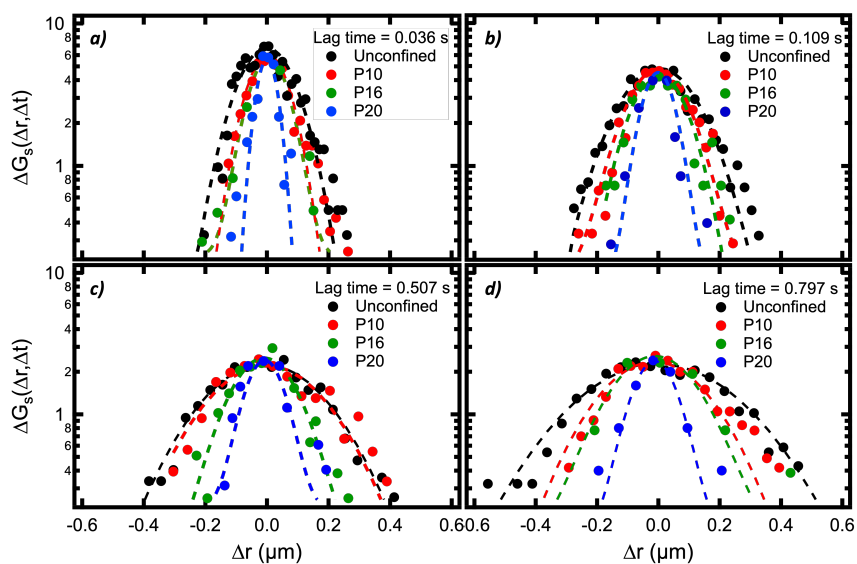


Figure 3.15: Probability distribution of pNIPAM particles' displacements ($\Delta G_s(\Delta r, \Delta t)$) at lag time of 0.036 s (a), 0.109 s (b), 0.507 s (c) and 0.797 s (d). The different color represents the different confinement media: red (P10), green (P16) and blue (P20).

3.4 Dynamics of bacteria

To advance our comprehension of the motility of active biological matter, such as bacteria, in constrained microenvironments, this study explored the motility of the application-relevant bacteria *B. subtilis* confined within the transparent porous hydrogel presented in Sec. 3.1. Different degrees of confinement and geometrical conditions were tested.

3.4.1 Bacteria characterization and hydrogel loading

To have a clear understanding of the bacterial dynamic behavior, cultures of *B. subtilis* have been prepared according to the procedures reported in Sec. 2.1.4. The obtained bacterial cells were morphologically characterized by SEM imaging in order to later link the size and shape of the investigated bacteria to the structural confinement imposed by the PEG hydrogels. For the SEM measurements, the biological tissue of the bacterial cell was fixed with glutaraldehyde for 24 hours, stained with osmium tetroxide solution for 2 hours, and subsequently dehydrated in ascending ethanol-water solutions. The resulting suspension was delicately deposited onto the sample holder and subjected to vacuum drying for one hour at room temperature to ensure complete ethanol removal. Even though the fixation procedure preserves the cell's main structure from collapsing, the intrinsic fragility of the flagella did not allow the observation of the characteristic length of these propelling structures, as shown in Fig. 3.16. Consistent with previous works [61] the applied growth conditions result in well-defined cells of length $l_{\text{bacteria}} = 2.10 \pm 0.20 \mu\text{m}$ and width $w_{\text{bacteria}} = 0.60 \pm 0.05 \mu\text{m}$, with the error estimated from image

analysis.

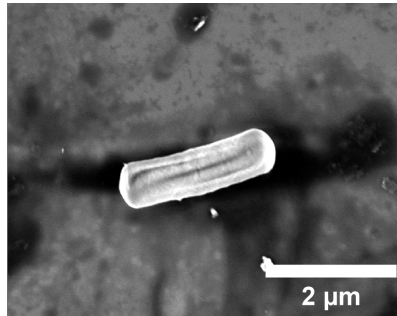


Figure 3.16: Scanning electron micrography of the stained *B. subtilis*.

The bacteria were then loaded in PEG hydrogels of different porosity, thus inducing different degrees of confinement; the fresh culture medium in the porous matrix after overnight equilibration in TSB drove bacterial adsorption within the polymer matrix. The high transparency of the confining hydrogels allowed the direct observation of bacterial motions in micro-confined environments (see Fig.3.17). Moreover, the 2D imaging shown in Fig. 3.16 highlights the versatility of this approach which allows the simultaneous cell-tracking and the characterization of the porosity of the confining matrix. While confocal microscopy offers excellent results and versatility, the high running speed of bacteria does not allow to follow them and correctly reconstruct their trajectories in 3D through particle tracking. Proof of this is the deformed image of bacteria in the 3D image-stacks shown in Fig. 3.17. For this reason, the dynamics in a 2D plane (2-3 plane, see Fig.3.16b) were investigated. Consistent with the characteristic channel-like nature of the porosity evidenced in Sec. 3.1.3, the elongation of the pores in direction 1 is sufficiently large compared to the diameter of the pores in the 2-3 plane, so that we can, in any case, assume that the major confinement effects should be revealed by the study of the in-plane dynamics.

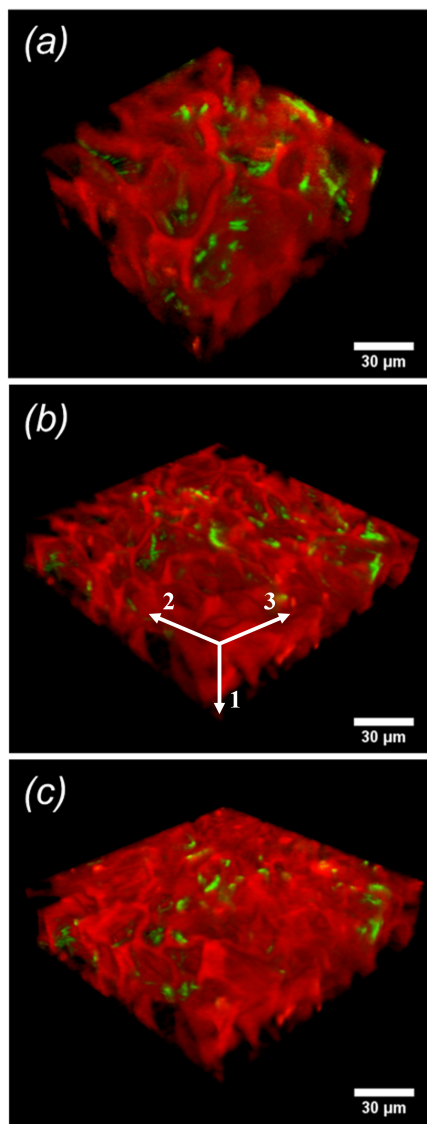


Figure 3.17: Confocal microscopy image stacks of RhB labeled porous hydrogels (red) with increasing PEG content: (a) P10, (b) P16, and (c) P20. *B. subtilis* cells adsorbed within the hydrogels are labeled in green.

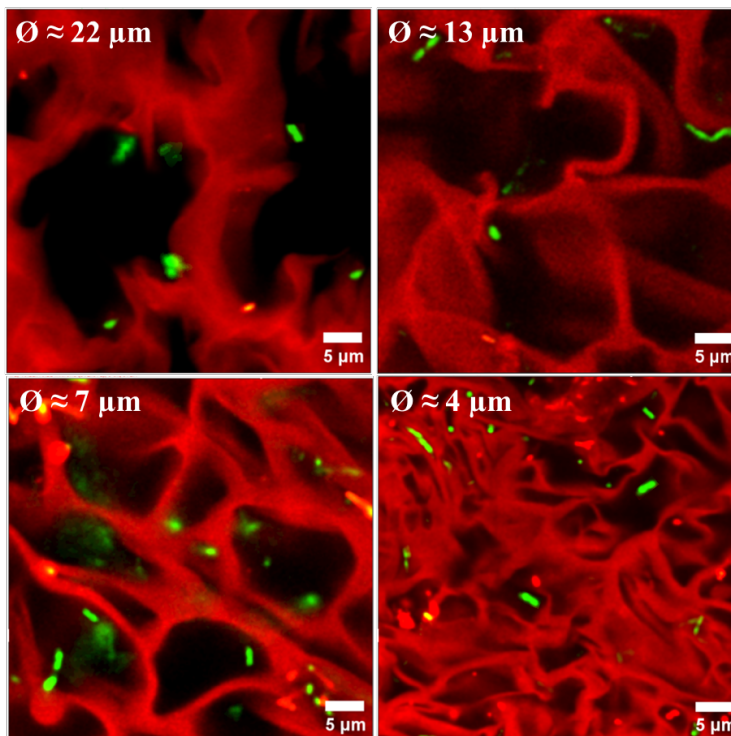


Figure 3.18: Confocal 2D micrographies of the *B. subtilis* labeled with SYTO9 (green) diffusing through the RhB-labeled porous structures (red) at different porosities with a diameter of $\approx 22 \mu\text{m}$, $\approx 13 \mu\text{m}$, $\approx 7 \mu\text{m}$, and $\approx 4 \mu\text{m}$ respectively.

3.4.2 Motility behavior

According to the expression in Eq. 3.1, the average bacterial MSDs were successfully calculated using Trackpy for all investigated systems, including the freely diffusing bacteria in bulk TSB, and reported as a function of lag-time (τ) in Fig. 3.19. To correctly relate the different degrees of confinement to the motility behavior exposed by the confined bacteria the confinement length ξ introduced in Sec. 3.3 (see Eq. 3.4) was used, here calculated using for the ratio the characteristic size of the bacterium as the cell's length and the averaged pore diameter:

$$\xi = \frac{l_{\text{bacteria}}}{\langle d \rangle} \quad (3.6)$$

A first insight into the effect of confinement on bacterial motility is clearly obtained from the progressive decrease of the MSDs with the increase of the confinement length, resulting from the decrease of the pore diameter. The time dependence of the MSDs introduced in Sec. 3.3, Eq. 3.3 is still valid and allows the extrapolation of the average transport coefficient $\langle K \rangle$ and the diffusion exponent n related to the nature of the motion.

It should be noted that the units of $\langle K \rangle$ are $\mu\text{m}^2/\text{s}^n$ and change depending on n for the different samples. On the other hand, the exponent n identifies the motion dynamic's nature as super-diffusive, as in the case of active motion at short times, normal diffusive when this value is equal to 1, and for smaller values it becomes sub-diffusive. Consistent with the expected run-and-tumble motion for bacteria swimming in bulk, the unconfined *B.subtilis* is characterized by super-diffusive motion with $n \approx 1.70$ [153, 154]. The straight runs of unconfined bacteria are also evidenced by single trajectories (Fig.3.22b, left panel). The fitting of the MSD data to Eq. 3.3 also allows the extrapola-

tion of the transport coefficient $\langle K \rangle = 26.28 \mu\text{m}^2/\text{s}^{1.70}$. In the long-time regime of the MSD profiles, for $\tau > 0.8$ s, a slope change was observed, highlighting the randomization of the motion and the transition to a diffusive regime which can be fitted by $\langle \Delta r^2(\tau) \rangle = 4\langle D \rangle \tau$; despite the few available points, the obtained value of $\langle D \rangle \approx 20.05 \mu\text{m}^2/\text{s}$ is consistent with previous finding [153].

For the correct interpretation of bacterial motility in confined conditions, anomalous diffusion models were considered, like the Continuous Time Random Walk model or the Scaled Brownian Motion model [155, 156]; according to these models, a time-dependent diffusion coefficient can be defined as $D(\tau) = nK\tau^{n-1}$, having thus the dimensions of $\mu\text{m}^2/\text{s}$ for all samples. The dynamics of samples under different degrees of confinement were compared using the time-dependent diffusion coefficient calculated at the longest time at which the MSD was determined, $D(\tau = 1\text{s})$. In mild confinement conditions, corresponding to an average pore diameter of $\approx 22 \mu\text{m}$, an approximately diffusive behavior was observed, with $n = 1.05$, while $D(\tau = 1\text{s}) = 1.98 \mu\text{m}^2/\text{s}$. Consistent with previous studies [157], these results highlight the effect of confinement even in pores about an order of magnitude greater than the characteristic size of the bacteria, resulting in a $D(\tau = 1\text{s})$ value an order of magnitude smaller than the unconfined bacteria. The effect of confinement is qualitatively appreciable observing the example trajectory shown in Fig. 3.19b; a further increase of the confinement results in the progressive localization of the bacteria within increasingly narrower porosities. The characteristic exponent n and transport coefficient $D(\tau = 1\text{s})$ for these samples reveal a sub-diffusive behavior that spans the whole time range, with MSDs that seem to approach a plateau regime for the smallest pore diameters.

The fitted values of n and $D(\tau = 1s)$, reported in Tab. 3.4, show a strong decrease of the transport coefficient with increasing confinement. For the strongest confinement $D(\tau = 1s) \approx 0.03 \mu m^2/s$; compared to the unconfined $\langle D \rangle$ this is almost three orders of magnitude smaller.

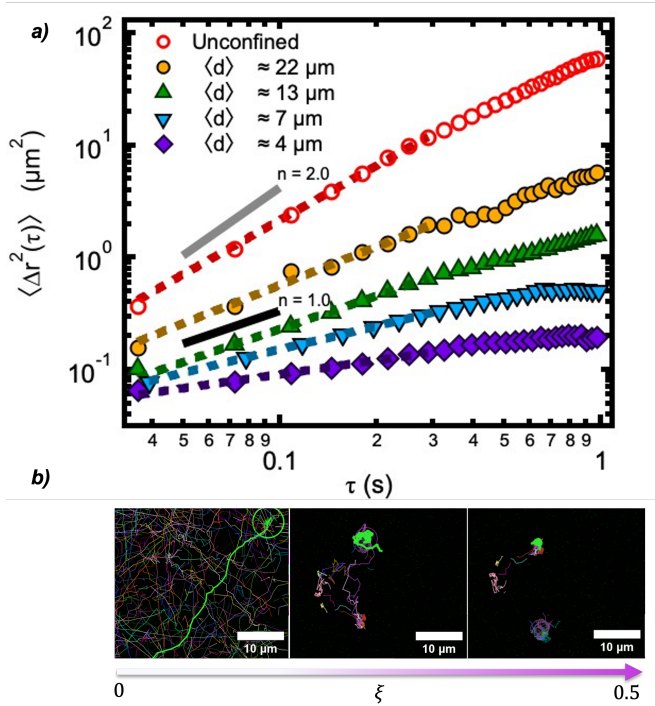


Figure 3.19: (a) Mean Squared Displacements of bacteria in unconfined conditions (empty markers) and loaded in the different porous hydrogels (full markers). Dotted lines represent fits according to Eq.3.3. (b) Exemplary single trajectories were obtained from TrackMate (highlighted in green), for three different values of the confinement length increasing from 0 to 0.5. Additional lines correspond to other bacterial trajectories.

We can conclude that the application of a structural confinement, imposed by a heterogeneous porous matrix, induces the

Table 3.4: Time-dependent diffusion coefficient $D(\tau = 1s)$ and exponent n , obtained from fits of the experimental MSD in Fig. 3.19, for bacteria in unconfined and confined conditions, corresponding to different values of the confinement length ξ .

Sample	Pore $\langle d \rangle$ (μm)	$D(\tau = 1s)$ ($\mu\text{m}^2/\text{s}$)	n	ξ
Unconfined	-	26.26	1.70	-
P10	22 ± 2	1.90	1.04	0.11
P16	13 ± 2	0.54	0.75	0.19
P20	7 ± 2	0.20	0.64	0.36
P25	4 ± 1	0.03	0.43	0.50

progressive transition from run-and-tumble active motion to average diffusive motion and a pronounced sub-diffusive motion. Although other works on *E.Coli* [83, 95] show comparable values of transport coefficients for the short-time regime, this is not found for *B.subtilis*; this discrepancy supports the different behaviour of these two bacteria, also evidenced by previous microfluidic experiments but, unlike possible cell wall deformation [158], this discrepancy can be attributed to the ability of *B. subtilis* to adapt to environmental conditions to behave as a pusher or puller [103]. In addition to this, the particle displacement distributions were calculated and, consistent with the MSD profiles, their width is reduced with increasing confinement. (see Fig. 3.20). Moreover, non-Gaussian tails, characteristics of sub-diffusive behavior and localization, were observed for all confined systems with more pronounced tails in the cases of stronger confinements; this evidence is further supported by the calculation of the non-Gaussian parameter α_2 reported in Fig. 3.21 for three different degrees of confinement; deviations from Gaussian behavior are more pronounced for the smallest confinement, even

though the corresponding MSD shows an approximately diffusive behavior in the same delay-time window. These results suggested a heterogeneous nature of bacterial trajectories under confinement. In order to elucidate these hypotheses the characteristic motility parameters were then related to the morphological parameters of the porous network. The critical effect of the confinement on the diffusion properties is clearly observed in Fig. 3.22, the progressive increase of ξ is associated to a dramatic reduction of $D(\tau = 1s)$, which can be described by an exponential decay $A \exp(-B\xi)$ with $B \approx 24.0$. Similarly, the diffusion exponent n follows an exponential decay with $B \approx 6.5$. Remarkably, even in the less confining hydrogel, with pores almost an order of magnitude greater than the bacteria length, the average dynamic behavior changes from super-diffusive to diffusive, as indicated by $n \approx 1$. Moreover, the transport coefficient $D(\tau = 1s)$ reported as a function of α and Φ can be described by a power-law dependence with an exponent of approximately 6 in both cases. On the other hand, n follows the same dependence with exponents equal to 1.6 and 2.1, on α and Φ respectively. The similar functional dependence of $D(\tau = 1s)$ and n as a function of α and Φ supports our assumption that the effects of confinement are essentially determined by the motion in the 2-3 plane. The promising results obtained from the time and ensemble-averaged parameters indicate the need of a more detailed analysis of the individual trajectories. Due to this, a single-trajectory analysis was performed on the investigated systems.

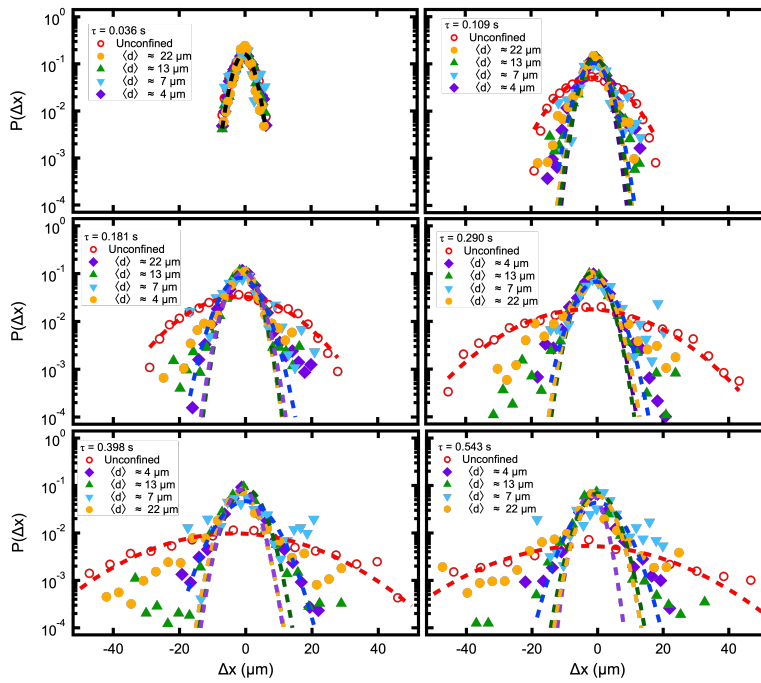


Figure 3.20: Displacement distributions of the bacteria in free diffusing dispersion and in confining networks, at different lag-times, as indicated.

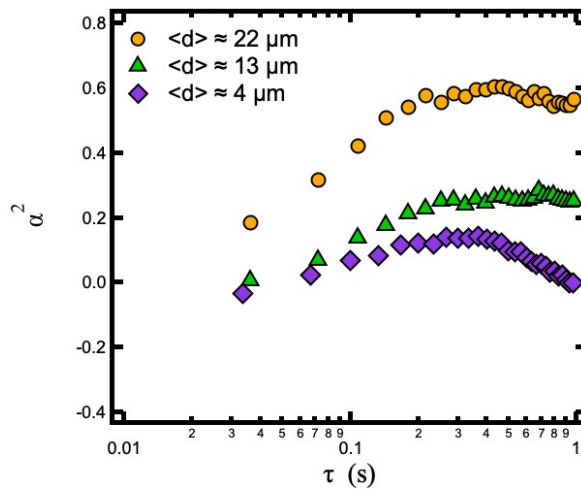


Figure 3.21: Non-gaussian parameters α_2 extracted from particle tracking analysis of bacterial motions in confinement, for three confinement conditions (as indicated) and as a function of lag-time.

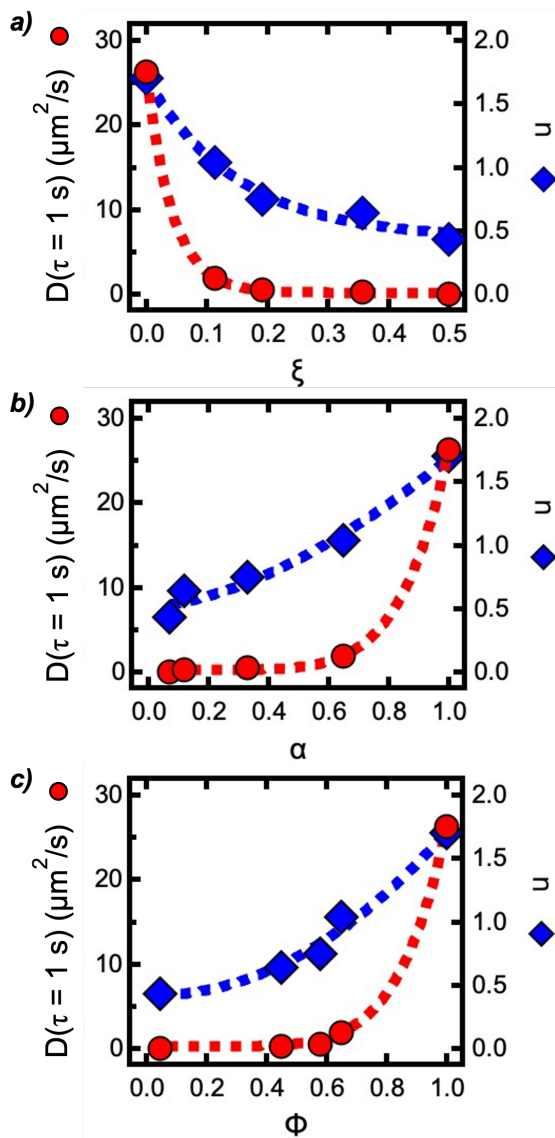


Figure 3.22: $D(\tau = 1 \text{ s})$ and power-law exponent n of the average MSD $\langle \Delta r^2(\tau) \rangle$ as a function of the confinement length (a), the pore area fraction (b), and the pore volume fraction (c).

3.4.3 Single-trajectory analysis

By analyzing the individual trajectories instantaneous velocities were extracted for each reconstructed trajectory segment; within experimental limits, the instantaneous speeds were calculated based on the ratio of the distance traveled by the bacteria in two consecutive frames divided by the temporal resolution of the recorded video. Based on this assumption, the maximal, minimal, and median instantaneous velocities were calculated for the different confining conditions (see Fig. 3.23). Consistent with the expectations, the speed distributions exhibit characteristic and progressive changes of their profiles with the increase of the imposed confinement, with a coherent shift to smaller velocities with the decrease of the pore diameter. It is interesting to note that the median values, reported in Fig. 3.23 d, follow a roughly linear decrease with increasing confinement length ξ ; furthermore, the distribution becomes narrower, suggesting an increasing control of the confining space on the bacterial velocity.

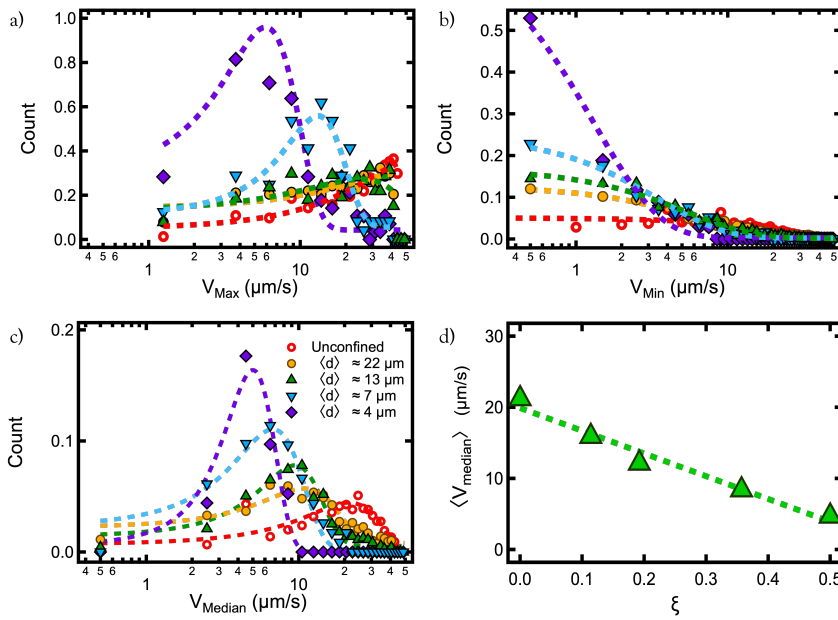


Figure 3.23: Distribution of the maximal (a), minimal (b), and median velocity (c) of all investigated trajectories for different confinement conditions, and median value of the distribution as a function of the confinement length ξ (d).

Detailing the analysis of the individual trajectories, the average reorientation rate (γ) was calculated by averaging the reorientation rate of all the reconstructed single trajectories, according to:

$$\gamma_j = \frac{\sum_i \theta_{i,i+1}}{N \Delta t_j} \quad (3.7)$$

where $\theta_{i,i+1}$ represents the reorientation angle between two consecutive steps, i and $i + 1$, in a trajectory j , N is the total number of reorientation events and Δt_j is the total duration of the trajectory. In addition, the mean straight-line speed (V_{SL}^j) was also calculated from the single trajectories; this speed can be defined as the speed that the bacteria would present when moving at constant speed along a straight line from the initial to the final spot of a trajectory. It can be defined as the net distance traveled d_{j0} in the time Δt_j for the trajectory j :

$$V_{\text{SL}}^j = \frac{d_{j0}}{\Delta t_j} \quad (3.8)$$

where the value $\langle V_{\text{SL}} \rangle$ is the average over all trajectories. In order to have a complete overview of the linearity/tortuosity of bacterial dynamics in the investigated systems, the confinement ratio (CR), or persistence, was calculated and averaged over all trajectories; this parameter indicates the 'efficiency' of the trajectory in getting far away from its starting point and can be defined as the net-displacement divided by the total-distance traveled:

$$CR = \frac{d_{j0}}{\sum_i d_{i,i+1}} \quad (3.9)$$

where $\sum_i d_{i,i+1}$ is the total distance traveled along a trajectory. The relation between these three parameters and the confinement length ξ is shown in Fig. 3.24. Consistent with the run-and-tumble motility mode, the free-diffusing bacteria exposed the

greatest mean straight-line velocity and the smallest average reorientation rate (see Fig. 3.24a); as a result of the imposed structural confinement, a decrease of average reorientation rate was observed with the increase of the confinement length, reaching an almost constant value $\gamma \approx 40$ rad/s for $\xi > 0.2$. This possibly suggests a physical limit of this specific bacterium, *B.subtilis*. Note that, compared to $\langle V_r \rangle$, $\langle V_{SL} \rangle$ decreases more rapidly as a function of confinement: this can be explained by the suppression of straight trajectories in favor of random motion typical of diffusion or sub-diffusion. The induced randomization of bacterial motion was also confirmed by the confinement ratio with values that go from ≈ 1 in the free-diffusing bacteria to ≈ 0.5 under the strongest confinement (see Fig. 3.24b). These trends indicate a significant change in the motility behavior of the bacteria under confinement; in these conditions, less straight trajectories, typical of the run-and-tumble motion, are observed with the consecutive faster reorientation needed to escape the confinement imposed by the hydrogel.

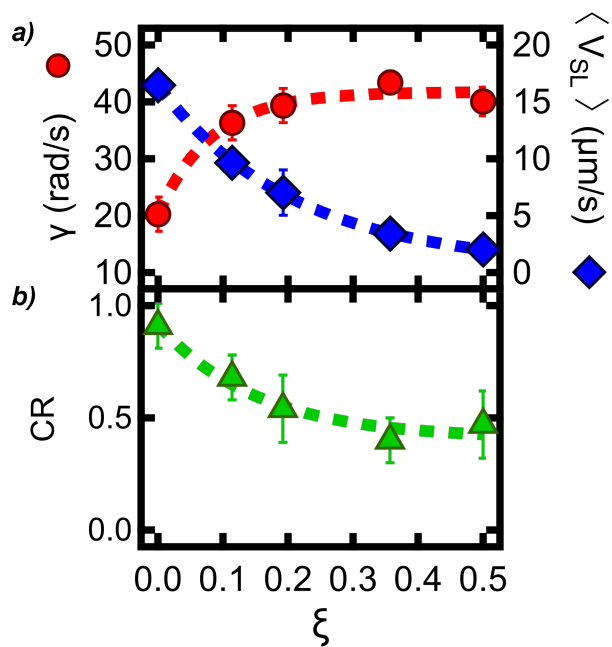


Figure 3.24: Average reorientation rate γ , mean straight line velocity $\langle V_{SL} \rangle$ (a) and mean confinement ratio CR (b) as a function of the confinement length.

3.4.4 Trajectories classifying

In order to study the possible transient events that characterize motility in confined conditions, the trajectories studied have been divided into segments and these were analyzed according to three models [159], which describe the MSD for sub-diffusive(Eq. 3.10), normal diffusive(Eq. 3.11), and active motion(Eq. 3.12):

$$\langle r^2_{(m)}(t) \rangle = 4K(m\Delta t)^\alpha \quad (3.10)$$

$$\langle r^2_{(m)}(t) \rangle = 4Km\Delta t \quad (3.11)$$

$$\langle r^2_{(m)}(t) \rangle = 4Km\Delta t + (\nu m\Delta t)^2 \quad (3.12)$$

where in all equations the parameter m represents the number of segments that can be classified according to the corresponding motion type. According to Saxton et al. [160], the models can describe diffusion, sub-diffusion, with $\alpha < 1$, and active motion, with the velocity parameter ν . Distinct from previous works, conducted mainly on E.coli, where only a qualitative distinction between hopping and trapping events was discussed, a quantitative classification of the trajectories split into segments representing the different transient events is presented. The results of this classification, reported in Fig. 3.25, highlight the effect of the imposed confinement on the distribution of the different hopping and trapping events; in the free-diffusing bacteria case the majority of the trajectory segments are classified as active motion, with a relatively low fraction of diffusive segments, that could explain the $n \approx 1.7$ exponent of the MSD, instead of the expected value of 2 for purely active motion. Consistent with the expectations, no sub-diffusive trajectory segments are observed in the unconfined case; a roughly linear increase of the sub-diffusive

segments is observed for increasing confinement length ξ , with a consequently sharp decrease of the percentage of active trajectory segments. These reach a plateau equal to $\approx 20\%$ for $\xi > 0.2$. On the other hand, the percentage of diffusive segments seems to have a maximum at intermediate confinement for $\xi \approx 0.15$, before approaching a plateau similar to that observed for active segments. These results confirmed the coexistence of different types of motion, with transient events of hopping associated with diffusing and active segments and trapping associated with sub-diffusive segments. Their respective frequencies are related to the imposed confinement length; those events characterize the average dynamics represented by the MSD. In the investigated conditions the bacteria undergo these three different modes by exploring the porous network, approaching the confining walls, and reorienting itself to 'escape' from the imposed confinement. Even though the sub-diffusive populations are comparable in the range of confinement lengths $0.1 \leq \xi \leq 0.2$, in the strongest confinement conditions this population became dominant with the consequent average sub-diffusive behavior. An additional remark is that the growth of the reorientation rate coincides with the increase in the population of diffusive segments, while its plateau with the drop in the same population. This suggests that the most significant bacterial reorientation allowing to escape confinement occurs along the diffusive segments of the trajectories.

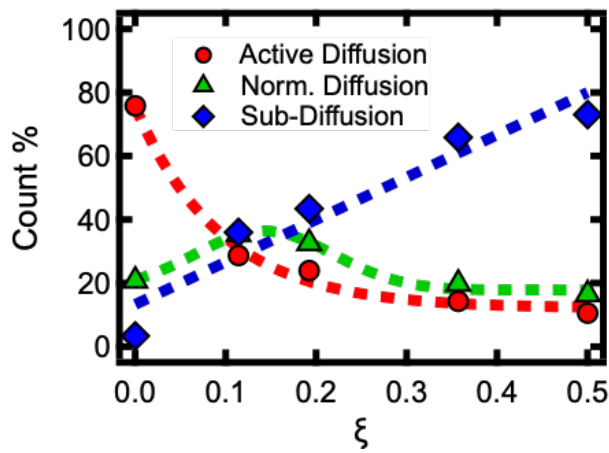


Figure 3.25: Normalized populations of segments classified as active, diffusive, or sub-diffusive, as a function of the confining length (ξ).

3.4.5 Transport models

In multi-flagellated micro-swimmers presenting run-and-tumble motility, the dynamic behavior is characterized by the alternation of straight-swimming motion and directional reorientations resulting from the collective bundling and unbundling of the flagellar apparatus, respectively.

At sufficiently long times, however, the reorientation in random directions leads to an effective diffusive motion. A model of this long-time diffusion for bacteria with run-and-tumble motility can be provided in terms of a random walk, with runs represented by links between two events of reorientation at the vertices; assuming the tumbling process is a homogeneous Poisson process the diffusive behavior at long times can be written as:

$$D = \frac{\langle L_r^2 \rangle}{4\langle \tau \rangle(1 - \theta)} \left[1 + \left(2 \frac{\langle L_r \rangle^2}{\langle L_r^2 \rangle} - 1 \right) \theta \right] \quad (3.13)$$

where $\langle L_r \rangle$ and $\langle L_r^2 \rangle$, are the mean run length and mean square run length, respectively, $\langle \tau \rangle$ is the mean run-time, and θ is the mean projection of the tumble. In the free-diffusing regime, the bacterial motility can be described by the run-and-tumble model where the randomization of the trajectories at a sufficiently long time leads to the diffusion coefficient given by [64, 90–92, 161, 162]:

$$D_{RT} \approx \frac{\langle V_r \rangle \langle L_r \rangle}{3} \quad (3.14)$$

with $\langle V_r \rangle$ the mean speed of ballistic run; in this assumption, the characteristic mean run length of the free-diffusing bacteria is given by:

$$\langle L_r \rangle = \langle V_r \rangle \tau \quad (3.15)$$

This approach can be extended to the diffusion in a homogeneous porous system characterized by an average pore size $\langle d \rangle$. In such systems, the encounter of the swimming bacteria with the boundary wall interrupts the straight-line motion and determines a reorientation event [94]; according to this, the mean run length resulting from the imposed confinement L'_r is expressed as:

$$\langle L'_r \rangle = \langle V_r \rangle \tau (1 - e^{-\langle d \rangle / \langle V_r \rangle \tau}) \quad (3.16)$$

and

$$\langle L_r'^2 \rangle = 2 (\langle V_r \rangle \tau)^2 \left[1 - \left(1 + \frac{\langle d \rangle}{\langle V_r \rangle \tau} \right) e^{-\langle d \rangle / \langle V_r \rangle \tau} \right] \quad (3.17)$$

In the regime of large pore size $\langle d \rangle \gg \langle V_r \rangle \tau$, this description of the mean run length leads to the running length of free-diffusing bacteria in bulk liquids. This definition of the diffusion coefficient provides values in perfect agreement with that extrapolated from the experimental MSDs of the unconfined *B. subtilis* (see Fig. 3.26a). In the confined case, where the pore size became comparable to the characteristic running length of the free-diffusing bacteria ($\langle d \rangle \approx \langle V_r \rangle \tau$), it is usually assumed that the run-and-tumble motility mode is preserved [93,94]; in this assumption, the characteristic mean running speed is still the same of the unconfined case ($\langle V_r \rangle$), but applied for shorter run lengths, $L'_r > L_r$, as a results of the imposed confinement with running lengths corresponding to the mean pore diameter, $L'_r \approx \langle d \rangle$. However, evidence of the qualitative change in motility mode has been highlighted by previous work on *E. coli* in soft confinement conditions [83, 95]; the results of the single trajectory analysis and classification here reported confirmed this evidence and elucidate at the single trajectory level the critical motility change from the characteristic active motion of run-and-tumble to the diffusive

and sub-diffusive motion induced by confinement. In order to rationalize this evidence in a well-representative model of motility in confinement conditions, Bhattacharjee et al. [83,95] described the bacterial dynamic as a series of intermittent hopping and trapping events along the performed trajectories; in this configuration, the running bacteria that encounters a boundary wall interrupts its hop and remains trapped, until a favorable reorientation allows a new hopping. The proposed approach is consistent with the single trajectory analysis reported in this work and supported by the decomposition of the trajectory in active, diffusive, and sub-diffusive segments. In the described system the sub-diffusive segments can be interpreted as trapping periods, while diffusive and active segments as hopping events; different from the proposed approach, the analysis of the reorientation rate coupled with segment classification suggests that in our case also diffusive displacements contribute to the escape from local trapping. The expression of the effective diffusion coefficient in this new approach of hop-and-trap motility mode can be given by the hopping lengths L_h , since $L_h \gg L_t$, while the total diffusion time, given by the sum of hopping and trapping periods, can be assumed equal to this last contribution since $\tau_t \gg \tau_h$, with h and t referred to hop and trap events, respectively. This description of the effective diffusion coefficient leads to the following formulation of this parameter:

$$D_{HT} \approx \frac{\langle L_h \rangle^2}{3\langle \tau_t \rangle} \quad (3.18)$$

Also the temporal evolution of the instantaneous speeds, reported in Fig. 3.26b, shows the characteristic intermittent switching between hops, corresponding to the peaks, and trapping events, represented by the flat bottom temporal ranges. Unlike previous

studies on *E. coli* [95], the maximal values reached by the confined bacteria are significantly smaller than the bulk run velocity; this evidence supports that the observed hops are the possible combination of active runs and diffusion for the case of *B. subtilis*. Moreover, the instantaneous velocity profiles provide the hopping and trapping times defined as the periods at which the bacteria has a velocity larger or smaller than a threshold value, respectively. Different from other works where this threshold value was empirically assigned as $1/2V_r$ of the unconfined case [83, 95], in the present work it is defined as the median instantaneous velocity extrapolated from the trajectories in the different confinement conditions. As shown in Fig. 3.26b (red dashed line), the run velocity of the free-diffusing bacteria is not describing the motion of the bacteria in the confined cases, for which the instantaneous running velocities are significantly affected by the imposed confinement (dashed lines). Based on the defined threshold value the average hopping length was calculated as $\langle \nu_{\text{median}} \rangle \Delta t$, with Δt the time between two steps in a trajectory. As shown in Fig. 3.27a, the distributions of hopping lengths L_h were determined for three values of confinement, corresponding to $\langle d \rangle = 22, 13,$ and $4 \mu\text{m}$ and the median values extracted from these distributions are reported in Tab. 3.5. Consistent with the expectation the hopping lengths are strongly affected by the imposed confinement and $\langle L_h \rangle$ values are smaller than the effective pore size of the confining matrices, indicating the importance of cell-matrix interactions. Unfortunately, the high noise affecting the experiments in the matrix of $\langle d \rangle \approx 7 \mu\text{m}$ did not allow the determination of reliable median values of L_h , therefore this value was not reported. The possible bacteria-bacteria or bacteria-matrix interactions are suggested by the obtained values of $\langle L_h \rangle$, which are always smaller than the average pore size; this interaction could

be mediated by sensory organs such as the pili randomly distributed on the cell membrane. As expected, $\langle L_h \rangle$ is significantly affected by the imposed confinement, presenting an exponential decay as a function of the confinement length (Fig. 3.27b). The effective diffusion coefficients predicted through Eq. 3.14, D_{HT} , are in excellent agreement with the experimentally determined $D(t = 1s)$ (see Fig. 3.26a). As highlighted from Tab. 3.6, the arbitrarily adopted threshold value of $1/2\langle V_r \rangle$ results in a strong underestimation of the time-dependent diffusion coefficient; the introduction of a threshold value calibrated on the observed median speeds allows the precise determination of this parameter even if the system does not display a diffusive motion regime. Interestingly, the median velocity resulting from the imposed confinement ($\langle V_r \rangle_{conf}$) can be related to the velocity of the free-diffusing bacteria ($\langle V_r \rangle_{unc}$) through the confinement length ξ , as expressed by the following equation:

$$\langle V_r \rangle_{conf} = (1 - \xi)^2 \langle V_r \rangle_{unc} \quad (3.19)$$

The results of this relation are graphically reported in the insight in Fig. 3.26, where the experimentally determined median running speeds, normalized by the median value of the free-diffusing bacteria (yellow marker), and the predicted values (dotted line) are reported as a function of the confinement length ξ ; the predicted values find good agreement with the experimental data suggesting that the relation parameter $(1 - \xi)^2$ is the result of the ratio between the effective area of a pore with a diameter $\langle d \rangle$ occupied by a rapidly reorienting bacteria of length $l_{bacteria}$, and the area of the corresponding empty pore:

$$(1 - \xi)^2 = \frac{A_{free}}{A_{pore}} = \frac{\pi(\langle d \rangle - l_{bacteria})^2/4}{\pi\langle d \rangle^2/4} \quad (3.20)$$

Table 3.5: Characteristics 2D run lengths in confined and unconfined conditions related to the structural parameters of the porous matrices.

Sample	ξ	α	Φ	$\langle L_h \rangle$ (μm)
P10	0.11	0.65	0.65	1.29
P16	0.19	0.33	0.58	0.79
P20	0.36	0.12	0.45	-
P25	0.50	0.07	0.045	0.22

Table 3.6: Diffusion coefficients D , experimentally and theoretically predicted from the hop-and-trap model (D_{HT}). The D_{HT} values were calculated for both the cut-off velocities $\langle Vr \rangle$ and $1/2\langle Vr \rangle_{\text{free}}$.

ξ	$D(\tau = 1\text{s})$ ($\mu\text{m}^2/\text{s}$)	D_{HT} ($\mu\text{m}^2/\text{s}$)	$D_{\text{HT}(1/2 V_{\text{free}})}$ ($\mu\text{m}^2/\text{s}$)
-	44.64	-	-
0.11	1.98	1.79	1.30
0.19	0.40	0.53	0.32
0.36	0.13	-	0.05
0.50	0.03	0.02	0.005

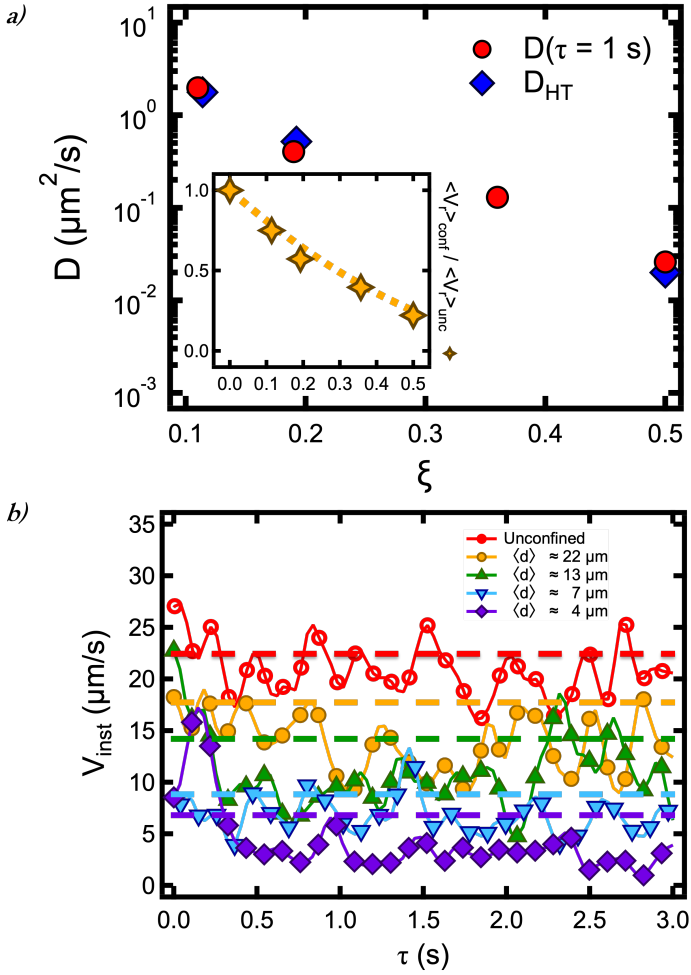


Figure 3.26: (a) Motility coefficient experimentally determined from the time and ensemble-averaged MSDs ($D(\tau = 1 \text{ s})$), and predicted from the hopping and trapping model D_{HT} (as indicated). Median running velocities normalized by the velocity in unconfined conditions as a function of the confinement length. (b) Time evolution of the instantaneous velocities for exemplary single trajectories of bacteria swimming in unconfined conditions (empty markers), and through the different confining matrices (full markers), as indicated. For clarity, the number of markers was reduced, reporting one every 3 experimental points. Corresponding median speeds extracted from the velocity distributions of Fig.3.23d are indicated by dashed lines. Dashed line corresponding to the model of Eq.3.7

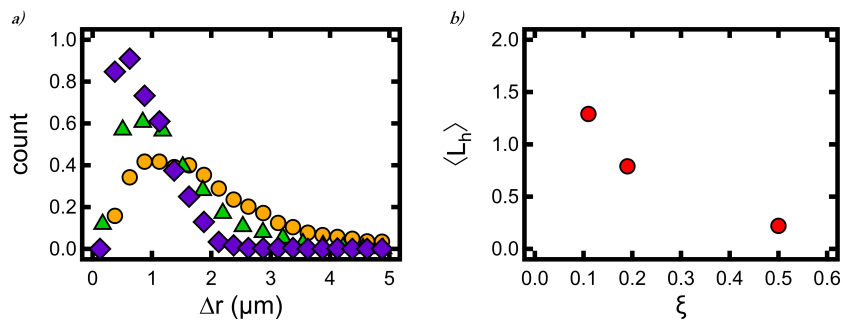


Figure 3.27: (a) Distribution of the hopping length of the investigated trajectories for different confinement conditions (as indicated). (b) Average hopping lengths $\langle L_h \rangle$ as a function of confinement length (ξ)

As shown in Fig. 3.28, the normalized probability densities of trapping times $P(\tau)$ highlight the increase of these times with the decrease of pore diameter, leading to the localization of the motion over increasingly longer trapping times. Interestingly, the probability densities were well-fitted by a compressed exponential function described by the decay time τ_d and the compressing exponent β as a function of the trapping period τ_t :

$$P(\tau_t) \approx A \exp \left[- (\tau_t/\tau_d)^\beta \right] \quad (3.21)$$

Theoretical models or previous experimental evidence that predict this kind of distribution could not be found. In the regime of long times, the trapping period distribution was usually predicted by conventional models of anomalous diffusion with the power-law dependence $P(\tau_t) \approx \tau_t^{-1-n}$ with n as the sub-diffusive exponent of the MSD [69]; in our case such dependency leads to values of the characteristic compression parameters, -3.8 in the large pore limit, and -2.6 for the smaller pore case, that is not consistent with the values of diffusion exponent n obtained from the fitting of the experimental MSD. On the other hand, the increase of confinement is reflected by the decay of τ_t as a function of both ξ and α , see Fig. 3.28b-c respectively. Consistent with the imposed confinement, the trapping duration was found to increase with the increase of the confinement length and decrease with the increase of the pore area fraction, while the progressively stronger compression of the exponential behavior was reflected by the increase of the stretching exponent β with the imposed confinement. Compressed exponential distributions have been associated in glassy systems with avalanche-like dynamics below the glass transition temperature [163]. The connection between the bacterial dynamics in confinement and avalanche-like phenomena should be investigated in the future.

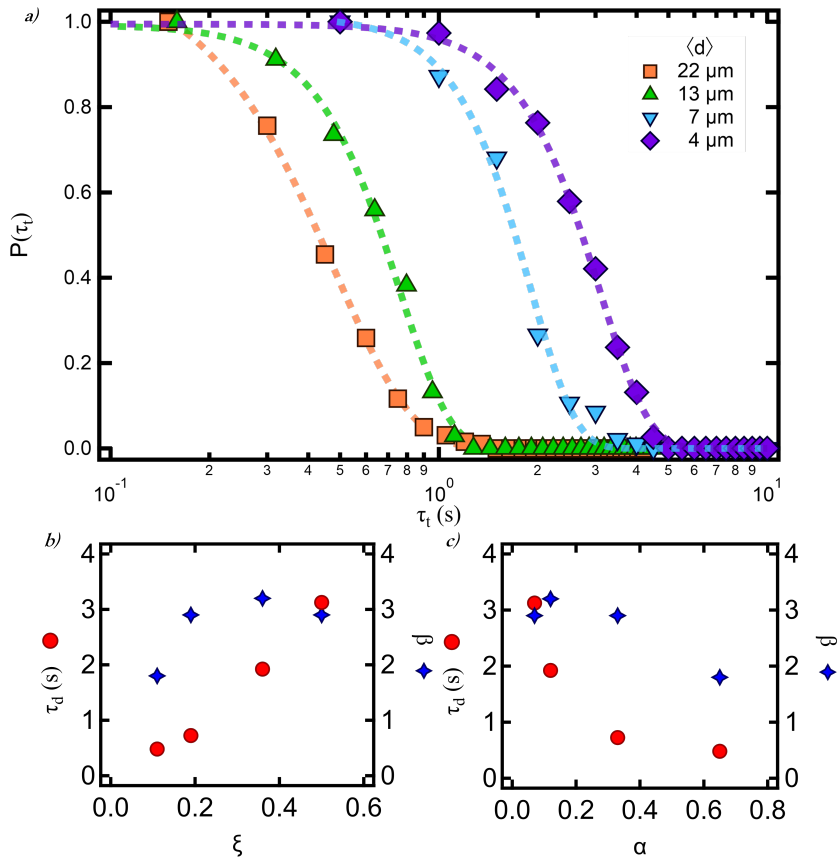


Figure 3.28: (a) Probability density distributions $P(\tau_t)$ (symbols) of the trapping times τ_t in the different confining matrices, as indicated. Dashed lines represent fits to a stretched exponential function, Eq.3.21. (b-c) Characteristic parameters τ_d and β resulting from the fits in (a), as a function of the confinement length (b), and the pore area fraction (c).

Chapter 4

Conclusion

This thesis work describes a novel approach to study the dynamic behavior of passive and active systems, such as colloids, and self-propelling bacteria, in porous confinement. The approach combines the use of highly transparent polymeric networks as confining media with optical microscopy and particle tracking. Fluorescently labeled porous PEG-based hydrogels with a high degree of transparency were developed in this work; The internal porous structure of the hydrogels, created through freeze-drying, was tailored by varying the macro-monomer content in the pre-reaction mixture. A comprehensive characterization of the hydrogels' internal porous structure was conducted using various experimental techniques, such as SAXS, SEM, rheological analysis, and confocal microscopy. Specifically, detailed insights into the 3D image stacks obtained from confocal microscopy provided volumetric information on pore geometry in relation to PEG content, unveiling a highly asymmetric channel-like porosity. As the PEG content increases, there is a gradual reduction in the channels' cross-sectional area. This reduction exhibited a linear trend

up to a critical threshold of 20 wt% PEG content, beyond which both porosity and pore interconnection experienced a significant decrease. The rheology measurements revealed that the synthesized hydrogels exhibit a solid-like response with an increase in the elastic modulus corresponding to the increase in the PEG content in the pre-reaction mixture, i.e. with decreasing porosity. The rheology results could be also linked to SAXS measurements, finding that the increase in elasticity with PEG content is associated with an increase in the Porod exponent m . Since an increase in m is connected with a progressive collapse of the polymer conformation, the results are consistent with the formation of a more compact and less porous network when increasing PEG content. As a further confirmation, elasticity is found to be maximal for the minimum value of ζ , so for a tighter mesh. Finally, the comparison with the characteristic size of heterogeneity in the network structure suggests that the latter, unlike ζ , does not significantly influence the viscoelastic moduli, indicating that rheological properties are more influenced by the mesh structure rather than the inhomogeneities.

Particle tracking analysis of microgel displacements within hydrogel matrices revealed the impact of confinement on microgel transport. The dynamics of microgels transitioned from approximately diffusive behavior within wide channels to subdiffusive behavior in narrow channels, in agreement with observations for nanoparticles confined in inverse opal structures. In the 3D morphological analysis of porosity, which identified elongated, channel-like pores, we compared the dependence of the effective diffusion coefficient on confinement length with models accounting for particle diffusion in cylindrical pores, incorporating hydrodynamic and steric effects.

The strong agreement between our findings and model pre-

dictions underscores the significance of these effects on confined microgel dynamics. Furthermore, we observed a substantial dependence of the effective diffusion coefficient on pore volume fraction, which could be characterized by a power-law relationship with an exponent considerably larger than expected for purely geometrical confinement effects in porous random media. This evidence suggests the presence of additional influences, including hydrodynamic and steric interactions, as well as potential effects stemming from microgel-hydrogel matrix interactions.

Furthermore, the developed hydrogels were applied to the investigation of the effects of confinement on the motility of self-propelling micro-swimmers, *B. subtilis*; The precise characterization of the porous matrix, coupled with single-trajectory analysis through particle tracking, enabled a quantitative understanding of bacterial dynamics in relation to the degree of confinement. The well-known run-and-tumble motility of *B. subtilis*, displaying super-diffusive mean square displacement (MSD) at short times and diffusive behavior at long times, was dramatically influenced by confinement.

Upon reducing hydrogel pore size, MSDs shifted from diffusive to sub-diffusive at short times. Analysis of single trajectories revealed a qualitative shift in individual bacterial dynamics within confinement. Trajectories exhibited a combination of active, diffusive, and subdiffusive segments. Active segments were significantly suppressed in confinement, replaced by diffusive and subdiffusive segments under intermediate confinements, while subdiffusive segments prevailed in stronger confinements. This transition correlated with a marked reduction in median velocity and a substantial increase in reorientation rate.

The alternating dynamics were described in terms of a hopping and trapping motion, where entrapment resulted from the

confining porosity. Unlike *E. coli*, which exhibited active jumps for release from local confinement, *B. subtilis* hopping events involved both active and diffusive motions. Hopping events were redefined based on displacements with an instantaneous velocity exceeding the median velocity estimated from trajectories. This redefinition aligned well with transport coefficients estimated from long-time MSDs, following predictions from a recent model of hopping and trapping motion. As a last effort, an empirical relation was introduced, quantitatively linking the median velocity under confined and unconfined conditions through the characteristic length and effective pore area associated with the imposed confinement.

The results of this thesis highlight the crucial importance of integrating the analysis of the single trajectory with a detailed morphological characterization of the confining matrix to better understand the diffusion behavior within heterogeneous environments. The method here developed is an excellent starting point for the exploration of diffusion properties in relation to the confining environment; It represents a valid reference to study the colloidal diffusion and the processes of migration and bacterial proliferation in confining natural habitats, such as soil or tissues. The present study reports the transport behavior of two application-relevant systems from the free to the strongly confined conditions. From this study is possible to compare the transport behavior of Brownian particles and active self-propelling bacteria in response to the imposed confinement. The present work highlights the consistent reduction of the transport properties of both of the investigated systems in relation to the increase in the confinement imposed by the decrease in the pores' diameter; the confinement effects are already present in pores with dimensions of an order of magnitude greater than the characteristic dimensions of the

investigated systems. The pNIPAM particles, as well as the *B. subtilis* cells are substantially stuck when observed in the conditions of maximum confinement imposed by pores with diameters approximately double the size of the investigated systems. The diffusion exponent is strongly influenced by the structural confinement imposed by the porous matrix; the pNIPAM microgels, which in unconfined conditions expose normal diffusive Brownian motion, reflect a transition to sub-diffusive motion when confined. On the other hand, *B. subtilis* exhibits active motion in unconfined conditions and the progressive increase in confinement induces a first transition to Brownian-like normal diffusive motions and only afterward, in conditions of extreme confinement, a second transition to sub-diffusive motives. In both of the systems, the decrease in the motion exponent and transport coefficient are consistent with the increase of the imposed confinement. The decrease of the exponent compared to the unconfined values is approximately 80 % in the case of the microgels and 75 % in the case of the bacteria; the slightly lower decrease of this parameter for bacteria suggests a possible residual influence of active motility even in confinement. Remarkably, the transport coefficients of microgels and bacteria decrease by one and three orders of magnitude respectively in strongly confining conditions compared to the free-diffusing systems. Note that the decrease in the transition from active diffusion to normal diffusion leads to a decrease of one order of magnitude while the transition from normal diffusing to sub-diffusing bacteria represents the greater decrease in the transport coefficient. In the case of microgels, the transport coefficient as a function of confinement length is described by the cylindrical pore model containing hydrodynamic and steric effects; the pronounced effect on diffusive properties in relation to the reduction of porosity confirms the importance of

hydrodynamic and steric effects of finite-sized particles and suggests the presence of particle-matrix interactions. However, the correct description of the transport properties of the investigated biological system requires a more detailed study of the speeds exhibited in response to the different degrees of imposed confinement; the adoption of a threshold speed consistent with the imposed confinement allows a better description of the running and permanence periods foreseen by the classic hop-and-trap model. Furthermore, in the case of bacterial transport the bacterium-bacterium and bacterium-matrix interaction is suggested by the jump length observed experimentally; which is always smaller than the pores of the neighboring structure, suggesting mediation of the sensory organs on the resulting motility. Future efforts will focus on expanding our research to understand bacteria with different motility characteristics, as well as self-driving active colloids. In addition, our goal is to consider the influence of flow fields and the presence of nutrients or antimicrobials in our investigations.

Bibliography

- [1] D. Nykypanchuk, H. H. Strey, D. A. Hoagland, Brownian motion of dna confined within a two-dimensional array, *Science* 297 (5583) (2002) 987–990.
- [2] W. Volkmuth, R. Austin, Dna electrophoresis in microlithographic arrays, *Nature* 358 (6387) (1992) 600–602.
- [3] D. M. Tartakovsky, M. Dentz, Diffusion in porous media: phenomena and mechanisms, *Transport in Porous Media* 130 (2019) 105–127.
- [4] L. Ning, P. Liu, F. Ye, M. Yang, K. Chen, Diffusion of colloidal particles in model porous media, *Physical Review E* 103 (2) (2021) 022608.
- [5] R. Raccis, A. Nikoubashman, M. Retsch, U. Jonas, K. Koynov, H.-J. Butt, C. N. Likos, G. Fytas, Confined diffusion in periodic porous nanostructures, *Acs Nano* 5 (6) (2011) 4607–4616.
- [6] K. He, F. Babaye Khorasani, S. T. Retterer, D. K. Thomas, J. C. Conrad, R. Krishnamoorti, Diffusive dynamics of nanoparticles in arrays of nanoposts, *ACS nano* 7 (6) (2013) 5122–5130.
- [7] M. Binz, A. P. Lee, C. Edwards, D. V. Nicolau, Motility of bacteria in microfluidic structures, *Microelectronic Engineering* 87 (5-8) (2010) 810–813.

-
- [8] B. Libberton, M. Binz, H. Van Zalinge, D. V. Nicolau, Efficiency of the flagellar propulsion of *escherichia coli* in confined microfluidic geometries, *Physical Review E* 99 (1) (2019) 012408.
- [9] K. Marcel, F. Zahra, C. Martijn, et al., Injectable hydrogels from segmented peg-bisurea copolymers (2012).
- [10] I. Strehin, Z. Nahas, K. Arora, T. Nguyen, J. Elisseeff, A versatile pH sensitive chondroitin sulfate–peg tissue adhesive and hydrogel, *Biomaterials* 31 (10) (2010) 2788–2797.
- [11] F. Anjum, P. S. Lienemann, S. Metzger, J. Biernaskie, M. S. Kallos, M. Ehrbar, Enzyme responsive gag-based natural-synthetic hybrid hydrogel for tunable growth factor delivery and stem cell differentiation, *Biomaterials* 87 (2016) 104–117.
- [12] F. Della Sala, M. Biondi, D. Guarnieri, A. Borzacchiello, L. Ambrosio, L. Mayol, Mechanical behavior of bioactive poly (ethylene glycol) diacrylate matrices for biomedical application, *Journal of the Mechanical Behavior of Biomedical Materials* 110 (2020) 103885.
- [13] J. Alemán, A. V. Chadwick, J. He, M. Hess, K. Horie, R. G. Jones, P. Kratochvíl, I. Meisel, I. Mita, G. Moad, et al., Definitions of terms relating to the structure and processing of sols, gels, networks, and inorganic-organic hybrid materials (iupac recommendations 2007), *Pure and Applied Chemistry* 79 (10) (2007) 1801–1829.
- [14] P. J. Flory, *Principles of polymer chemistry*, Cornell university press, 1953.
- [15] D. Stauffer, A. Coniglio, M. Adam, Gelation and critical phenomena, in: *Polymer networks*, Springer, 2005, pp. 103–158.
- [16] P. Meakin, Models for colloidal aggregation, *Annual Review of Physical Chemistry* 39 (1) (1988) 237–267.

- [17] R. Izadi, M. Mahinroosta, K. Mohammadzadeh, S. N. Ashrafzadeh, An inclusive review on inorganic gels: classifications, synthesis methods and applications, *Journal of the Iranian Chemical Society* (2023) 1–23.
- [18] H. Yang, J. Sun, Y. Zhang, Q. Xue, S. Xia, Preparation of hydrophobic carbon aerogel using cellulose extracted from luffa sponge for adsorption of diesel oil, *Ceramics International* 47 (23) (2021) 33827–33834.
- [19] O. Korhonen, T. Budtova, All-cellulose composite aerogels and cryogels, *Composites Part A: Applied Science and Manufacturing* 137 (2020) 106027.
- [20] A. Du, B. Zhou, Z. Zhang, J. Shen, A special material or a new state of matter: a review and reconsideration of the aerogel, *Materials* 6 (3) (2013) 941–968.
- [21] A. Yamauchi, Gels: introduction, in: *Gels handbook*, Elsevier, 2001, pp. 4–12.
- [22] J. P. Rolland, B. W. Maynor, L. E. Euliss, A. E. Exner, G. M. Denison, J. M. DeSimone, Direct fabrication and harvesting of monodisperse, shape-specific nanobiomaterials, *Journal of the American Chemical Society* 127 (28) (2005) 10096–10100.
- [23] M. D. Tang, A. P. Golden, J. Tien, Molding of three-dimensional microstructures of gels, *Journal of the American Chemical Society* 125 (43) (2003) 12988–12989.
- [24] Z. Nie, W. Li, M. Seo, S. Xu, E. Kumacheva, Janus and ternary particles generated by microfluidic synthesis: design, synthesis, and self-assembly, *Journal of the American Chemical Society* 128 (29) (2006) 9408–9412.

-
- [25] J. K. Oh, R. Drumright, D. J. Siegwart, K. Matyjaszewski, The development of microgels/nanogels for drug delivery applications, *Progress in polymer science* 33 (4) (2008) 448–477.
- [26] J. K. Dhont, *An introduction to dynamics of colloids*, Elsevier, 1996.
- [27] U. Deichmann, *âmolecularâ versus âcolloidalâ: controversies in biology and biochemistry, 1900–1940*, *Bulletin for the History of Chemistry* 32 (2) (2007).
- [28] J. N. Israelachvili, Contrasts between intermolecular, interparticle and intersurface forces, *Intermolecular and surface forces* 11 (2011) 205–222.
- [29] J. Perrin, *Brownian movement and molecular reality*, Courier Corporation, 2013.
- [30] A. Einstein, *Über die von der molekularkinetischen theorie der wärme geforderte bewegung von in ruhenden flüssigkeiten suspendierten teilchen*, *Annalen der physik* 4 (1905).
- [31] P. Langevin, *Sur la théorie du mouvement brownien*, *Compt. Rendus* 146 (1908) 530–533.
- [32] A. Einstein, *Eine neue bestimmung der moleküldimensionen*, Ph.D. thesis, ETH Zurich (1905).
- [33] I. L. Molnar, W. P. Johnson, J. I. Gerhard, C. S. Willson, D. M. O’carroll, Predicting colloid transport through saturated porous media: A critical review, *Water Resources Research* 51 (9) (2015) 6804–6845.
- [34] W. Coffey, Y. P. Kalmykov, *The Langevin equation: with applications to stochastic problems in physics, chemistry and electrical engineering*, Vol. 27, World Scientific, 2012.

-
- [35] K. E. Nelson, T. R. Ginn, New collector efficiency equation for colloid filtration in both natural and engineered flow conditions, *Water Resources Research* 47 (5) (2011).
- [36] I. S. Aranson, Active colloids, *Physics-Uspekhi* 56 (1) (2013) 79.
- [37] R. Di Leonardo, Controlled collective motions, *Nature materials* 15 (10) (2016) 1057–1058.
- [38] J. J. Falke, R. B. Bass, S. L. Butler, S. A. Chervitz, M. A. Danielson, The two-component signaling pathway of bacterial chemotaxis: a molecular view of signal transduction by receptors, kinases, and adaptation enzymes, *Annual review of cell and developmental biology* 13 (1) (1997) 457–512.
- [39] J. L. Spudich, C.-S. Yang, K.-H. Jung, E. N. Spudich, Retinylidene proteins: structures and functions from archaea to humans, *Annual review of cell and developmental biology* 16 (1) (2000) 365–392.
- [40] M. Khatami, K. Wolff, O. Pohl, M. R. Ejtehadi, H. Stark, Active brownian particles and run-and-tumble particles separate inside a maze, *Scientific reports* 6 (1) (2016) 37670.
- [41] G. Volpe, I. Buttinoni, D. Vogt, H.-J. Kümmerer, C. Bechinger, Microswimmers in patterned environments, *Soft Matter* 7 (19) (2011) 8810–8815.
- [42] A. Ghosh, P. Fischer, Controlled propulsion of artificial magnetic nanostructured propellers, *Nano letters* 9 (6) (2009) 2243–2245.
- [43] H.-R. Jiang, N. Yoshinaga, M. Sano, Active motion of a janus particle by self-thermophoresis in a defocused laser beam, *Physical review letters* 105 (26) (2010) 268302.

-
- [44] C. Bechinger, R. Di Leonardo, H. Löwen, C. Reichhardt, G. Volpe, G. Volpe, Active particles in complex and crowded environments, *Reviews of Modern Physics* 88 (4) (2016) 045006.
- [45] M. E. Cates, J. Tailleur, When are active brownian particles and run-and-tumble particles equivalent? consequences for motility-induced phase separation, *Europhysics Letters* 101 (2) (2013) 20010.
- [46] A. A. Salyers, D. D. Whitt, D. D. Whitt, *Bacterial pathogenesis: a molecular approach*, Vol. 1, ASM press Washington, DC, 1994.
- [47] N. Woodford, D. M. Livermore, Infections caused by gram-positive bacteria: a review of the global challenge, *Journal of Infection* 59 (2009) S4–S16.
- [48] O. Habimana, A. Semião, E. Casey, The role of cell-surface interactions in bacterial initial adhesion and consequent biofilm formation on nanofiltration/reverse osmosis membranes, *Journal of Membrane Science* 454 (2014) 82–96.
- [49] T. A. Harper, S. Bridgewater, L. Brown, P. Pow-Brown, A. Stewart-Johnson, A. A. Adesiyun, Bioaerosol sampling for airborne bacteria in a small animal veterinary teaching hospital, *Infection ecology & epidemiology* 3 (1) (2013) 20376.
- [50] Y. Asada, J. Miyake, Photobiological hydrogen production, *Journal of bioscience and bioengineering* 88 (1) (1999) 1–6.
- [51] A. Esmaeili, A. A. Pourbabae, H. A. Alikhani, F. Shabani, E. Esmaeili, Biodegradation of low-density polyethylene (ldpe) by mixed culture of *lysini bacillus xylanilyticus* and *aspergillus niger* in soil, *Plos one* 8 (9) (2013) e71720.
- [52] J. Henrichsen, Bacterial surface translocation: a survey and a classification, *Bacteriological reviews* 36 (4) (1972) 478–503.

-
- [53] B. Nan, D. R. Zusman, Novel mechanisms power bacterial gliding motility, *Molecular microbiology* 101 (2) (2016) 186–193.
- [54] V. Palma, M. S. Gutiérrez, O. Vargas, R. Parthasarathy, P. Navarrete, Methods to evaluate bacterial motility and its role in bacterial–host interactions, *Microorganisms* 10 (3) (2022) 563.
- [55] D. B. Kearns, A field guide to bacterial swarming motility, *Nature Reviews Microbiology* 8 (9) (2010) 634–644.
- [56] N. R. Francis, G. E. Sosinsky, D. Thomas, D. J. DeRosier, Isolation, characterization and structure of bacterial flagellar motors containing the switch complex, *Journal of molecular biology* 235 (4) (1994) 1261–1270.
- [57] H. Suzuki, K. Yonekura, K. Namba, Structure of the rotor of the bacterial flagellar motor revealed by electron cryomicroscopy and single-particle image analysis, *Journal of molecular biology* 337 (1) (2004) 105–113.
- [58] D. R. Thomas, N. R. Francis, C. Xu, D. J. DeRosier, The three-dimensional structure of the flagellar rotor from a clockwise-locked mutant of salmonella enterica serovar typhimurium, *Journal of bacteriology* 188 (20) (2006) 7039–7048.
- [59] M. D. Manson, P. Tedesco, H. C. Berg, F. M. Harold, C. Van der Drift, A protonmotive force drives bacterial flagella., *Proceedings of the National Academy of Sciences* 74 (7) (1977) 3060–3064.
- [60] D. F. Blair, H. C. Berg, Restoration of torque in defective flagellar motors, *Science* 242 (4886) (1988) 1678–1681.
- [61] D. B. Kearns, R. Losick, Swarming motility in undomesticated bacillus subtilis, *Molecular microbiology* 49 (3) (2003) 581–590.

- [62] L. Minnullina, Z. Kostennikova, V. Evtugin, Y. Akosah, M. Sharipova, A. Mardanova, Diversity in the swimming motility and flagellar regulon structure of uropathogenic *morganella morganii* strains, *International Microbiology* (2022) 1–12.
- [63] L. Turner, W. S. Ryu, H. C. Berg, Real-time imaging of fluorescent flagellar filaments, *Journal of bacteriology* 182 (10) (2000) 2793–2801.
- [64] A. Villa-Torrealba, C. Chávez-Raby, P. de Castro, R. Soto, Run-and-tumble bacteria slowly approaching the diffusive regime, *Physical Review E* 101 (6) (2020) 062607.
- [65] V. Torchilin, Tumor delivery of macromolecular drugs based on the epr effect, *Advanced drug delivery reviews* 63 (3) (2011) 131–135.
- [66] G. Bitton, R. W. Harvey, Transport of pathogens through soils and aquifers, *Environmental microbiology* 19 (1992) 103–123.
- [67] S. A. Bradford, R. W. Harvey, Future research needs involving pathogens in groundwater, *Hydrogeology Journal* 25 (4) (2017) 931.
- [68] H. van Beijeren, Transport properties of stochastic lorentz models, *Reviews of Modern Physics* 54 (1) (1982) 195.
- [69] F. Höfling, T. Franosch, E. Frey, Localization transition of the three-dimensional lorentz model and continuum percolation, *Physical review letters* 96 (16) (2006) 165901.
- [70] T. O. Skinner, S. K. Schnyder, D. G. Aarts, J. Horbach, R. P. Dullens, Localization dynamics of fluids in random confinement, *Physical Review Letters* 111 (12) (2013) 128301.
- [71] J. M. Zalc, S. C. Reyes, E. Iglesia, The effects of diffusion mechanism and void structure on transport rates and tortuosity fac-

- tors in complex porous structures, *Chemical Engineering Science* 59 (14) (2004) 2947–2960.
- [72] S. H. Park, Y. Xia, Fabrication of three-dimensional macroporous membranes with assemblies of microspheres as templates, *Chemistry of materials* 10 (7) (1998) 1745–1747.
- [73] M. Nishita, S.-Y. Park, T. Nishio, K. Kamizaki, Z. Wang, K. Tamada, T. Takumi, R. Hashimoto, H. Otani, G. J. Pazour, et al., Ror2 signaling regulates golgi structure and transport through ift20 for tumor invasiveness, *Scientific Reports* 7 (1) (2017) 1.
- [74] S. C. Takatori, J. F. Brady, Forces, stresses and the (thermo?) dynamics of active matter, *Current Opinion in Colloid & Interface Science* 21 (2016) 24–33.
- [75] W. Yan, J. F. Brady, The force on a boundary in active matter, *Journal of Fluid Mechanics* 785 (2015) R1.
- [76] S. Das, G. Gompper, R. G. Winkler, Confined active brownian particles: theoretical description of propulsion-induced accumulation, *New Journal of Physics* 20 (1) (2018) 015001.
- [77] P. Hänggi, P. Jung, Colored noise in dynamical systems, *Advances in chemical physics* 89 (1994) 239–326.
- [78] P. Galajda, J. Keymer, P. Chaikin, R. Austin, A wall of funnels concentrates swimming bacteria, *Journal of bacteriology* 189 (23) (2007) 8704–8707.
- [79] K. Schaar, A. Zöttl, H. Stark, Detention times of microswimmers close to surfaces: Influence of hydrodynamic interactions and noise, *Physical review letters* 115 (3) (2015) 038101.
- [80] A. T. Brown, I. D. Vladescu, A. Dawson, T. Vissers, J. Schwarz-Linek, J. S. Lintuvuori, W. C. Poon, Swimming in a crystal, *Soft matter* 12 (1) (2016) 131–140.

- [81] V. Tokárová, A. Sudalaiyadum Perumal, M. Nayak, H. Shum, O. Kašpar, K. Rajendran, M. Mohammadi, C. Tremblay, E. A. Gaffney, S. Martel, et al., Patterns of bacterial motility in microfluidics-confining environments, *Proceedings of the National Academy of Sciences* 118 (17) (2021) e2013925118.
- [82] M. Brun-Cosme-Bruny, E. Bertin, B. Coasne, P. Peyla, S. Rafaï, Effective diffusivity of microswimmers in a crowded environment, *The Journal of chemical physics* 150 (10) (2019).
- [83] T. Bhattacharjee, S. S. Datta, Confinement and activity regulate bacterial motion in porous media, *Soft Matter* 15 (48) (2019) 9920–9930.
- [84] C. Reichhardt, C. Reichhardt, Directional locking effects for active matter particles coupled to a periodic substrate, *Physical Review E* 102 (4) (2020) 042616.
- [85] A. J. Mathijssen, N. Figueroa-Morales, G. Junot, É. Clément, A. Lindner, A. Zöttl, Oscillatory surface rheotaxis of swimming *e. coli* bacteria, *Nature communications* 10 (1) (2019) 3434.
- [86] V. Kantsler, J. Dunkel, M. Blayney, R. E. Goldstein, Rheotaxis facilitates upstream navigation of mammalian sperm cells, *Elife* 3 (2014) e02403.
- [87] A. Costanzo, R. Di Leonardo, G. Ruocco, L. Angelani, Transport of self-propelling bacteria in micro-channel flow, *Journal of Physics: Condensed Matter* 24 (6) (2012) 065101.
- [88] J. Taktikos, H. Stark, V. Zaburdaev, How the motility pattern of bacteria affects their dispersal and chemotaxis, *PloS one* 8 (12) (2013) e81936.
- [89] A. J. Wolfe, H. C. Berg, Migration of bacteria in semisolid agar., *Proceedings of the National Academy of Sciences* 86 (18) (1989) 6973–6977.

-
- [90] H. C. Berg, *Random walks in biology*, Princeton University Press, 1993.
- [91] A. Baumgärtner, M. Muthukumar, A trapped polymer chain in random porous media, *The Journal of chemical physics* 87 (5) (1987) 3082–3088.
- [92] M. Muthukumar, A. Baumgärtner, Effects of entropic barriers on polymer dynamics, *Macromolecules* 22 (4) (1989) 1937–1941.
- [93] D. Lauffenburger, C. R. Kennedy, R. Aris, Traveling bands of chemotactic bacteria in the context of population growth, *Bulletin of Mathematical Biology* 46 (1) (1984) 19–40.
- [94] N. A. Licata, B. Mohari, C. Fuqua, S. Setayeshgar, Diffusion of bacterial cells in porous media, *Biophysical journal* 110 (1) (2016) 247–257.
- [95] T. Bhattacharjee, S. S. Datta, Bacterial hopping and trapping in porous media, *Nature communications* 10 (1) (2019) 2075.
- [96] S. Ali, M. L. Cuchiara, J. L. West, Micropatterning of poly (ethylene glycol) diacrylate hydrogels, in: *Methods in Cell Biology*, Vol. 121, Elsevier, 2014, pp. 105–119.
- [97] S. Lee, X. Tong, F. Yang, Effects of the poly (ethylene glycol) hydrogel crosslinking mechanism on protein release, *Biomaterials science* 4 (3) (2016) 405–411.
- [98] C.-C. Lin, K. S. Anseth, Peg hydrogels for the controlled release of biomolecules in regenerative medicine, *Pharmaceutical research* 26 (2009) 631–643.
- [99] W. Yang, H. Yu, W. Liang, Y. Wang, L. Liu, Rapid fabrication of hydrogel microstructures using uv-induced projection printing, *Micromachines* 6 (12) (2015) 1903–1913.

-
- [100] M. Rossi, Gels based systems for the development of functional materials', University of Florence (2019).
- [101] H. Shimizu, R. Wada, M. Okabe, Preparation and characterization of micrometer-sized poly (n-isopropylacrylamide) hydrogel particles, *Polymer journal* 41 (9) (2009) 771–777.
- [102] A. Pich, W. Richtering, Microgels by precipitation polymerization: synthesis, characterization, and functionalization, *Chemical design of responsive microgels* (2011) 1–37.
- [103] C. Kurzthaler, L. Gentile, H. A. Stone, *Out-of-equilibrium Soft Matter: Active Fluids*, Vol. 17, Royal Society of Chemistry, 2023.
- [104] Y. Hatwalne, S. Ramaswamy, M. Rao, R. A. Simha, Rheology of active-particle suspensions, *Physical review letters* 92 (11) (2004) 118101.
- [105] A. Sokolov, I. S. Aranson, Reduction of viscosity in suspension of swimming bacteria, *Physical review letters* 103 (14) (2009) 148101.
- [106] D. Saintillan, The dilute rheology of swimming suspensions: A simple kinetic model, *Experimental Mechanics* 50 (2010) 1275–1281.
- [107] P. J. Flory, J. Rehner Jr, Statistical mechanics of cross-linked polymer networks ii. swelling, *The journal of chemical physics* 11 (11) (1943) 521–526.
- [108] R. H. COLBY, Chapel hill, north carolina, usa (2003).
- [109] M. S. Jhon, J. D. Andrade, Water and hydrogels, *Journal of biomedical materials research* 7 (6) (1973) 509–522.
- [110] F. Müller-Plathe, Different states of water in hydrogels?, *Macromolecules* 31 (19) (1998) 6721–6723.

-
- [111] V. M. Gunâko, I. N. Savina, S. V. Mikhalovsky, Properties of water bound in hydrogels, *Gels* 3 (4) (2017) 37.
- [112] P. Bhagwan, *A handbook of thermodynamics*, Mittal Publications, 2005.
- [113] R.-J. Roe, *Methods of x-ray and neutron scattering in polymer science*, (No Title) (2000).
- [114] T. Blanton, T. Huang, H. Toraya, C. Hubbard, S. Robie, D. Louer, H. Göbel, G. Will, R. Gilles, T. Raftery, Jcpdsâinternational centre for diffraction data round robin study of silver behenate. a possible low-angle x-ray diffraction calibration standard, *Powder Diffraction* 10 (2) (1995) 91–95.
- [115] F. Zhang, J. Ilavsky, G. G. Long, J. P. Quintana, A. J. Allen, P. R. Jemian, Glassy carbon as an absolute intensity calibration standard for small-angle scattering, *Metallurgical and Materials Transactions A* 41 (2010) 1151–1158.
- [116] P. Debye, A. Bueche, Scattering by an inhomogeneous solid, *Journal of Applied Physics* 20 (6) (1949) 518–525.
- [117] L. S. Ornstein, Accidental deviations of density and opalescence at the critical point of a single substance, *Proc. Akad. Sci.* 17 (1914) 793.
- [118] G. Porod, Die röntgenkleinwinkelstreuung von dichtgepackten kolloiden systemen: I. teil, *Kolloid-Zeitschrift* 124 (2) (1951) 83–114.
- [119] F. Ikkai, M. Shibayama, Inhomogeneity control in polymer gels, *Journal of Polymer Science Part B: Polymer Physics* 43 (6) (2005) 617–628.
- [120] T. Sakai, Experimental verification of homogeneity in polymer gels, *Polymer Journal* 46 (9) (2014) 517–523.

- [121] J. C. Crocker, D. G. Grier, Methods of digital video microscopy for colloidal studies, *Journal of colloid and interface science* 179 (1) (1996) 298–310.
- [122] D. Legland, I. Arganda-Carreras, P. Andrey, Morpholibj: integrated library and plugins for mathematical morphology with imagej, *Bioinformatics* 32 (22) (2016) 3532–3534.
- [123] H. H. Winter, F. Chambon, Analysis of linear viscoelasticity of a crosslinking polymer at the gel point, *Journal of rheology* 30 (2) (1986) 367–382.
- [124] K. Almdal, J. Dyre, S. Hvidt, O. Kramer, Towards a phenomenological definition of the term *âgelâ*, *Polymer gels and networks* 1 (1) (1993) 5–17.
- [125] A. Diaspro, *Nanoscopy and multidimensional optical fluorescence microscopy*, CRC press, 2010.
- [126] D. B. Allan, T. Caswell, N. C. Keim, C. M. van der Wel, R. W. Verweij, *soft-matter/trackpy: Trackpy v0. 5.0*, Zenodo repository (2021).
- [127] T. Wagner, A. Kroll, C. R. Haramagatti, H. G. Lipinski, M. Wiemann, Classification and segmentation of nanoparticle diffusion trajectories in cellular micro environments, *PLoS ONE* 12 (1) (2017) 1–20. doi:10.1371/journal.pone.0170165.
- [128] J.-Y. Tinevez, N. Perry, J. Schindelin, G. M. Hoopes, G. D. Reynolds, E. Laplantine, S. Y. Bednarek, S. L. Shorte, K. W. Eliceiri, TrackMate: An open and extensible platform for single-particle tracking, *Methods* 115 (2016) (2017) 80–90. doi:10.1016/j.ymeth.2016.09.016.
URL <http://dx.doi.org/10.1016/j.ymeth.2016.09.016>
<https://linkinghub.elsevier.com/retrieve/pii/S1046202316303346>

- [129] D. Ershov, M.-s. Phan, J. W. Pylvänäinen, S. U. Rigaud, L. L. Blanc, J. R. W. Conway, R. F. Laine, N. H. Roy, D. Bonazzi, G. Duménil, G. Jacquemet, J.-y. Tinevez, Bringing TrackMate into the era of (2021) 9–12doi:<https://doi.org/10.1101/2021.09.03.458852>.
URL <https://doi.org/10.1101/2021.09.03.458852>
- [130] K. Jaqaman, D. Loerke, M. Mettlen, H. Stein, S. Schmid and G. Danuser, *Nature Methods* 5 (2008) 695–702.
- [131] E. I. Wisotzki, P. Tempesti, E. Fratini, S. G. Mayr, Influence of high energy electron irradiation on the network structure of gelatin hydrogels as investigated by small-angle x-ray scattering (saxs), *Physical Chemistry Chemical Physics* 19 (19) (2017) 12064–12074.
- [132] R. Mastrangelo, D. Chelazzi, G. Poggi, E. Fratini, L. Pensabene Buemi, M. L. Petruzzellis, P. Baglioni, Twin-chain polymer hydrogels based on poly (vinyl alcohol) as new advanced tool for the cleaning of modern and contemporary art, *Proceedings of the National Academy of Sciences* 117 (13) (2020) 7011–7020.
- [133] W. Ruland, Small-angle scattering of two-phase systems: determination and significance of systematic deviations from porod's law, *Journal of Applied Crystallography* 4 (1) (1971) 70–73.
- [134] G. Shao, D. A. Hanaor, X. Shen, A. Gurlo, Freeze casting: from low-dimensional building blocks to aligned porous structures—a review of novel materials, methods, and applications, *Advanced Materials* 32 (17) (2020) 1907176.
- [135] H. Nishihara, S. R. Mukai, D. Yamashita, H. Tamon, Ordered macroporous silica by ice templating, *Chemistry of materials* 17 (3) (2005) 683–689.

-
- [136] R. Pelton, Temperature-sensitive aqueous microgels, *Advances in colloid and interface science* 85 (1) (2000) 1–33.
- [137] T. Moschakis, B. S. Murray, E. Dickinson, Particle tracking using confocal microscopy to probe the microrheology in a phase-separating emulsion containing nonadsorbing polysaccharide, *Langmuir* 22 (10) (2006) 4710–4719.
- [138] V. Breedveld, D. Pine, Microrheology as a tool for high-throughput screening, *Journal of materials science* 38 (2003) 4461–4470.
- [139] E. Lushi, H. Wioland, R. E. Goldstein, Fluid flows created by swimming bacteria drive self-organization in confined suspensions, *Proceedings of the National Academy of Sciences* 111 (27) (2014) 9733–9738.
- [140] J. M. Nitsche, G. Balgi, Hindered brownian diffusion of spherical solutes within circular cylindrical pores, *Industrial & engineering chemistry research* 33 (9) (1994) 2242–2247.
- [141] M. J. Skaug, L. Wang, Y. Ding, D. K. Schwartz, Hindered nanoparticle diffusion and void accessibility in a three-dimensional porous medium, *ACS nano* 9 (2) (2015) 2148–2156.
- [142] F. Babayekhorasani, D. E. Dunstan, R. Krishnamoorti, J. C. Conrad, Nanoparticle diffusion in crowded and confined media, *Soft Matter* 12 (40) (2016) 8407–8416.
- [143] J. A. Dix, A. Verkman, Crowding effects on diffusion in solutions and cells, *Annu. Rev. Biophys.* 37 (2008) 247–263.
- [144] F. Roosen-Runge, M. Hennig, F. Zhang, R. M. Jacobs, M. Sztucki, H. Schober, T. Seydel, F. Schreiber, Protein self-diffusion in crowded solutions, *Proceedings of the National Academy of Sciences* 108 (29) (2011) 11815–11820.

-
- [145] K. H. Langley, I. Teraoka, 7. light scattering and other optical methods, in: *Experimental Methods in the Physical Sciences*, Vol. 35, Elsevier, 1999, pp. 263–300.
- [146] E. M. Renkin, Filtration, diffusion, and molecular sieving through porous cellulose membranes, *The Journal of General Physiology* 39 (5) (1956) 820.
- [147] H. Brenner, L. J. Gaydos, The constrained brownian movement of spherical particles in cylindrical pores of comparable radius: Models of the diffusive and convective transport of solute molecules in membranes and porous media, *Journal of Colloid and Interface Science* 58 (2) (1977) 312–356.
- [148] G. M. Mavrovouniotis, H. Brenner, Hindered sedimentation, diffusion, and dispersion coefficients for brownian spheres in circular cylindrical pores, *Journal of Colloid and Interface Science* 124 (1) (1988) 269–283.
- [149] J. Higdon, G. Muldowney, Resistance functions for spherical particles, droplets and bubbles in cylindrical tubes, *Journal of Fluid Mechanics* 298 (1995) 193–210.
- [150] J. Happel, H. Brenner, *Low Reynolds number hydrodynamics: with special applications to particulate media*, Vol. 1, Springer Science & Business Media, 1983.
- [151] Y. Pawar, J. L. Anderson, Hindered diffusion in slit pores: an analytical result, *Industrial & engineering chemistry research* 32 (4) (1993) 743–746.
- [152] N. Ray, A. Rupp, R. Schulz, P. Knabner, Old and new approaches predicting the diffusion in porous media, *Transport in Porous Media* 124 (2018) 803–824.
- [153] A. Creppy, E. Clément, C. Douarche, M. V. D’Angelo, H. Auradou, Effect of motility on the transport of bacteria populations

- through a porous medium, *Physical Review Fluids* 4 (1) (2019) 1–16. [arXiv:1802.01879](https://arxiv.org/abs/1802.01879), [doi:10.1103/PhysRevFluids.4.013102](https://doi.org/10.1103/PhysRevFluids.4.013102).
- [154] G. Ariel, A. Rabani, S. Benisty, J. D. Partridge, R. M. Harshey, A. Be’Er, Swarming bacteria migrate by lévy walk, *Nature communications* 6 (1) (2015) 1–6.
- [155] F. HÄffling, T. Franosch, Anomalous transport in the crowded world of biological cells, *Reports on Progress in Physics* 76 (4) (2013) 046602. [doi:10.1088/0034-4885/76/4/046602](https://doi.org/10.1088/0034-4885/76/4/046602).
URL <https://dx.doi.org/10.1088/0034-4885/76/4/046602>
- [156] J.-H. Jeon, A. V. Chechkin, R. Metzler, Scaled brownian motion: a paradoxical process with a time dependent diffusivity for the description of anomalous diffusion, *Phys. Chem. Chem. Phys.* 16 (2014) 15811–15817. [doi:10.1039/C4CP02019G](https://doi.org/10.1039/C4CP02019G).
URL <http://dx.doi.org/10.1039/C4CP02019G>
- [157] J. C. Conrad, R. Poling-Skutvik, Confined flow: consequences and implications for bacteria and biofilms, *Annual review of chemical and biomolecular engineering* 9 (2018) 175–200.
- [158] J. Männik, R. Driessen, P. Galajda, J. E. Keymer, C. Dekker, Bacterial growth and motility in sub-micron constrictions, *Proceedings of the National Academy of Sciences* 106 (35) (2009) 14861–14866.
- [159] C. R. Haramagatti, F. H. Schacher, A. H. Müller, J. Köhler, Diblock copolymer membranes investigated by single-particle tracking, *Physical Chemistry Chemical Physics* 13 (6) (2011) 2278–2284.
- [160] M. J. Saxton, K. Jacobson, Single-particle tracking: applications to membrane dynamics, *Annual review of biophysics and biomolecular structure* 26 (1) (1997) 373–399.

- [161] J. Han, S. Turner, H. G. Craighead, Entropic trapping and escape of long dna molecules at submicron size constriction, *Physical review letters* 83 (8) (1999) 1688.
- [162] M. Muthukumar, A. Baumgärtner, Diffusion of a polymer chain in random media, *Macromolecules* 22 (4) (1989) 1941–1946.
- [163] K. Trachenko, A. Zaccone, Slow stretched-exponential and fast compressed-exponential relaxation from local event dynamics, *Journal of Physics: Condensed Matter* 33 (31) (2021) 315101.

Appendix A

Publications

This research activity has led to several publications in international journals and conferences. These are summarized below.¹

¹The author's bibliometric indices are the following: *H*-index = X, total number of citations = XX (source: Google Scholar on Month XX, 201x).

International Journals

1. **Gavino Bassu**, Marco Laurati, and Emiliano Fratini. “Microgel dynamics within the 3D porous structure of transparent PEG hydrogels”, *Colloids and Surfaces B: Biointerfaces*, vol. 221.,2023. [DOI:10.1016/j.colsurfb.2022.112938]
2. **Vanessa Rosciardi**, Daminano Bandelli, Gavino Bassu, and Piero Baglioni. “Highly Biocidal Poly (vinyl alcohol)-Hydantoin/Starch Hybrid Gels: a ”Trojan Horse” for *Bacillus subtilis*”, *Journal of Colloid and Interface Science* , vol. 657, pp. 788-798, 2024. [DOI: 10.1016/j.jcis.2023.11.142]
3. **Marina Macchiagodena**, Gavino Bassu, Irene Vettori, Emiliano Fratini, Piero Procacci, and Marco Pagliai. “2-Butanol Aqueous Solutions: A Combined Molecular Dynamics and Small/Wide Angle X-ray Scattering Study.”, *The Journal of Physical Chemistry A*, vol. 126, iss. 47, pp. 8826-8833, 2022. [DOI: 10.1021/acs.jpca.2c05708]
4. **Fernando Soto-Bustamanante**, Gavino Bassu, Emiliano Fratini, and Marco Laurati. “Effect of Composition and Freeze-Thaw on the Network Structure, Porosity and Mechanical Properties of Polyvinyl-Alcohol/Chitosan Hydrogels.”, *Gels*, vol. 9, iss. 5, pp. 396, 2023. [DOI: 10.3390/gels9050396]
5. **Irene Vettori**, Marina Macchiagodena, Marco Pagliai, Gavino Bassu, Emiliano Fratini, and Piero Baglioni. “Conformational and solvent effects in structural and spectroscopic properties of 2-hydroxyethyl methacrylate and acrylic acid.”, *Journal of Molecular Liquids*, vol. 360, iss. 47, pp. 119428, 2022. [DOI: 10.1016/j.molliq.2022.119428]

Submitted

1. **Gavino Bassu**, Marco Laurati, and Emiliano Fratini. “Transition from active motion to anomalous diffusion for *Bacillus subtilis* confined in hydrogel matrices”, *Colloids and Surfaces B: Biointerfaces*.
2. **Gavino Bassu**, Judith E. Houston, Mayra A. Lara-Peña, Hartmut Kriegs, Minne Paul Lettinga, Lionel Porcar, Andrea Scotti, and Marco Laurati. “Link between permanent shear-banding and local concentration fluctuations in suspensions of compressible microgels”, *Physical Review Letters*.

National and International Oral Contributes

- OC01 Bassu G.**, Laurati M., Fratini E.. Poly(ethylene glycol)-based hydrogels as transparent porous network for diffusivity studies. 1st Picsu Chemistry PhD Symposium 2022, Sesto Fiorentino (Italy), 19th - 21th January 2022.
- OC02 Bassu G.**, Laurati M., Fratini E.. Micro-gel in transparent porous hydrogel: synthesis, morphological characterization, and diffusivity studies. Polymer network chemistry PNG 2022 Rome (Italy), 12-16 June 2022.
- OC03 Bassu G.**, Laurati M., Fratini E.. Diffusive transport of micro-gel in transparent micro-sized porous hydrogel. XLVIII National Congress of Physical Chemistry, Genoa (Italy), 4-7 July 2022.
- OC04 Bassu G.**, Laurati M., Fratini E.. Fast and Bacterious: diffusivity study of bacteria in confining hydrogel. Next Generation Chemists 2022, Cagliari (Italy), 4th-5th November 2022.
- OC05 Bassu G.**, Laurati M., Fratini E.. Fast and Bacterious: motility drift from super to sub-diffusion behavior. 2nd Picsu Chem-

istry PhD Symposium 2023, Sesto Fiorentino (Italy), 25th - 26th January 2023.

OC06 Bassu G., Laurati M., Fratini E.. Transition from active motion to anomalous diffusion of *Bacillus subtilis* confined in hydrogel matrices. The 7th International Soft Matter Conference ISMC 2023, Osaka (Japan), 4th-8th September 2023.

Poster Communications

PC01 Bassu G., Laurati M., Fratini E.. Transparent porous hydrogel for characterization of micro-particle diffusion. INTERFACES INTERNATIONAL CONFERENCE From new materials to life science - Structure, Interactions, Dynamics and Activity, Pula (CA) (Italy), September 21-25, 2021.

PC02 Vettori I., **Bassu G.**, Macchiagodena M., Pagliai M., Fratini E.. Hydrogels improvements through freeze-casting and anti-freezing additives. INTERFACES INTERNATIONAL CONFERENCE From new materials to life science â Structure, Interactions, Dynamics and Activity, Pula (CA) (Italy), September 21-25, 2021.

PC03 Bassu G., Laurati M., Fratini E.. Confining effects of transparent PEG hydrogels on microgel transport. 36th European Colloid & Interface Society Conference 4 - 9 September 2022 Chania, Crete, Greece.

PC04 Rosciardi V., Bandelli D., **Bassu G.**, Casu I., Baglioni P.. Starch/Poly(Vinyl Alcohol-Vinyl Hydantoin) Hydrogels with active biocidal effect: from polymer functionalization to the real-time observation of the gels' efficacy against model bacteria through confocal laser scanning microscopy.

A.0.1 Attached Publications



Microgel dynamics within the 3D porous structure of transparent PEG hydrogels

Author: Gavino Bassu, Marco Laurati, Emiliano Fratini

Publication: Colloids and Surfaces B: Biointerfaces

Publisher: Elsevier

Date: January 2023

© 2022 Elsevier B.V. All rights reserved.

Journal Author Rights

Please note that, as the author of this Elsevier article, you retain the right to include it in a thesis or dissertation, provided it is not published commercially. Permission is not required, but please ensure that you reference the journal as the original source. For more information on this and on your other retained rights, please visit: <https://www.elsevier.com/about/our-business/policies/copyright#Author-rights>

BACK

CLOSE WINDOW



Microgel dynamics within the 3D porous structure of transparent PEG hydrogels

Gavino Bassu^{1,2}, Marco Laurati^{1,3}, Emiliano Fratini^{*,4}

Department of Chemistry "Ugo Schiff" and CSGI, University of Florence, via della Lastruccia, 3 – Sesto Fiorentino, FI I-50019, Italy

ARTICLE INFO

Keywords:

Polyethylene glycol (PEG)
Hydrogel porosity
Tortuosity/morphological characterization
PNIPAM
Diffusion
Microgels

ABSTRACT

We report an investigation on the effects of the confinement imposed by application-relevant poly(ethylene glycol) (PEG) hydrogel matrices with controlled porosity on the dynamics of soft microgels. Through a detailed characterization of the internal structure of the hydrogels at the nano and microscale, we were able to link the microgel dynamics, measured by particle tracking, to the 3D geometrical confinement imposed by the porous matrices. PEG hydrogels with a high degree of transparency and tunable pore sizes and volume fractions were obtained using freeze-thawing. We found that the porosity of the hydrogel networks is characterized by elongated channels having asymmetric sections, with the average size decreasing from about 7 to about 2 particle diameters, and the size distribution becoming narrower with increasing PEG content in the pre-reaction mixture. The microgel dynamics slowdown and change from diffusive to sub-diffusive as a result of the increasing confinement. The observed decrease in diffusivity is consistent with models of diffusion in cylindrical pores and can be attributed to hydrodynamic and steric effects in addition to geometrical constriction. A dependence of the effective diffusion coefficient on the pore volume fraction, which is unusually pronounced, suggests the presence of microgel-hydrogel interactions. Our results demonstrate that a detailed characterization of the 3D geometry of the porous network is of primary importance for the understanding of transport properties in complex, random porous media.

1. Introduction

Many interesting phenomena in physics and biology, and applications in materials science, medicine, environmental science and geology, are associated with the diffusion of nanometric and micrometric colloidal particles in three-dimensional confining matrices[1]. For example micro-filtration using porous matrices is needed to preserve vehicles or instruments from unwanted particulates[1] or is used in recovery of valuable colloidal materials from waste products, as spent catalysts[2]. Specific processes to remove pollution rely on air and water filtration with porous materials. In environmental engineering and geosciences, there is a remarkable interest in predicting how bio-colloids, such as viruses and bacteria, travel through soils or other porous matrices[3–5]. In addition, there is large evidence that disease outbreaks can take place when pathogens are not correctly filtered[6–9].

Natural, non-harmful colloids are also capable of enhancing the transport of dissolved soil pollution through porous media by passive stochastic motion[10,11]. In all these cases, a detailed knowledge of the porous matrix's morphology, and of the particle-matrix interactions is a key feature to completely understand the diffusion properties of colloidal species and how the confinement conditions influence the particles' motion. Recent works addressed these issues by studying the diffusion properties of colloids in quasi-2D confining networks[12–14]. As a result of 2D confinement, the particles' trajectories reveal the existence of two different states of motion: a free-diffusion state, typically associated to diffusion of particles in the bulk, unconfined part of the fluid, and a trapped state in which particles inside confining *holes* present sub-diffusive motion. Studies of transport within ordered 3D structures were able to show the effect of obstacles and structural constraints on colloids' motion[15–17]. In particular, a linear decrease of

* Corresponding author.

E-mail address: emiliano.fratini@unifi.it (E. Fratini).

¹ G.B. and M.L. contributed equally to this work.

² ORCID: 0000-0001-8520-9919

³ ORCID: 0000-0003-1334-5940

⁴ ORCID: 0000-0001-7104-6530

<https://doi.org/10.1016/j.colsurfb.2022.112938>

Received 4 July 2022; Received in revised form 6 September 2022; Accepted 13 October 2022

Available online 18 October 2022

0927-7765/© 2022 Elsevier B.V. All rights reserved.



Highly biocidal poly(vinyl alcohol)-hydantoin/starch hybrid gels: A “Trojan Horse” for *Bacillus subtilis*

Author: Vanessa Rosciardi, Damiano Bandelli, Gavino Bassu, Iliaria Casu, Piero Baglioni

Publication: Journal of Colloid and Interface Science

Publisher: Elsevier

Date: March 2024

© 2023 The Author(s). Published by Elsevier Inc.

Creative Commons

This is an open access article distributed under the terms of the [Creative Commons CC-BY](#) license, which permits unrestricted use, distribution, and reproduction in any medium, provided the original work is properly cited.

You are not required to obtain permission to reuse this article.

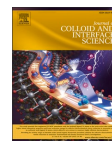
To request permission for a type of use not listed, please contact [Elsevier](#) Global Rights Department.

Are you the [author](#) of this Elsevier journal article?



Contents lists available at ScienceDirect

Journal of Colloid And Interface Science

journal homepage: www.elsevier.com/locate/jcis

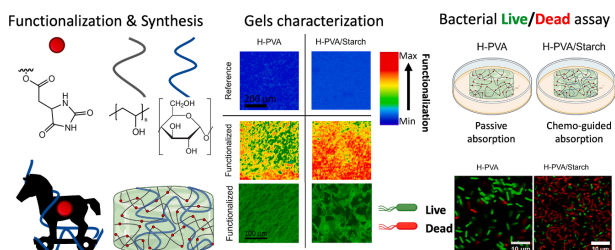
Highly biocidal poly(vinyl alcohol)-hydantoin/starch hybrid gels: A “Trojan Horse” for *Bacillus subtilis*

Vanessa Rosciardi^{a,b}, Damiano Bandelli^a, Gavino Bassu^{a,b}, Ilaria Casu^a, Piero Baglioni^{a,b,*}

^a Department of Chemistry “Ugo Schiff”, University of Florence, Via della Lastruccia 3, 50019 Sesto Fiorentino (Florence), Italy

^b CSGI, Center for Colloids and Surface Science, University of Florence, Via della Lastruccia 3, 50019 Sesto Fiorentino (Florence), Italy

GRAPHICAL ABSTRACT



ARTICLE INFO

Keywords:
PVA
Starch
Cryogel
Trojan Horse
Hydantoin
Anti-bacterial

ABSTRACT

Hypothesis: Poly (vinyl alcohol) (PVA) cryogels can be functionalized with *n*-Halamines to confer biocidal features useful for their application as wound-dressing tools. Their efficacy can be boosted by stably embedding a polymeric bacterial food source (e.g., starch) in the gel matrix. The bioavailability of the food source lures bacteria inside the gel network via chemotactic mechanisms, promoting their contact with the biocidal functionalities and their consequent inactivation.

Experiments: The synthesis of a novel hydantoin-functionalized PVA (H-PVA-hyd) is proposed. The newly synthesized H-PVA-hyd polymer was introduced in the formulation of H-PVA-based cryogels. To promote the cryogelation of the systems we exploited phase-separation mechanisms employing either a PVA carrying residual acetate groups (L-PVA) or starch as phase-segregating components. The permanence of the biocidal functionality after swelling was investigated via proton nuclear magnetic resonance (¹H NMR) and Fourier transform infrared (FT-IR) microscopy. The activated H-PVA-hyd cryogels have been tested against bacteria with amylolytic activity (*Bacillus subtilis*) and the outcomes were analyzed by direct observation via confocal laser scanning microscopy (CLSM).

Findings: The cryogels containing starch resulted in being the most effective (up to 90% bacterial killing), despite carrying a lower amount of hydantoin groups than their starch-free counterparts, suggesting that their improved efficacy relies on a “Trojan Horse” type of mechanism.

* Corresponding author at: Department of Chemistry “Ugo Schiff”, University of Florence, Via della Lastruccia 3, 50019 Sesto Fiorentino (Florence), Italy.

E-mail addresses: vanessa.rosciardi@unifi.it (V. Rosciardi), damiano.bandelli@unifi.it (D. Bandelli), gavino.bassu@unifi.it (G. Bassu), ilaria.casu@stud.unifi.it (I. Casu), baglioni@csgi.unifi.it (P. Baglioni).

<https://doi.org/10.1016/j.jcis.2023.11.142>

Received 21 August 2023; Received in revised form 22 November 2023; Accepted 22 November 2023

Available online 27 November 2023

0021-9797/© 2023 The Author(s). Published by Elsevier Inc. This is an open access article under the CC BY license (<http://creativecommons.org/licenses/by/4.0/>).

Open Access Article

Effect of Composition and Freeze-Thaw on the Network Structure, Porosity and Mechanical Properties of Polyvinyl-Alcohol/Chitosan Hydrogels

by  Fernando Soto-Bustamante ^{1,2} ,  Gavino Bassu ^{1,2},  Emiliano Fratini ^{1,2}  and  Marco Laurati ^{1,2,*}  

¹ Dipartimento di Chimica "Ugo Schiff", Università di Firenze, 50019 Firenze, Italy

² Consorzio per lo Sviluppo dei Sistemi a Grande Interfase (CSGI), c/o Università di Firenze, 50019 Firenze, Italy

* Author to whom correspondence should be addressed.

Gels **2023**, *9*(5), 396; <https://doi.org/10.3390/gels9050396>

Submission received: 30 March 2023 / Revised: 3 May 2023 / Accepted: 5 May 2023 / Published: 9 May 2023

(This article belongs to the Special Issue Polymer Networks and Gels 2022)




Download 

Browse Figures

Versions Notes

Article

Effect of Composition and Freeze-Thaw on the Network Structure, Porosity and Mechanical Properties of Polyvinyl-Alcohol/Chitosan Hydrogels

Fernando Soto-Bustamante ^{1,2}, Gavino Bassu ^{1,2}, Emiliano Fratini ^{1,2} and Marco Laurati ^{1,2,*}

¹ Dipartimento di Chimica "Ugo Schiff", Università di Firenze, 50019 Firenze, Italy

² Consorzio per lo Sviluppo dei Sistemi a Grande Interfase (CSGI), c/o Università di Firenze, 50019 Firenze, Italy

* Correspondence: marco.laurati@unifi.it

Abstract: We report the synthesis and characterization of poly (vinyl alcohol) (PVA)/Chitosan (CT) cryogels for applications involving the uptake and entrapment of particulate and bacterial colonies. In particular, we systematically investigated the network and pore structures of the gels as a function of CT content and for different freeze-thaw times, combining Small Angle X-Ray Scattering (SAXS), Scanning Electron Microscopy (SEM), and confocal microscopy. The nanoscale analysis obtained from SAXS shows that while the characteristic correlation length of the network is poorly affected by composition and freeze-thaw time, the characteristic size of heterogeneities associated with PVA crystallites decreases with CT content. SEM investigation evidences a transition to a more homogeneous network structure induced by the incorporation of CT that progressively builds a secondary network around the one formed by PVA. A detailed analysis of confocal microscopy image stacks allows to characterize the 3D porosity of the samples, revealing a significantly asymmetric shape of the pores. While the average volume of single pores increases with increasing CT content, the overall porosity remains almost unchanged as a result of the suppression of smaller pores in the PVA network with the progressive incorporation of the more homogeneous CT network. Increasing the freezing time in the FT cycles also results in a decrease of porosity, which can be associated with a growth in the crosslinking of the network due to PVA crystallization. The linear viscoelastic moduli measured by oscillatory rheology show a qualitatively comparable frequency-dependent response in all cases, with a moderate reduction with increasing CT content. This is attributed to changes in the structure of the strands of the PVA network.

Keywords: hydrogel; cryogel; poly (vinyl alcohol); chitosan; porosity; network structure; rheology



Citation: Soto-Bustamante, F.; Bassu, G.; Fratini, E.; Laurati, M. Effect of Composition and Freeze-Thaw on the Network Structure, Porosity and Mechanical Properties of Polyvinyl-Alcohol/Chitosan Hydrogels. *Gels* **2023**, *9*, 396. <https://doi.org/10.3390/gels9050396>

Academic Editors: Gaio Paradossi, Costas S. Patrickios, Ester Chiessi and Ferenc Horkay

Received: 30 March 2023

Revised: 3 May 2023

Accepted: 5 May 2023

Published: 9 May 2023



Copyright: © 2023 by the authors. Licensee MDPI, Basel, Switzerland. This article is an open access article distributed under the terms and conditions of the Creative Commons Attribution (CC BY) license (<https://creativecommons.org/licenses/by/4.0/>).

1. Introduction

Hydrogels are chemically or physically cross-linked 3D porous polymer networks formed by water-soluble polymers, capable of absorbing a large quantity of water. They find application in several fields, comprising drug delivery [1–3], filtration processes [4–6], water harvesting [7–9], growth of bacterial colonies [10–13], and cultural heritage restoration [14–16]. Different synthetic polymers can be used for producing hydrogels, including poly (ethylene glycol) (PEG) [17], poly (2-hydroxyethyl methacrylate) (PHEMA) [18,19], poly (acrylic acid) (PAA) [20], poly (acrylamide) (PAAm) [21], poly (vinyl alcohol) (PVA) [22,23], among others. In particular, hydrogels formed by PVA have attracted much attention and research effort [24] owing to the non-toxicity of PVA, which is essential in biomedical applications [25], and which combines with a high mechanical strength [26] and a facile tuning of properties [27]. PVA hydrogels are most commonly prepared using physical crosslinking obtained through the freeze-thaw (FT) method first introduced by Peppas and coworkers [28]. In the freezing step, the formation of ice crystals favors the segregation of PVA-rich phases, in which polymer–polymer interactions facilitate hydrogen bonding and crystallization. The



Conformational and solvent effects in structural and spectroscopic properties of 2-hydroxyethyl methacrylate and acrylic acid

Author:

Irene Vettori, Marina Macchiagodena, Marco Pagliai, Gavino Bassu, Emiliano Fratini, Piero Baglioni

Publication: Journal of Molecular Liquids**Publisher:** Elsevier**Date:** 15 August 2022

© 2022 Elsevier B.V. All rights reserved.

Journal Author Rights

Please note that, as the author of this Elsevier article, you retain the right to include it in a thesis or dissertation, provided it is not published commercially. Permission is not required, but please ensure that you reference the journal as the original source. For more information on this and on your other retained rights, please visit: <https://www.elsevier.com/about/our-business/policies/copyright#Author-rights>

BACK

CLOSE WINDOW



Conformational and solvent effects in structural and spectroscopic properties of 2-hydroxyethyl methacrylate and acrylic acid

Irene Vettori^{a,b,1}, Marina Macchiagodena^{a,1}, Marco Pagliai^{a,*}, Gavino Bassu^{a,b}, Emiliano Fratini^{a,b,*}, Piero Baglioni^{a,b}

^a Department of Chemistry "Ugo Schiff", Via della Lastruccia 3, Sesto Fiorentino (FI), 50019, Italy

^b Consorzio per lo Sviluppo dei Sistemi a Grande Interfase (CSGI), Via della Lastruccia 3, Sesto Fiorentino (FI), 50019, Italy



ARTICLE INFO

Article history:

Received 17 March 2022

Revised 4 May 2022

Accepted 18 May 2022

Available online 23 May 2022

Keywords:

2-hydroxyethyl methacrylate

Acrylic acid

Molecular dynamics simulations

Conformers

Spectroscopic properties

DFT calculations

ABSTRACT

2-hydroxyethyl methacrylate (HEMA) and acrylic acid (AA) are monomers widely used in the production of hydrogels with medium-high water content. The structural and spectroscopic properties of HEMA and AA were studied using a combination of computational strategies based on both density functional theory (DFT) calculations and molecular dynamics (MD) simulations. DFT calculations have confirmed the co-existence of two stable HEMA conformers, while solute-solvent interactions between HEMA and AA with water were characterized by the analysis of MD simulations carried out by employing four different water models and different simulation conditions. The carbonyl and hydroxyl oxygen atoms of HEMA are involved in hydrogen bonding, whereas the ester oxygen atom does not appreciably interact with the solvent. No significant differences in solute-solvent interactions are found between the two HEMA conformers. Their spectroscopic properties were calculated and the results were compared to experimental data. Although electronic spectra do not really allow a differentiation of the conformers, IR spectra present some peculiar bands to discriminate the presence and obtain information on the ratio of the conformers in solution. To verify the influence of a solvent with higher dipole moment on chemical properties, acetonitrile has been considered as an alternative solvent.

© 2022 Elsevier B.V. All rights reserved.

1. Introduction

2-Hydroxyethyl methacrylate (HEMA) and acrylic acid (AA) are monomers widely used as building blocks in numerous fields of application where the presence of chemical hydrogels with a medium/high water content and good mechanical properties is needed. Their use, both as homopolymers (poly-HEMA and poly-AA) or co-polymers (poly-(HEMA/AA)), spreads from biomedical [1–3] to artworks conservation [4] applications. These monomers deserve deeper investigations for several reasons.

In the case of HEMA, despite the current state of art comprehends several data on the syntheses, characterization and degradation on the polymer (pHEMA) [5–10], just a few papers investigate pHEMA noncovalent inter- and intra-molecular interactions [11–14], and surprisingly, literature lacks even more on studies related to the monomer. Few data report on HEMA

hydrogen bonding from experimental spectra speculations [15,13], proposing dimeric intermolecular or quasi-ring intramolecular structures at low concentration [13]. Both the HEMA carbonyl and alcoholic functional groups appear to be involved in hydrogen bonding, according to vibrational spectra [15,13]. Regarding the monomer structure, as for other methacrylates [16], there are already some experimental evidences of the existence of two stable HEMA conformers in solution, one presenting the carbonyl moiety in *cis* position with respect to the vinyl group, while the other one in *trans* position. In particular, experimental spectra of HEMA present some peaks that can be deconvoluted into contributions arising from these isomers [13]. To the best of our knowledge, the only paper that was entirely devoted to a preliminary study on the HEMA rotational isomers is the one published by Belaidi et al. (2015) [17]. These authors confirmed experimental results with *ab-initio* calculations and theoretical spectra of the two conformers. However, still some questions to answer remain: (i) what is the percentage of *s-cis*-like conformer with respect to the *s-trans*-like one in solution? (ii) How does this ratio evolve with temperature? (iii) Does this conformation difference affect interactions with the solvent and with other solutes?

* Corresponding author at: Department of Chemistry "Ugo Schiff", Via della Lastruccia 3, Sesto Fiorentino (FI), 50019, Italy (M. Pagliai and E. Fratini).


E-mail addresses: marco.pagliai@unifi.it (M. Pagliai), emiliano.fratini@unifi.it (E. Fratini).


¹ Authors contributed equally.

[RETURN TO ISSUE](#)[< PREV](#) **A: STRUCTURE, SPECTR...** [NEXT >](#)THE JOURNAL OF
PHYSICAL
CHEMISTRY
A[Get e-Alerts](#)

2-Butanol Aqueous Solutions: A Combined Molecular Dynamics and Small/Wide-Angle X-ray Scattering Study

Marina Macchiagodena, Gavino Bassu, Irene Vettori, Emiliano Fratini*, Piero Procacci, and Marco Pagliai*

 **Cite this:** *J. Phys. Chem. A* 2022, 126, 47, 8826–8833

Publication Date: November 17, 2022 

<https://doi.org/10.1021/acs.jpca.2c05708>

Copyright © 2022 The Authors. Published by American Chemical Society. This publication is licensed under [CC-BY 4.0](#).

[Open Access](#)

Article Views | Altmetric | Citations

760

-

1

[LEARN ABOUT THESE METRICS](#)

Share Add to Export



2-Butanol Aqueous Solutions: A Combined Molecular Dynamics and Small/Wide-Angle X-ray Scattering Study

Published as part of *The Journal of Physical Chemistry virtual special issue "Vincenzo Barone Festschrift"*.

Marina Macchiagodena, Gavino Bassu, Irene Vettori, Emiliano Fratini,* Piero Procacci, and Marco Pagliai*

Cite This: *J. Phys. Chem. A* 2022, 126, 8826–8833

Read Online

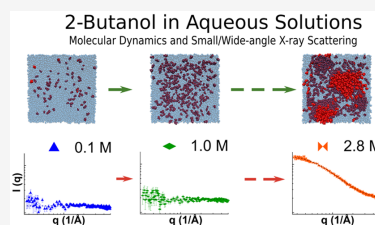
ACCESS |

Metrics & More

Article Recommendations

Supporting Information

ABSTRACT: Structural properties of 2-butanol aqueous solutions at different concentrations have been studied using small- and wide-angle X-ray scattering and molecular dynamics simulations. The experimental structure factors have been accurately reproduced by the simulations, allowing one to explain their variation with concentration and to achieve a detailed description of the structural and dynamic properties of the studied systems. The analysis of experimental and computational data has shown that 2-butanol, the simplest aliphatic chiral alcohol, tends to form aggregates at a concentration above 1 M, affecting also both the structural and dynamic properties of the solvent.



INTRODUCTION

Alcohols are amphiphilic molecules formed by two different moieties: one polar, characterized by the hydrophilic –OH group, and one apolar, corresponding to the aliphatic hydrocarbon chain. This characteristic affects both the structure of the alcohol in the aqueous solution and the dynamics of the surrounding water molecules. As the alcohol concentration increases, the system responds forming alcohol clusters.¹

The alcohol aqueous solutions are widely studied for their specific properties and applications in numerous research, technological, and medical sectors.^{2–5}

In the present study, both experimental and computational results for 2-butanol aqueous solutions are reported. 2-Butanol is one of the isomers of butyl alcohol and the only chiral one. Two enantiomeric forms of 2-butanol ((*R*)- and (*S*)-) exist as shown in panels (a) and (b) of Figure 1, and in nature it is usually present as a racemic mixture.^{2,6}

Among the butyl alcohol isomers, 2-butanol is the less studied one. In fact, interactions in 2-butanol-based systems have been only partially investigated by a computational approach, mainly through density functional theory (DFT) calculations, focusing on chirality aspects^{7,8} or on clathrate structure formation.⁹ The interest in studying 2-butanol relies mainly in its uses in the fuel industry, both as an additive^{10,11} and as a platform for biofuel production.^{12,13} Further fields of application regard the food industry,^{14,15} electroadsorption,^{16,17} and hydrogenation routes.¹⁸

To characterize the structure and the dynamics of 2-butanol aqueous solutions, molecular dynamics (MD) simulations and

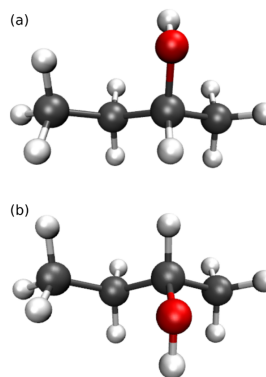


Figure 1. Molecular structure of (a) (*R*)-2-butanol and (b) (*S*)-2-butanol enantiomers.

Received: August 10, 2022
Revised: November 3, 2022
Published: November 17, 2022



Acknowledgments

Here we are... after two thesis degrees I find myself writing the last thanks to the people close to me. How could I introduce so many thanks? In which order? I imagine the few loved ones who will have the pleasure to read these few rows, after flying over the hundreds of pages that constitute this thesis, seeing just for a split second some colourful figure, and finally here.

Without any doubt an immense thanks goes to my family, an inexhaustible source of smiles and support. My thoughts go to you in the most difficult and adverse moments... and perhaps the only regret is that Grandmother Luisa passed away so close to the finish, *"but what should we do? go on"*.

To my Professors Emiliano and Marco, thank you for your guidance, mentorship, and for making this PhD path a wonderful adventure.

A much more informal thanks goes to my friends. People capable of rise in me the loudest laughter and capable of making me smile like a pomegranate. Much more than friends, because friendship after too many years does not remain as such but becomes a terminal condition; Jo, La Fayette, and Blalla, thanks.

In the sea of events that I am sure have happened over the course of 8 or 9 years of study at the university, I think that 4 or 5 moments remain imprinted on each of us, perhaps a few more, indelible moments full of emotion like a difficult exam (mathematics 2, for which I will always thank Gemma) or the long-awaited graduation of a friend (Pablo). A big thank you to Liccia and Francesco, gluttonous dinner buddies and irreplaceable supporters. The thing I never believed until now was that all those years would pass as quickly as a breath.

If I think back to everything that happened in the years of this doctorate, I must admit that it was a really good experience, not only for the travel, the places, and the food but for the extraordinary people I met. Among these, two extremely interesting people stand out who unexpectedly changed the direction of my life, at least for the moment... Teresa and Andrea thank you.

This is certainly not the complete list of people who have supported me on this journey, and I will certainly apologize to everyone else for forgetting to mention them, but I am sure I will not miss the opportunity to thank you in person. As a good idiot I want to thank a person who certainly wouldn't like to be named in such an explicit way but who has characterized these last three years: thank you for always being there for me.